RICE UNIVERSITY

Multi-wavelength Analysis of Solar Transient Phenomena

by

Aaron J Coyner

A Thesis Submitted
in Partial Fulfillment of the
Requirements for the Degree

DOCTOR OF PHILOSOPHY

Approved, Thesis Committee:

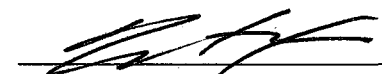

David Alexander , Chair
Associate Professor of Physics and
Astronomy

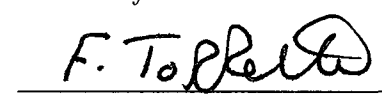

Frank Toffoletto
Associate Professor of Physics and
Astronomy

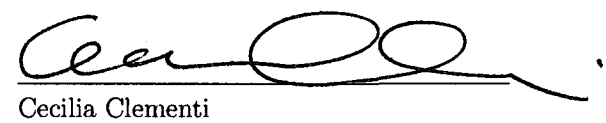

Cecilia Clementi
Associate Professor of Chemistry

Houston, Texas

July, 2008

ABSTRACT

Multi-wavelength Analysis of Solar Transient Phenomena

by

Aaron J Coyner

Solar transient phenomena such as solar flares and coronal mass ejection are some of the most energetic and explosive phenomena affecting the solar environment. Emission signatures within solar flares provide direct insight into the physical mechanisms involved in the flaring process as well as the role the magnetic field topology plays in the energy release and particle transport within flares. Specifically, the work here addresses the temporal and spatial relationships between ultraviolet and hard X-ray flare emissions while also addressing the relationship between hard X-ray emission evolution in flares and the development of quasi-separatrix layers (QSLs) within the magnetic structure of the flaring region. As a final component, we address the implications of pre-event solar conditions such as magnetic configuration and flare productivity on the particle composition of solar energetic particle (SEP) events seen at 1AU. Specifically, we find that co-spatial and co-temporal UV and hard X-ray emission expected in 1-D loop flare models only account for a portion of the observed flare

emission, and a complete explanation of the flaring process must take into account more complex and time-varying magnetic topologies along with contributions from multiple physical processes. Finally, we find, for particle events, that closed magnetic configurations at higher energies result in higher average Fe/O enhancements while the amount of open field and the active region appear to have no direct relationship to the observed SEP compositions.

Acknowledgments

I would like to thank my thesis advisor Dr. David Alexander for his guidance and assistance with the completion of this research. In addition, I would like to thank Dr. Frank Toffoletto and Dr. Cecilia Clementi for serving on my committee. Thanks to Lirong Tian for her assistance in helping me understand solar magnetic fields and the field extrapolation process. I would also like to acknowledge and thank the members of "the lunch group" (Albert Chang, Mike Mott, Roman Gomez, Gary Kilper, Greg Brunner) for their assistance in maintaining my sanity throughout the graduate school process. I pass my gratitude and acknowledgements to the members of the Rice Solar Group for their scientific support and encouragement. I would like to acknowledge and thank the Texas Space Grant Consortium for their financial support for the last two years. Finally, I'd like to graciously acknowledge my family and friends for their understanding and encouragement throughout the writing process.

Contents

List of Figures

List of Tables

Chapter 1
Introduction

The sun exhibits a wide array of transient activity on a number of spatial and temporal scales. The most prominent of these are the large and energetic explosions associated with solar flares and coronal mass ejections (CMEs). Despite being some of the most frequently solar observed phenomena, solar transients are still not sufficiently well understood to fully address the wide array of activity observed, the relationships between them, their broader implications for the heliospheric environment, and most critically the Sun-Earth connection. Flares and CMEs provide observational constraints and physical insight into magnetically-driven impulsive phenomena on the Sun and also similar phenomena in stars and other astrophysical objects. Solar transients are key components in the Sun-Earth connection shaping the heliospheric environment by releasing enhanced electromagnetic radiation and energetic particles to create a range of geomagnetic activity classified as space weather. These space weather events produce energetic photon and particle radiation that can adversely affect human life, ground-based electrical systems, and space-based resources, such as communications satellites. While many of these geoeffective storms are directly linked to coronal mass ejections (Weiss et al., 1996), the energy released from solar flares, believed to be driven by magnetic reconnection in the solar corona, provides

key observational constraints on the physical mechanisms that govern the plethora of transient activity in the solar atmosphere. Studies of the combination of solar flares, coronal mass ejections, and the resulting particle events seen at Earth help to clarify the physics influencing the always volatile Sun-Earth relationship.

In this thesis, we investigate observational relationships involving chromospheric emission signatures and the solar magnetic field to clarify the nature and significance of temporal and spatial relationships for ultraviolet and hard X-ray chromospheric emission, the relationship between the hard X-ray evolution and the evolution of the magnetic topology within a flare, and the connection between solar magnetic field and active region flare productivity to the observed particle abundance ratios for solar energetic particles seen at Earth. In combination, these three studies clarify the roles of the solar magnetic field, energy release and particle transport effects in generating the observed transient signatures and the physical processes responsible for their creation. In this chapter, we will provide a basic overview of the transient events that influence space weather focusing primarily on the solar flare phenomenon and the development of solar energetic particle events.

1.1 Solar Flare Characteristics

Solar flares are events in which large amounts of energy are released over short timescales as a result of the relaxation of the solar magnetic field, resulting in a variety of responses by the solar atmosphere. Solar flares can often be described by three

phases:

- a pre-flare phase showing an energetic build up, frequently in the form of intermittent, low intensity activity
- an impulsive phase, most clearly defined by one or more intense bursts of hard X-ray emission over timescales of order minutes representing the response of the atmosphere to the most intense magnetic energy release of the flare
- a final gradual phase, denoting the eventual decay of flare energy over timescales of hours.

Solar flares produce emission signatures in wavelengths spanning the entire electromagnetic spectrum. The research presented in this thesis will focus on signatures originating from the chromosphere and the corona. Our observations of the chromosphere primarily utilize Hα emission, resulting from the first Balmer transition of hydrogen at 6563 Å, ultraviolet emission, focusing on a narrow bandpass peaked at 1600 Å, and hard X-rays, primarily photon energies in the range 25-100 keV, while our coronal observations are provided primarily by extreme ultraviolet loop observations in specific narrow band wavelengths centered on 171 Å, 195Å, 284Å, and 304Å. The chromospheric emission, particularly in Hα and in the ultraviolet wavelengths, observed by the Transistion Region and Coronal Explorer (TRACE: Handy et al. , 1999), generally shows ribbon-like structures (see Figure 1.1) which define the chro-

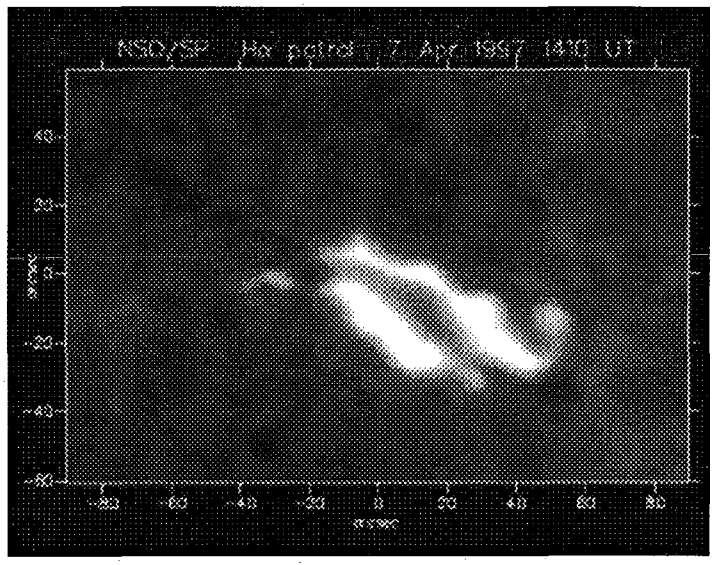

Figure 1.1 Example of the classic two-ribbon flare picture taken in Hα from National Solar Observatory (NSO) data on 7 Apr 1997

mospheric boundaries of the expanding flare, while the X-ray and EUV emission form a complex arcade of coronal loop structures connected to the chromospheric ribbons at their base (Figure 1.2). The Bastille Day flare from 2000 is one of the best example of a developing flare loop arcade. In Figure 1.2, a series of thin coronal loops form, giving the flare an appearance like that of a slinky. Each of the loops is a plasma-filled magnetic structure anchored to the chromosphere with one footpoint on each of the two chromospheric ribbons. We will elaborate on the importance of the morphology in these flares in Section 1.1.2.

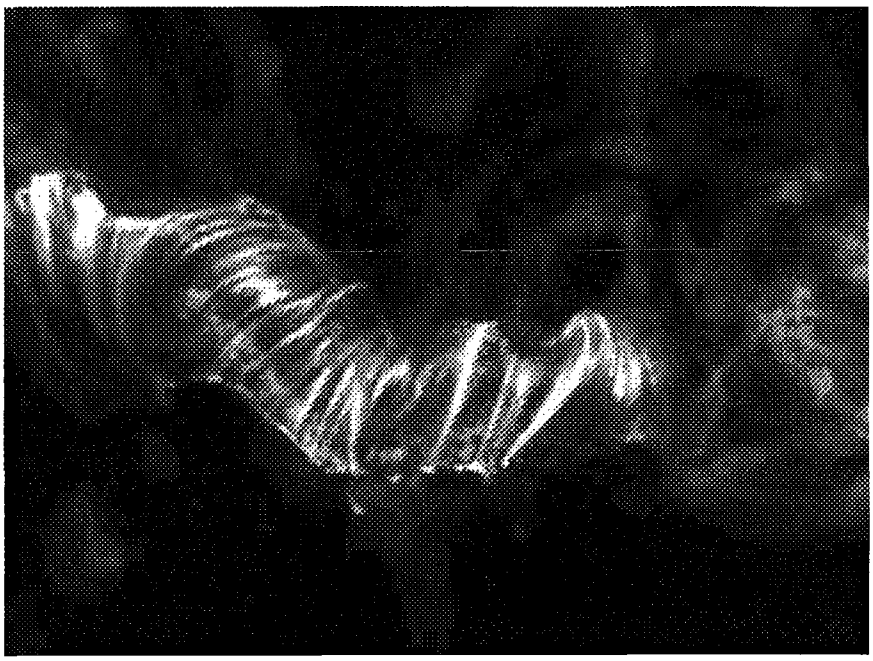

Figure 1.2 Example of a complex flare loop arcade taken from the well-known Bastille Day flare, an X-class flare from 14 July 2002. Data shown is taken from TRACE 195Å observations.

1.1.1 Flare Classification and Time profiles

The most common way flares are classified is in terms of intensity measured in the 1-8 Å soft X-ray data seen from the Geostationary Operational Environmental Satellites (GOES) satellites, operated by the National Oceanic and Atmospheric Administration (NOAA). This classification is based on a logarithmic scale of the peak flux measurements, with X-class flares being the strongest, exhibiting peak fluxes above 10^{-4} watts per square meter. Table 1.1 provides the full classification scale

used. Many flare studies largely focus on C-class flares and above, i.e. flares with peak soft X-ray flux above 10^{-6} W/m^2. Shown in Figure 1.3 is a GOES profile of the soft X-ray emission for a large X 2.5 flare, determined from the peak of the lower energy (upper curve) GOES band. GOES records soft X-ray emission in two bands, the 1-8 Å band used for flare classification and the 0.5-4 Å higher energy channel to provide additional information on hotter emitting plasma. It should be noted that the GOES classification is based on full-Sun measurements and not centered on specific events. When a flare occurs, however, the GOES bandpasses are dominated by flare emission (see Figure 1.3). This flare shows many of the components of a typical flare soft X-ray response:

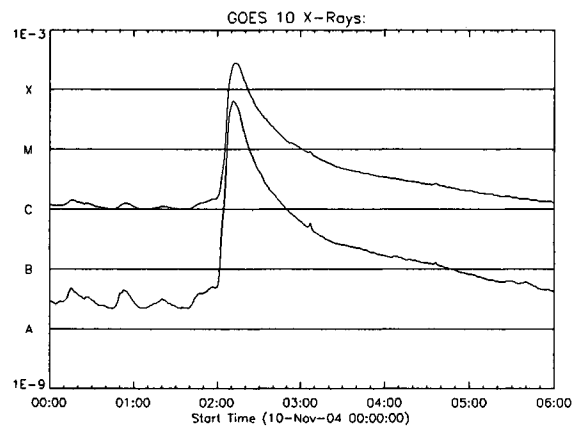

Figure 1.3 Sample GOES plot from 10-Nov-2004 depicting the soft X-ray response of an X 2.5 flare. The soft X-ray profile shows a quick impulsive rise and a gradual exponential decay over timescales of hours. The upper curve shows lower energy soft X-rays (1-8 Å). The lower curve shows emission from 0.5-4 Å .

GOES Flare Class	Flux Range (W/m^2)
A	$< 10^{-7}$
B	10^{-7}-10^{-6}
C	10^{-6}-10^{-5}
M	10^{-5}-10^{-4}
X	$> 10^{-4}$

Table 1.1 The GOES flare classification system based on 1-8 Å fluxes during the peak of the flare

- a presence of some weak activity prior to the flare
- a fast-rising impulsive phase peaking within a few minutes of its initial onset
- a gradual decay phase, representing an exponential decay of the flare energy and the return of the corona to a typical soft X-ray background.

It is important to note that the smooth appearance of the soft X-ray emission does not translate to other important wavelengths. Hard X-ray and UV emissions will be the focus of much of the work of this thesis; however, the soft X-ray response is critical for classification and general characteristics of the flare.

Hard X-ray and UV Time Profiles

While the soft X-ray profiles used in the classification are generally smooth, due largely to the thermal nature of soft X-ray emission, the UV and hard X-ray emissions exhibit a much more impulsive character. Hard X-rays, in particular, show a series of distinct impulses generally involving a quick succession of bursts over timescales

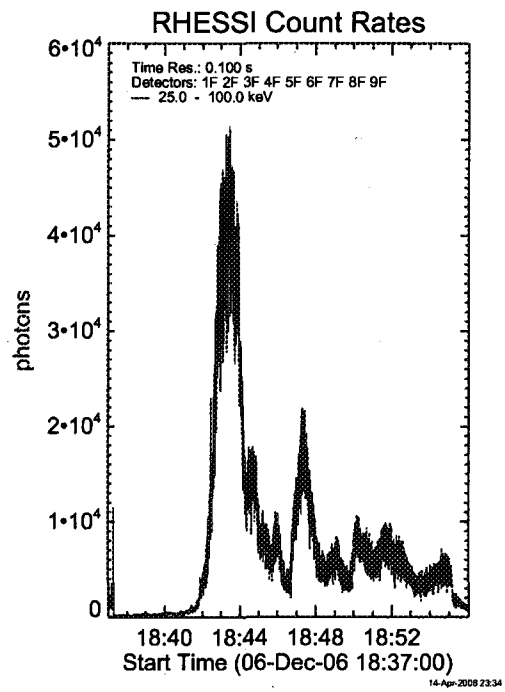

Figure 1.4 RHESSI hard X-ray time profile for energies 25-100 keV at 0.1 second full temporal resolution. The general character of the profile is determined by the magnetically trapped population of electrons that precipitates into the chromosphere and produces HXR emission via bremsstrahlung. The smaller timescale variation have been shown to relate to direct injection of electrons (See Aschwanden, 1998).

of several minutes. An example hard X-ray emission profile, taken from the Reuven Ramaty High Energy Solar Spectroscopic Imager (RHESSI: Lin et al., 2002), is displayed in Figure 1.4. This hard X-ray lightcurve, covering the energy range 25-100 keV, shows the X-ray emission profile for a typical large X class event. We observe large-scale impulses on the order of minutes each with a quick rise phase that can be interpreted as a direct response to the magnetic energy release driving the flare.

Each of the impulses, and their combinations, have direct implications for the flare energy release which will be addressed in detail in Chapter 4. Brown (1973) showed that the these large-scale pulses of X-ray emission are generally defined by the solar atmospheric response to an accelerated population of electrons arising from some initial energy release. Specifically, the hard X-ray emission is believed to be governed by the acceleration of electrons from the flare trigger site in the corona to the energy deposition locations in chromosphere. The acceleration of these electrons is, in turn, governed by the magnetic field structure as particles travelling through the corona follow the magnetic lines in a low-β plasma. β, the ratio of gas pressure to magnetic pressure is defined by

$$\beta = \frac{8\pi P_0}{B_0^2} \tag{1.1}$$

where P_0 is the gas pressure of the plasma at a given location and B_0 is the magnetic field strength at that location. For the corona, $\beta \ll 1$; therefore the magnetic pressure dominates the plasma behavior.

As a result of the energy release, the flare particles are accelerated along the field. Each particle is injected into the flaring loop with a specific *pitch angle*, defined as the angle between the particle's velocity vector and the magnetic field. The accelerated particles travel along the magnetic field lines connecting the acceleration site to the chromosphere. These energized field lines ultimately form the post-flare loops shown in Figure 1.2. The magnetic field is weaker in the corona than in the chromospheric

footpoints. Therefore, as particles travel from the acceleration site, near the top of the loop, toward the footpoints, they pass through regions of increasingly stronger magnetic field. Depending on the field gradient and the pitch angle of the particle, the mirror force, resulting from the converging field, may cause the particles to remain trapped in the coronal portion of the loop. Thus, particles within the magnetic structure fall into two populations based on their initial pitch angles and the rate of convergence of the magnetic field. A directly precipitating component results from particles with pitch angles small enough to escape the loss cone of the trap defined by:

$$sin\theta_L = \sqrt{\frac{B}{B_{max}}} \tag{1.2}$$

where θ_L is the loss cone angle, the maximum pitch angle allowed to escape the trap, B is the field strength near the looptop and B_{max} is the field strength at the footpoint of the trap.

Particles with pitch angles less than θ_L will directly precipitate into the chromosphere produce hard X-ray emission via bremsstrahlung radiation on short timescales seen as emission spikes in the full-resolution RHESSI profile (Aschwanden,1998). A magnetically-trapped population of electrons, those particle with larger initial pitch angles than the loss cone angle, θ_L, remain in the loop and are reflected from one side of the loop to the other. These particles remain in this magnetic trap until scattered

by Coulomb collisions, or other mechanisms (e.g. waves) which modify the particle pitch angles sufficiently to inject them into the loss cone and allow them to the precipitate to the chromosphere and emit X-rays. Magnetic traps, as described, need not have the same field strength at both footpoints. This will result in two different loss cones within the legs of the loop and will result in an asymmetric magnetic trap (Alexander and Metcalf, 2002; McClements and Alexander, 2005). Both components of the accelerated electron population produce hard X-ray emission as the result of bremsstrahlung radiation (discussed in detail in Section 2.1.4) and then deposit their remaining energy into the chromosphere via collisions within the dense plasma. This energy release results in bulk energization and heating of the chromosphere and is observationally evident in chromospheric signatures, such as UV and Hα kernels.

Aschwanden (1998) showed that these two populations were responsible for separate components of the observed X-ray emission profile. The larger scale structure of the bursts, having a broader pulse shape, arises from the emission of the trapped population. In contrast, the directly precipitating electrons provide the smaller scale structure, appearing as spikes on timescales of tenths of seconds visible at the full time resolution of RHESSI (depicted in Figure 1.4). These spikes are evident throughout the flare, indicating a recurring direct injection component throughout the duration of the flare.

In the ultraviolet, solar flares have been shown to exhibit a similar impulsive na-

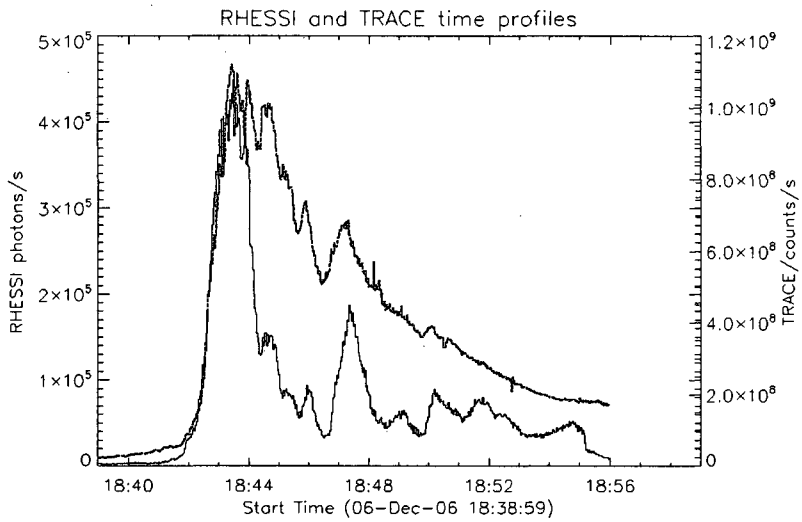

Figure 1.5 Comparison of TRACE 1600 Å and RHESSI 25-100 keV hard X-ray time profiles for the 6 December 2006 X6.5 flare event.

ture to that seen in the hard X-ray emission; however, they often exhibit a more gradual falloff than the hard X-rays, likely due to the effects of bulk heating of the chromosphere in the gradual phase of the flares (Fletcher and Warren, 2003). Studies of the overall UV response of spatially-unresolved flares have shown that the time development of the UV emission is most closely associated with the hard X-ray emission (Cheng et al., 1989; Kane, Frost and Donelly, 1979). Figure 1.5 displays the overall time profiles for the UV and HXR emission for the X6.5 flare from 6 December 2006. For typical strong impulses, we find that the UV shows a strong impulsive character similar to HXR emission, suggesting that the same particle population is critical to

the production of the UV signatures. When examined on a spatially-resolved level, emissions originating in the chromosphere, like the $H\alpha$ for example, have shown significant variation in temporal response compared with the hard X-ray emission profile. In a recent study of Hα localized sources compared with the HXR emission for two large flares, Zharkova and Kashapova (Zharkova et al., 2007; Kashapova et al, 2007) showed that these localized sources within a flare have varied time profiles, based on the precipitating populations of both electrons and protons at specific spatially localized sites. In both these studies, the authors report the formation of multiple loop structures within the flaring region with electrons and protons being preferentially transported into different loops as theorized by Zharkova and Gordovsky (2004). The variations in temporal development allows the different particle populations to be distinguished.

The observations of Warren and Warshall (2001) indicated some variation in the temporal responses of different localized UV sources in association with hard X-ray emission. The UV sources active during the X-ray flare bursts exhibited the strong temporal correlation seen in other studies. In contrast, the sources observed prior to the hard X-ray flare onset do not show any correlations with the HXR emission. Despite the temporal correlations, these localized sources show distinct spatial variation from their X-ray counterparts. The spatial variations seen by Warren and Warshall using the Hard X-ray Telescope (HXT), aboard the YOHKOH Solar Observatory,

(Kosugi et al., 1991) and UV observations from the TRACE telescope provide initial evidence for additional magnetic complexity within the flaring region. The variation in specific localized UV development provides a complicated picture of UV emission as it relates to the hard X-rays, suggesting additional magnetic complexity than previously considered and both the likelihood of multiple emission processes and multiple particle populations, the greater implications of which we will address in this work.

1.1.2 Flare Morphology and the Importance of Magnetic Topology

While each solar flare is unique, there are some common characteristics which occur in most events. Notably in the ultraviolet, flaring regions are typically outlined by ribbon-like structures which expand outward as the flare progresses. The two ribbons lie in regions on either side of a magnetic neutral line (also called the polarity inversion line due to the opposite magnetic polarities on either side). The ribbon structure appears primarily in UV and Hα observations with sources of emission on the ribbons often appearing as conjugate pairs. Two-ribbon flares and the subsequent loop systems are often theoretically discussed in terms of a standard 2-D model known as the CSHKP model (Carmichael, 1964; Sturrock, 1966, Hirayama, 1974; Kopp and Pneuman, 1976) which views the observed sources on the two chromospheric ribbons as footpoints for a complex of coronal loops which span the spatial separation between the ribbons to produce an arcade structure like the one shown in a 2-D projection in Figure 1.2.

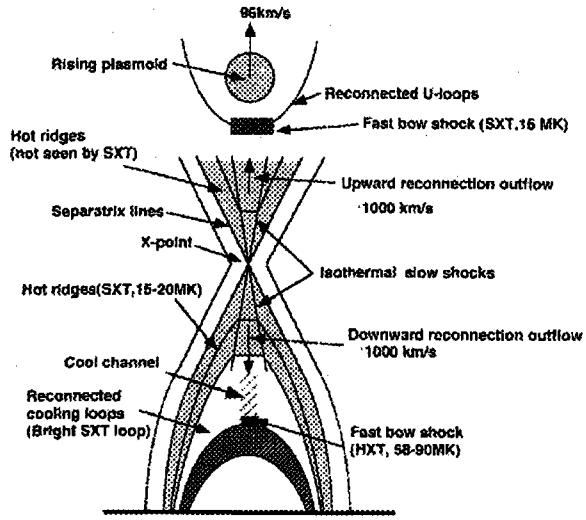

Figure 1.6 Basic 2-D flare model used as the physical foundation for many flare studies. Figure taken from Tsuneta (1997)

Though flares themselves cannot as yet be described by single all-encompassing model, the CSHKP model serves as a basis to describe many observations, their evolution, and permits reasonable physical interpretations from flare initiation through post-flare configurations while also providing a connection between flares and the interplanetary environment where the discussion of solar energetic particles becomes prevalent (Aschwanden, 2004; Tsuneta, 1997). In the CSHKP model, (see Figure 1.6), the flare is initiated by the eruption of a solar prominence or other magnetic structure rising into the corona and opening the coronal field. As the erupting plasmoid rises, the magnetic field below is stretched, storing magnetic energy and bringing oppositely directed field together. This drives reconnection within the field under-

neath the rising plasmoid. In the CSHKP model, reconnection takes the form of X-type magnetic reconnection, closing the field into loop structures and rapidly releasing energy. This energy release produces particles and heating of the corona which results in the energetic flare phenomena commonly seen. The heated plasma becomes visible in the coronal loops, originally in soft X-rays before the plasma cools to become visible in the EUV. The thermal electrons produced near the top of the loop emit in soft X-rays via thin-target bremsstrahlung radiation (see Section 2.1.4). The energy released from the reconnection is also partially converted into accelerated particles which have much higher energy than the average thermal energy of the flare plasma, resulting in a non-thermal power law distribution at energies above the thermal energy that produce the UV and HXR signatures often but not exclusively as footpoints.

This 2-D picture of a flare is a simplification of what has become widely accepted to be a larger 3-D process. Clarification of when and where energy release occurs within the complex 3-D magnetic system is a critical step in the full understanding of solar flares. To this end a number of studies have focused on the importance of the existence and evolution of what are known as separator systems (Longcope, 1996; Démoulin et al, 1993, Titov et al. 2002). These systems gain their name due to the existence of single specialized field lines called *separators* that exist at the interaction region between two systems of oppositely directly magnetic fiux. Within the 3-D

magnetic system of the flaring region, a number of self contained bipolar flux systems develop. Each of these systems is contained within a construct known as a *separatrix surface.* Separatrix surfaces divide the flaring region into distinct flux systems with surface boundaries observationally determined by mapping out discontinuities in the observed surface magnetic field (Longcope, 1996). These separatrix surfaces boundaries are often defined by separators, which have been regarded as likely locations for reconnection within the region (Démoulin et al, 1993). Flare emissions in Hα, UV and HXR emission have been shown to trace the boundaries of these separatrix surfaces (Démoulin et al., 1993; Metcalf et al., 2003). Therefore, we can use the spatial distribution of the emissions and their evolution over the course of the flare to provide a proxy for the evolution of the magnetic topology over the course of the flare, tracking topological changes and determining locations for current sheets and potential reconnection sites. In Chapter 5, we will address the connection of HXR evolution and the development of separators within NOAA Active Region 10720 for two large flares from 17 January 2005. We will further investigate the connection between the magnetic topology and the emission signatures we observe.

1.2 Eruptive Flares, and the Connection to Particle Observations

While the bulk of flare study focuses on how the solar environment responds to solar transients, it is critical to include a discussion of flares and coronal mass ejections

in the context of their effects on the Sun-earth system and, on a larger scale, the heliosphere. To this end, numerous studies have distinguished between two classes of flare event, *eruptive flares* and *confined flares* (Švestka and Cliver, 1992; Wang and Zhang 2007). Confined flares are those flares that are limited in effect to the solar atmosphere while eruptive flares are generally associated with a CME, though the specific relationship between flares and CMEs remains a subject of much study with many unresolved questions. While CMEs are largely responsible for the bulk of geomagnetic storms (Weiss et al., 1996), both eruptive flares and CMEs contribute significantly to the particles available for acceleration within the heliosphere. Studies comparing eruptive and confined flare events have found two key characteristics that indicate a likelihood of eruption, and thus, the release of particles: the intensity of the flare and the duration of the event. A statistical study of Solar Maximum Mission (SMM) data by Kahler et al. (1989) found eruption association frequencies ranging from 7% for B class flares to 100 % for X-class flares. Similar results were reported by Yashiro et al. (2005) with 90-92 % of X-class flares being associated with eruptions.

The association of large flares with eruption before the availability of CME observations led early investigators of energetic particles to attribute all particle events to flares in what is now described as the "flare myth" (Gosling, 1993; Reames, 1999). While the crude picture of the flare myth has been replaced by a more realistic two-class paradigm for particle events (see Section 1.3 for a brief description along with

Reames (1999) and the references therein for more detail), flare accelerated particles still play a key role. Particles accelerated in flares often show significant enhancements in elemental species such as ^{3}He and Fe above the nominal values typically found in coronal plasma. Impulsive Solar Energetic Particle (SEP) events have been directly associated with a flare origin. These event are generally confined to the localized flaring region and typically show the strong enhancements in ^{3}He and heavy elements consistent with enhancements expected from a flare-accelerated particle population. These events are smaller in spatial extent than gradual SEPs, the second type of SEP event, generally believed to be shock-accelerated, and are overall more numerous. Impulsive SEP events release highly energetic particles from localized flaring region on the Sun. These particles then travel into interplanetary space along well confined field lines specifically associated with the flaring region.

While the nature of impulsive events and the role of flares in their production seem to be understood, the nature of their gradual SEP brethren remains unclear. In the paradigm described by Reames, these events were believe to accelerate particles from ambient coronal plasma, with typical coronal abundances, via shocks propagating out from the corona into the heliosphere. Recent in-situ observations have called this paradigm into question and raised the importance of variations in the shock properties and the particles available for acceleration in defining the particle population seen at Earth. Further introduction of these gradual events is included in the next section.

1.3 SEP Events

Solar transients like flares and CMEs have effects that are not limited to the solar surface and corona. Among these effects are a vast array of highly energetic electrons, protons, and ionized heavy nuclei that stream from the sun into the heliosphere. Solar energetic particles comprise a portion of this constant particle stream originating directly as the result of solar flares and coronal mass ejections (CMEs) and their associated shocks. These particles possess immense energy, ranging from 30 keV to the 30 GeV for the largest events (Tylka, 2004). The importance of these solar energetic particles is two-fold.

- These particles provide clear insight into the energization process for particles at the Sun (Mason, Mazur, and Dwyer, 1999) since they can be measured in-situ at Earth and and subsequently traced back to their origin at the sun.

- These energetic particles present significant complications for space-based technology and present a radiation exposure risk for people and equipment both in space and, for the largest events, on Earth.

As a result, understanding of these particle events is critical to help clarify the influence of solar transient events on the heliospheric environment and properly determine the effects of these events on space-based technologies and potentially human life.

Early studies of these events (Reames et al. 1999 and references therein) set forth a two-class paradigm for SEP events: impulsive events, which occur over limited areas of the Sun and are often directly associated with flares (discussed previously in Section 1.2) and gradual events which originate high in the corona and are associated with shock-acceleration often from CME-driven shocks. In the paradigm, flare-associated impulsive SEP were shown to have enhanced heavy-ion and ^{3}He abundances above those of the typical solar wind, while the composition of gradual shock-accelerated events was believed to be that of ambient coronal plasma with solar wind abundances. This implies that the highest energy particles and the ones of most concern to the Sun-Earth environment were primarily association with the smaller scale impulsive events.

In-situ measurements from instruments, like those aboard the Advanced Composition Explorer (ACE: Stone et al., 1998), have blurred these distinctions between gradual and impulsive SEP events. These observations show that gradual events also exhibit heavy element enhancements, indicating that shock-accelerated events can accelerate the high energy particles previously associated with flare acceleration. As a result, the largest SEPs, almost all of which are classified as gradual events, can produce accelerated particles up to GEV energies which have the most direct consequences on the heliospheric environment. Recent studies of large gradual events (Desai et al., 2006: Tylka et al., 2005; Tylka and Lee, 2006) have attempted to explain

this enhanced component of the particle population associated with large gradual SEP (LSEP) events, and have posed two competing theories to explain the observations:

- Tylka et al. (2005) and Desai et al. (2006) have suggested that remnant suprathermals from previous flare accelerated populations in the corona can provide a significant component of the particles accelerated by the CME-associated events.

- In contrast Cane et al. (2003, 2006) posit that the enhancements result from a direct flare component and that the variations in observed SEP abundances and spectra depend on the strength of the flare component, the strength of the shock, and the strength of the magnetic connection between the event-associated region on the solar surface and the Earth.

Further description of these events and discussion of the importance of solar activity and the solar environment will be presented in Section 2.3 leading to our study of the influences of solar magnetic configuration and flare productivity on the observed SEP abundances, discussed in Chapter 6.

Chapter 2
Project Background and Motivation

This chapter describes the key issues and questions and physical understandings which lead directly to the research in the later chapters of this thesis. We discuss here the relevant background of previous studies and how the work presented here builds on this existing framework. To accomplish this, the chapter is presented in 3 parts:

- Section 2.1.1 discusses the historical context of temporal and spatial studies of solar flares while also highlighting the relevant physical concepts and modeling concerns. This largely serves as background for the UV/HXR investigation discussed in Chapter 4.

- Section 2.2 describes the importance of the solar magnetic field in initiating and governing the flaring process. Within this section we address the importance of magnetic topology in the flaring process. We highlight magnetic reconnection as a key physical processes in the flare energy release. We describe the nature and role of separatrix surfaces in defining the 3-D solar field and discuss the implications of their interaction, often at separators, in relation to observed chromospheric signatures.

- Finally we discuss the relevant background in recent SEP studies and discuss viable solar environment variation which may influence the nature of the SEP

composition measured in-situ at ACE.

2.1 Solar Flare Introduction

Solar flares are most easily described as localized, explosive energy release events, freeing up some 10^{32} 10^{33} ergs per second of energy for the largest events (Emslie et al. 2004). Solar flares predominantly occur within active regions, regions on the solar surface dominated by strong emergent magnetic field visibly defined by complex sunspot groups in the photosphere. Flares are the observable manifestation of the relaxation of a complex magnetic field from a non-potential state, releasing significant magnetic energy in the process. The magnetic energy is released quickly via magnetic reconnection which will be explained in more detail in section 2.2.1. Flares show emission signatures covering the full electromagnetic spectrum from gamma rays for the largest events to bursts of radio emissions. For the work within this study, we concentrate on emission in the ultraviolet (UV), extreme ultraviolet (EUV), and hard X-rays (HXR). While, in the case of the UV and EUV the exact production mechanism remains unclear, many physical constraints can be determined from the analysis of temporal profiles and the evolution of the flares. Most critically, comparison of the temporal profiles of the observed emission in the various wavelengths can link signatures with co-temporal burst features to the same initial magnetic energy release. This connection primarily drives the study of temporal relationships in flares as it provides critical insight into the potential physical origins of the energy release

in the corona.

2.1.1 Solar Flare Temporal Studies

Chapter 4 will discuss our research into the temporal and spatial relationship between various emission signatures resulting from the chromospheric response to the flare energy release. Initial temporal studies of broadband EUV and hard X-ray emissions, based on observations from the OGO satellites and ground-based sudden frequency deviation (SFD) observations in the ionosphere for EUV wavelengths at 10 1030 Å (Kane and Donnelly, 1971; Donnelly and Kane, 1978; Kane, Frost, and Donnelly, 1979). In these studies, they analyzed a number of flares of varied intensities during the period 1967 to 1969 using ionization chamber data from OGO-1 and OGO-3 and NaI scintillation chamber data from OGO-5. The data presented were measurements from the scintillation chamber on OGO-5, which collected hard X-ray data in eight channels (9.6-19.2, 19.2-32, 32-48, 48-64, 64-80, 80-104, 104-128, >128keV) with a temporal resolution of 2.3 seconds, and broadband EUV time profiles obtained from SFD observations with a time resolution of approximately one second.

The results of three such flares are shown in Figure 2.1. Each event shows a similar rise phase in both wavelengths (pictured are the 9.6-19.2 and 19.2-32 keV channels). The analysis is limited to this part of each of the flares partially due to a desire to focus on the impulsive phase of the flare, but also due to unreliability in SFD data during the decay phase.

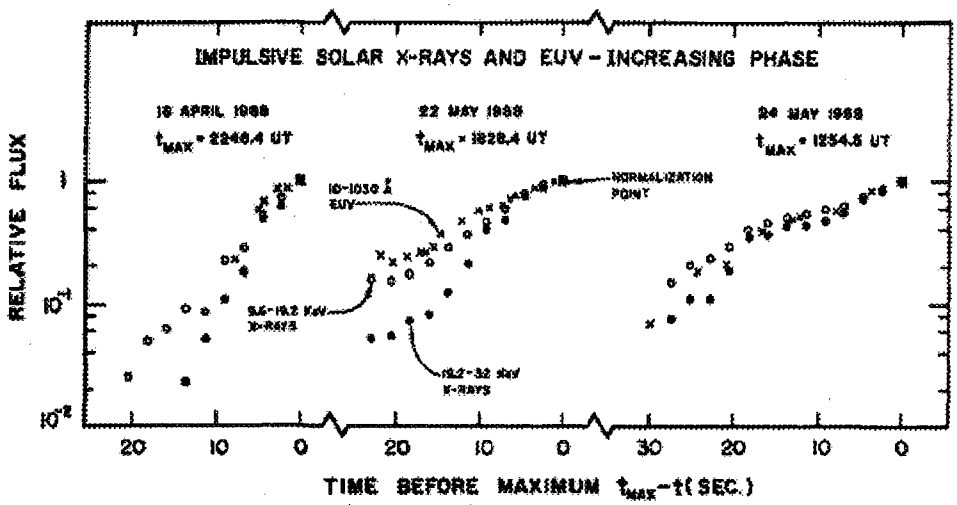

Figure 2.1 Figure 2 from Kane and Donnelly, 1971 showing comparisons of the impulsive rise of three flares in broadband EUV, 9.6-19.2 keV X-rays, and 19.2-32 keV X-rays.

From these observations, Kane, Frost, and Donnelly (1979) posited a model of partial precipitation of energetic electrons to reproduce the UV-HXR relationship, theorizing that hard X-ray sources are produced through thick-target bremsstrahlung in the chromosphere while the EUV emission originates from chromospheric heating resulting from the kinetic energy transfer from the precipitated, non-thermal, electrons into the high-density chromosphere, predominantly via Coulomb collisions. This partial precipitation model invokes three density regions and a strongly converging magnetic field to produce the observed X-ray footpoint and EUV emission. The Kane et al. model describes the flare as a single magnetic loop with the magnetic field converging with atmospheric depth. The non-thermal electrons are injected in

the low-density corona and travel along the magnetic field toward one of two higher density regions, the flare footpoints. Some of the particles mirror in the higher density regions dependent on their pitch angle and the geometric variations in the magnetic field. The loop structures serve as magnetic traps for particles with pitch angles larger than the loss cone angle, θ_L defined in Section 1.1.1. The electrons which reach the chromosphere do so through either direct precipitation, when their initial pitch angles are less than the loss cone angle, θ_L, or as part of an initially trapped population which is eventually scattered from the trap by means of Coulomb collisions or other mechanisms. Those electrons reaching the medium density chromospheric region produce hard X-rays through bremsstrahlung emission (see Section 2.1.4) while those precipitating to the high-density chromosphere produce UV and EUV emission through bulk chromospheric heating.

Hard X-ray emission sources are also seen in the low density corona (Masuda et al. 1994) and are expected, in simple flare models, to be produced by electrons trapped in the medium density region through thin-target bremsstrahlung emission discussed in Section 2.1.4. Refinement of trap-plus-precipitation model continued throughout the 1980's and 1990's (MacKinnon et al., 1983; MacKinnon, 1988; Spicer and Emslie, 1988; McClements, 1990; Alexander, 1990; Bespalov et al., 1991; Mandzhavidze and Ramaty 1992; Alexander and Metcalf, 1997). These models were able to reproduce the observed HXR fluxes in the flare footpoints while also reproducing observed coronal

X-ray signatures, from the trapped particles.

After the launch of the Solar Maximum Mission (SMM) in 1980, the question of UV-HXR relationships continued to be a prominent focus in solar flare studies. Cheng et al. (1988) studied predominantly the temporal relationships between these wavelengths as the instruments on board SMM lacked imaging capability for hard X-ray sources above $\sim$ 30 keV. The Hard X-ray Imaging Spectrometer (HXIS) imaged lower energy X-rays, from 8-30 keV, where a significant thermal spectral component making the non-thermal flare signatures difficult to isolate. The UV images were taken by the SMM/UVSP with a field of view of 30x30 arcseconds square. The UV data concentrated on the OV line at 1371 Å and a wide-band UV continuum measurement around 1388 Å (Cheng et al, 1988). For each event studied, the time signatures for the hard X-rays were compared through temporal cross-correlation analysis with both the UV continuum and the OV line, permitting a determination of any time lags between the various emissions.

Sample data from the Cheng et al. studies (Figure 2.2) show a strong correlation in the impulsive bursts at all three wavelengths. Within the time resolution of this study (0.128 seconds), they report a 0.3 to 0.7 second time lag between the UV and hard X-ray peaks with the X-rays leading the UV emission. They also found that the correlation coefficient varies with the progression of the flare through a series of bursts with the strongest correlation being coincident with the peak burst of the hard

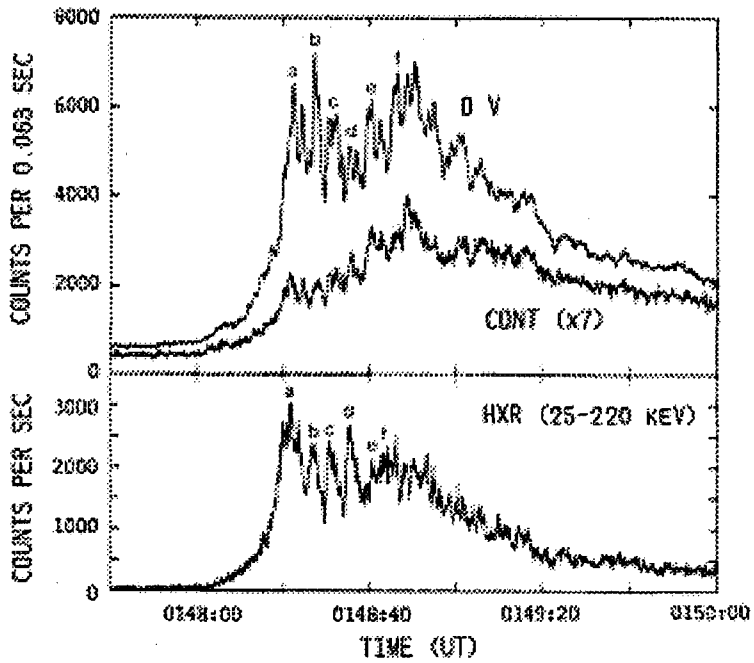

Figure 2.2 Example lightcurves of a May 24, 1985 flare from Cheng et al (1998). The labeled bursts are corresponding pulses in all three wavelengths.

X-rays. Analysis of these individual bursts is a key piece in completing the temporal development picture, and is a prominent aspect on which the study discussed in this thesis will build. Cheng et al. (1988) also demonstrated the existence of spatially localized UV and HXR emission. They reported that the majority of the sources observed in the UV were approximately 4 arcseconds, with 1 arcsecond equaling approximately 727 km in width. The 4 arcsecond UV resolution corresponds to the UVSP instrument resolution (images focused on the Si IV lines). The motions of these sources provide evidence for the commonly held belief that these UV kernels

were footpoints at the base of the flaring coronal loops. These UV kernels can be viewed as individual sources which correspond to specific brightening peaks within the UV lightcurve (Cheng et al., 1981; 1988).

Addressing the physical processes behind these results, Cheng et al. (1988) compared their UV line and continuum emission observations with the predictions of a number of models for hard X-ray and UV production. The results of these comparisons will be addressed in Section 2.1.3.

2.1.2 Studies Incorporating Spatial Development

Solar flare research advanced in the 1990's in part through the launch of the YOHKOH and TRACE missions (SOHO was not largely focused on flares although it has significantly contributed to transient phenomena research in collaboration with other missions). These spacecraft greatly improved spatial and spectral resolution, at their respective wavelengths, over those available with SMM. TRACE images in a number of UV wavelengths with a spatial resolution of approximately 1 arcsecond, imaging every 1 to 2 seconds at its highest cadence (Handy et al. 1999). The YOHKOH spacecraft and in particular the Hard X-ray Telescope (HXT) instrument allowed for hard X-ray imaging in 4 X-ray channels (Lo: 13-23 keV, M1: 23-33 keV, M2: 33-53 keV, and Hi: 53-93 keV). Details on the Yohkoh mission can be found in Tsuneta et al. (1991) and Kosugi et al. (1991). Warren and Warshall (2001) revisited the relationships between UV and hard X-ray emission in flares incorporating

these improved datasets. They presented results of nine flares exhibiting coincident flare emission in the UV continuum TRACE observations (peaking at 1600Å) and in YOHKOH/HXT, with additional flares observed in HXR data from the Burst and Transient Source Experiment, (BATSE) a hard X-ray instrument on board the Compton Gamma Ray Observatory for events where YOHKOH data for both the rise phase and peak times were not available. Figure 2.3 provides an example of Warren and Warshall's data comparing the lightcurves of six identified UV sources from an M1.1 flare occurring on 17 March 2000 with the composite hard X-ray lightcurve from BATSE data in the 25-50 and 50-100 keV channels.

The temporal correlation analysis of the sources shown in Figure 2.3 indicated a strong correlation between UV sources with minimal pre-flare emission active at X-ray onset (sources D and E) and the hard X-ray emission, but no correlation and, in some cases, an anti-correlation between UV and hard X-ray sources that exhibited significant precursor activity (Warren and Warshall, 2001). Of the nine events studied, five were observed with HXT, allowing for spatial resolution of the hard X-ray sources to within approximately 8 arcseconds. Two flares observed under these conditions were provided as examples of the spatial separation between the HXR emission sources and the UV brightenings. This separation suggests a more complex configuration than the single loop, often invoked by simple models, can provide. Figure 2.4 contains two UV images from TRACE with overlaid contours from the HXT data. The first image

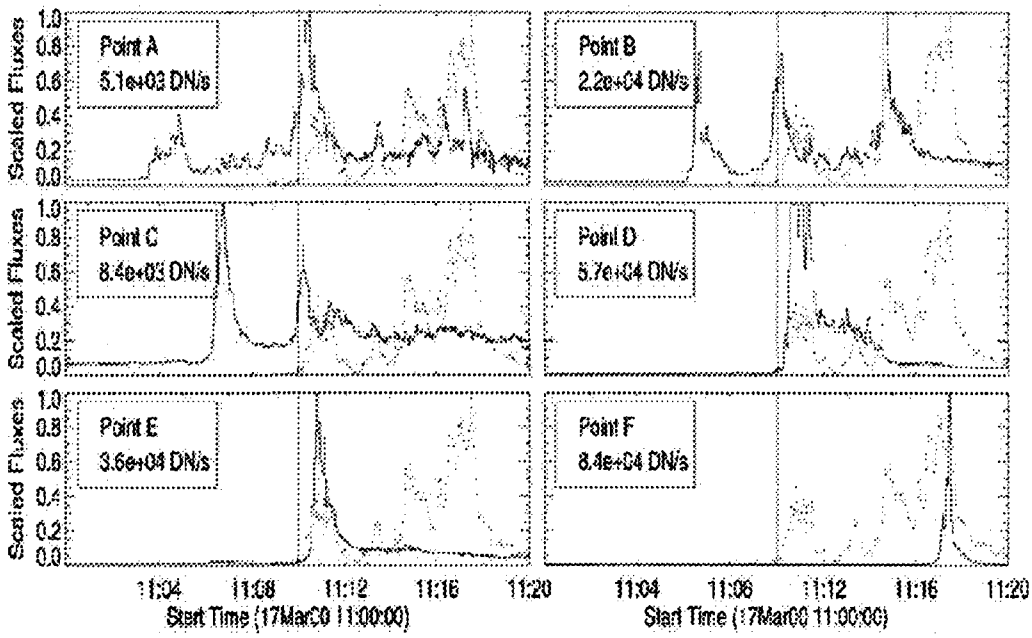

Figure 2.3 Comparative lightcurves of a March 17, 2000 flare (TRACE curve in foreground). Analysis of these lightcurves indicates a correlation between hard X-ray sources and UV sources which showed no preflare emission. (Warren and Warshall, 2001)

shows the initial UV ribbons prior to the onset of hard X-ray production while the second is a snapshot from near the onset of initial hard X-ray burst. While the UV emission exhibited extended, brightened, flare ribbon structures, the HXR bursts appeared concentrated at one end of the central ribbon.

2.1.3 Implications for Energization Models

Due to the complexity of the energization process of solar flares, a variety of models have been proposed to reproduce the observed relationships between emissions at

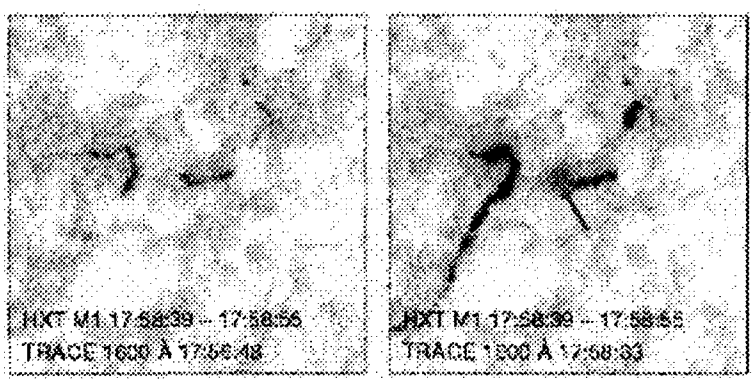

Figure 2.4 TRACE UV images from the 22 January 2000 flare in the study. The left image shows the development of a UV ribbon structure prior to the onset of hard X-ray emission. The right image is taken during the initial hard X-ray burst. The hard X-ray emissions are clearly more localized than the UV emission (Warren and Warshall, 2001)

different wavelengths. As instrumentation has improved, observational constraints on flare emission have become more stringent. Temporal profiles have sufficient resolution to determine the lag times between the emissions and constrain whether they are the results of a common impulsive origin or not, while observations of the spatial separation of temporally correlated emissions at various wavelengths have suggested a need for a more complex magnetic topology to allow for energy deposition consistent

with the spatial distributions found. Observations of UV and HXR emission being temporally correlated to within 1 second (Cheng et al. 1988, Woodgate et al. 1983) rules out thermal conduction models, such as those put forth by Brown, Melrose, and Spicer (1979) and Smith and Lilliequist (1979) for these temporally coincident sources. Thermal conduction fronts travel at the local sound speed which is around 300 km/s within the corona. Consequently, these models require delays of 6-20 seconds for the UV emission relative to the hard X-rays (Woodgate et al 1983) to travel from the apex of coronal loops in the corona, the proposed location for the energy release, and the base of the loops in the chromosphere where the UV emission is produced. This model assumes that the HXR emission results from particles which reach the chromosphere in approximately 0.1 seconds while the UV emission arises from a later developing thermal conduction fronts.

Cheng et al. (1988) also compared their time delay observations to other models including non-thermal electron beams, hole boring, in which an initial beam creates a high-temperature and low-density channel in which subsequent beam electrons precipitate (Cheng et al, 1988), and Alfvén wave heating (Emslie and Sturrock, 1982). All of the models tested were unable to sufficiently reproduce observations given the timing, density, and spectral constraints. The difficulties inherent to these models include the ability to generate enough energy at the needed chromospheric depths to produce the UV continuum emission and the ability to reproduce the observed

temporal correlations. In addition, the results of Warren and Warshall (2001) raise critical questions regarding the spatial structure and topology of the flaring regions. The spatially-extended nature of the UV emission suggests that the flare consists of a more complicated topology than a single loop structure, while the precursor emission raises the possibility of multiple mechanisms being necessary to reproduce the observed emission in its entirety. Observations presented in this thesis utilize the improved spatial resolution provided by the Ramaty High Energy Solar Spectroscopic Imager (RHESSI: Lin et al., 2002) to investigate the spatial component of the UV/HXR relationship with higher resolution than previously available. The combination of RHESSI and TRACE provides a significant opportunity to probe small scale structure within both the UV and the hard X-ray sources and observe any notable spatial separations between the emitting regions. The time resolution improvements of RHESSI present an opportunity to refine the timing relationships reported by Warren and Warshall (2001) with improved accuracy to verify and extend the correlation work.

Observations in other wavelengths, such as Hα (Kitahara and Kurokawa, 1990), have shown that localized sources of chromospheric emission within the same flare can have widely varying time profiles with the disparate Hα profile types being temporally associated with emissions including hard X-rays, soft X-rays, X-ray emission under 10 keV, and thermal conduction fronts. The temporal and spatial resolution of RHESSI

and TRACE allow us to analyze individually localized UV sources to investigate whether a similar variety of responses is observed in the UV. Correlations to additional types of emission suggest that multiple physical mechanisms as well as varied particle populations may be involved in creating the complex emission signatures seen in flares.

2.1.4 X-ray Emission from Bremsstrahlung Radiation

X-ray emission in the atmosphere is a direct result of the acceleration of high-energy particles. The specific mechanism for hard X-ray production in the chromosphere, and soft X-ray emission in the corona, has been shown to be bremsstrahlung radiation, also called braking radiation or free-free emission. Bremsstrahlung emission arises from the interaction of accelerated electrons with other charged particles in the solar atmosphere to produce the observed X-ray emission. These interactions result from interaction of two passing unbound charged particles, predominantly, a fast-moving electron with an ambient, relatively stationary, ion. These interactions are governed by the bremsstrahlung cross-section of the non-relativistic electrons for scattering from free ions given by the Bethe-Heitler cross-section:

$$\sigma_B(\varepsilon, E) = \frac{7.9 \times 10^{-25}\overline{Z^2}}{\varepsilon E}\ ln\frac{1+(1-\frac{\varepsilon}{E})^{\frac{1}{2}}}{1-(1-\frac{\varepsilon}{E})^{\frac{1}{2}}} \quad cm^2 keV^{-1}, \tag{2.1}$$

where ε is the photon energy, E is the energy of the accelerated electron, and $\overline{Z^2}$ is the average atomic number of the plasma, taking into account the elemental abundances

and the composition of the plasma. For solar composition, Z^2 is approximately 1.4.

In the solar atmosphere bremsstrahlung radiation is generally described in two different ways, *thick-target bremsstrahlung* and *thin-target bremsstrahlung*. Thick-target bremsstrahlung (Brown, 1971; Brown and McClymont, 1975) occurs in regions where the target is sufficiently dense enough to completely stop, i.e. thermalize, the accelerated electrons. Thick-target emission is generally believed responsible for the hard X-ray footpoint emissions in the chromosphere. The non-thermal, high-energy electron beams travel through the corona and lose all of their energy in the higher density layers in the chromosphere. Approximately 10^{-5} of that energy is emitted through bremsstrahlung. The rest of the energy goes into heating the chromosphere and producing additional flare emission signatures. In contrast, thin-target emission occurs in low-density regions where the electron distribution of the beams are unchanged as they propagate through the target (Wheatland and Melrose, 1995). Thin-target emission occurs largely in the corona where the plasma is tenuous and thus loss of energy due to collisions is rare. Within many flare models, this type of bremsstrahlung is responsible for the non-thermal component soft X-ray emission in the corona (Benz, 2008).

A key difference between the thin and thick target scenarios is the hardness of the resulting photon spectrum for a given electron injection profile, often, within non-thermal electron beams, assumed to be a power law proportional to $E^{-\delta}$. The photon

spectrum can be determined from:

$$I(\varepsilon) = \frac{S}{4\pi R^2} \frac{1}{2\pi e^4 ln\Lambda} \int_{\varepsilon}^{\infty} F(E_0) \int_{\varepsilon}^{E_0} E\sigma_B(\varepsilon, E) dE dE_0 \tag{2.2}$$

where σ_B is the bremsstrahlung cross-section given by Equation 2.1, ε is the photon energy as before, E is the electron energy, R is 1 AU, and S is the flare area. The parameter ln Λ is the Coulomb logarithm, which is defined by the collisional properties of the plasma. Its logarithmic dependence varies slowly enough that it is generally taken as a constant with a value of 10-20 for solar flares. I(ε) is the photon intensity distribution. It has been shown that given an electron power law distribution, both the thick-target and thin-target cases also produce power laws, of the form $\varepsilon^{-\gamma}$, only with different power law indices, γ. The power law indices relate directly to the electron distribution: for the thick-target case (Brown, 1971)

$$\gamma_{thick} = \delta - 1 \tag{2.3}$$

and for the thin-target case:

$$\gamma_{thin} = \delta + 1 \tag{2.4}$$

In terms of the X-ray spectrum for a typical flare we find low energies, < 25 keV, dominated by a thermal component which is in the form of a Maxwell-Boltzmann distribution, with a peak temperature of $\sim$ 35MK, and, high energies, dominated by a hard power law spectrum consistent with the thick target emission for energies above 25 keV. We focus the work here on hard X-rays from 25-100 keV that are more directly linked to impulsive flare behavior.

2.2 Importance of Magnetic Topology in Influencing the Behavior of Solar Transients

Solar flares and CMEs are visible manifestations of rapid energy release from the solar corona and specifically the coronal magnetic field. These transients originate from areas of strong and complex magnetic fields known as active regions. Typically, active regions associated with significant flare and CME productivity are often distinguished in white light images by complex sunspot groups (Tian et al. 2005; Tian and Alexander, 2006). These complex field regions store vast amounts of energy as currents within a non-potential configuration. Like many physical systems however, this non-potential magnetic field is naturally driven to lower energy states and subsequently releases magnetic free energy whenever an appropriate mechanism and trigger are presented. This energy release manifests itself in a number of observable processes: particle production, bulk coronal heating, dynamic motions, and emission signatures covering the entirety of the electromagnetic spectrum. A complete understanding of the solar flare and CMEs processes requires that we address both the mechanism governing the release, believed to be magnetic reconnection, as well as the topological constraints that are necessary to address the emission and morphological constraints that are observed.

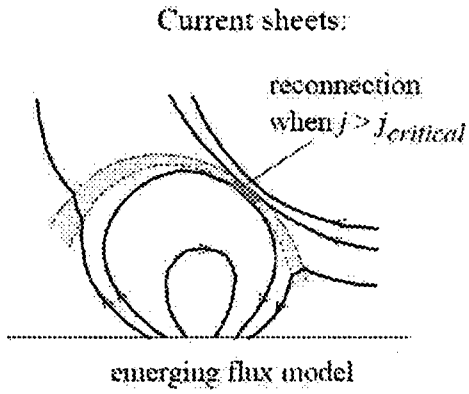

Figure 2.5 Schematic of reconnection at a current sheet taken from Forbes (2006).

2.2.1 Magnetic Reconnection in Flares

A key process in flare models is magnetic reconnection which is invoked to release and redistribute magnetic free energy in the corona. Reconnection occurs when two magnetic regions of opposite polarity interact allowing plasma to diffuse across the field and reconfigure the magnetic connectivity in such a manner as to release free magnetic energy often via formation of a current sheet, a 2-dimensional structure developing within the coronal magnetic field where electric currents accumulate. When the currents in these current sheets exceeds a critical value, allowing for particle diffusion to occur across oppositely directed field, reconnection occurs and magnetic energy is released (see Figure 2.5 In 2-D scenarios, reconnection is most often explained via two common mechanisms: Sweet-Parker reconnection (Sweet, 1958 and Parker 1963) and Petschek reconnection (Petschek, 1964). Detailed discussion of both

these processes are present in Chapter 10 of Aschwanden (2004). Both these 2-D models struggle to account for reconnection in flares with Sweet-Parker reconnection not reconnecting fast enough and Petschek reconnection struggling to reconnect sufficient portions of the coronal plasma (Aschwanden, 2004).

Recently, a number of 3-D models have been developed that appear to explain the various aspects of flare reconnection. Among the most common of these are X-type reconnection and separator reconnection. Typical flare scenarios, such as those depicted by Figure 1.6, suggest that X-type reconnection is appropriate, i.e. two oppositely directed open field regions are brought together and interact at an X-point in the corona. A number of X-type reconnection scenarios are described in a recent review by Aschwanden (see §2 from Aschwanden (2002) and the references therein). These scenarios are schematically shown in Figure 2.6. The key aspects of each of these scenarios involve variations in the field-line connectivities between oppositely oriented field, whether they be open field, which connects the sun magnetically to interplanetary space, or closed field loops, which have both of their footpoints anchored to the solar surface. In the scenario from Tsuneta (1997), two open field lines reconnect in the corona above the observed neutral line inferred from chromospheric observations and line-of-sight magnetograms. The neutral lines serve as key locations for reconnection because they are logical points for the easy interaction of opposite polarity field. The result of the reconnection is a smaller closed loop which entrains

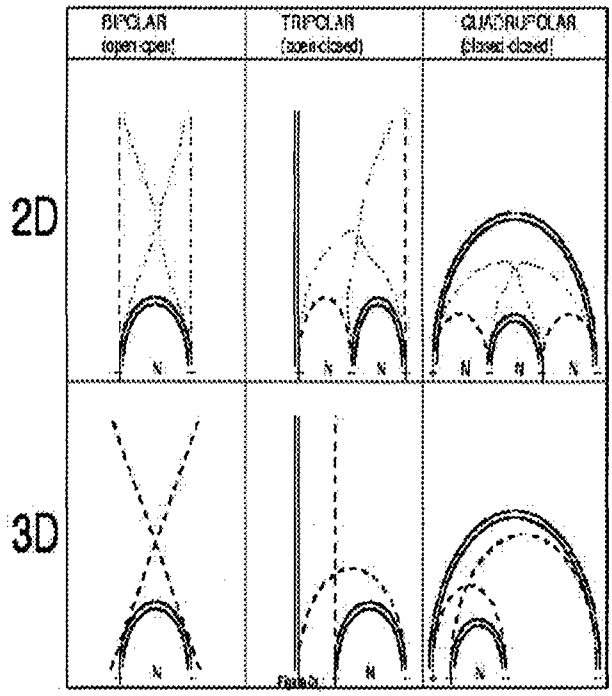

Figure 2.6 Schematic diagrams of bipolar, tripolar, and quadrupolar configurations for magnetic reconnection in 2-D and 3-D cases. Figure taken from Aschwanden (2002)

coronal plasma and facilitates particle transport into the chromosphere. More complex scenarios, the tripolar and quadrupolar cases, involve the interaction of one or more closed magnetic structures. In these scenarios, the closed loops are temporally opened by reconnection before settling into a largely closed topology. In each case, reconnection results in the coronal magnetic field relaxing into a more potential state due to the transfer of energy from the magnetic field to observable flare signatures.

Another more complex means of 3-D reconnection is reconnection along a specialized field line known as a *separator*. Separators, to be discussed further in the next section, are boundaries of 3-D flux systems known as *separatrices*. These surfaces divide the active regions into well-defined flux systems. As such, their boundaries form ideal locations for interaction and reconnection. Reconnection at these boundaries evolves with the flare based on the development of current sheets within the solar corona.

2.2.2 Separators, Separatrices and QSLs

Separators and separatrix surfaces are a viable means of explaining the cause and locations of magnetic energy release while addressing the link between the release trigger and the chromospheric flare signatures. Separatrix surfaces are 3-D surfaces which divide the flaring region into independent self-contained flux systems. The boundaries of these systems, specialized field lines known as separators, are defined by discontinuous mapping of the field in the flare region. The locations of the discontinuities are determined from the solution to the equation

$$\frac{dr(s)}{ds} = \frac{B(r(s))}{|B(r(s))|} \tag{2.5}$$

where B(r(s)) is the magnetic field value at a point r(s) along the field line, r(s) is a coordinate along the field such that $\frac{dr}{ds}$ is tangent to the field line, and s is the position along the line (Longcope, 1996). Due to the discontinuities described, these separators mark likely locations within the complex flaring region for reconnection

to occur. Separators act as 3D extensions of magnetic null points, locations in the magnetic field where the field is zero, and mark the boundaries between oppositely directed flux systems. These boundaries at separators allow particles to diffuse into oppositely directed field allowing for reconnection to occur and changing the overall connectivities of the magnetic topology.

Frequently, in lieu of complete discontinuities, reconnection occurs in regions called *quasi-separatrix layers*, hereafter *QSLs* (Démoulin et al., 1993; Titov et al., 2002; Wang et al., 2000). QSLs are defined not by complete discontinuities but by steep gradients in the magnetic field producing a similar effect as the pure separator system, only with a less stringent boundary condition (Priest and Démoulin,1995; Démoulin et al., 1996). A critical complication arises in the determination of separators and QSLs in that the magnetic fields in the corona are not measurable. Consequently, these fields must be extrapolated from the measurable fields in the photosphere. The photospheric field serves as a valid boundary condition because the chromosphere and corona are magnetically-dominated plasmas where the particle motions are governed by the magnetic fields. From these field extrapolations, we calculate the boundaries of QSLs using a calculation of the *norm*, which takes into account all the local gradients to provide a quantitative indication of the existence and strength of a QSL at a given location. The norm, however, often double counts gradients as it fails to take into account that each field line has two footpoints. To correct this, Titov et al. (2002)

discuss a *squashing degree factor, Q,* as an improvement upon the norm calculation designed to incorporate multiple mappings from given footpoints in the tracing of the field line mapping. The mathematical forms for the norm and the squashing factor will be presented in Section 5.1 as they are applied directly to observations.

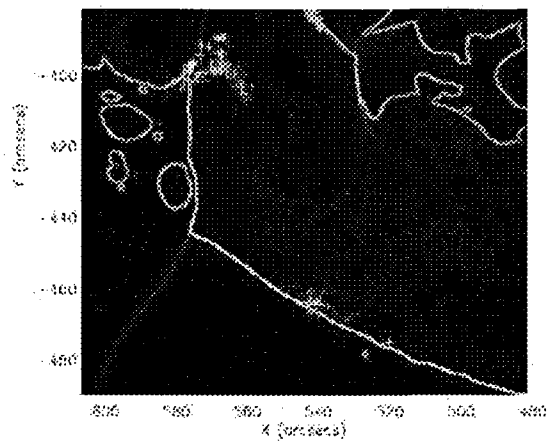

Figure 2.7 Map of the positions of hard X-ray emission sources relative to calculated separatrix surface boundaries for a white light flare from 25 Aug 2001

An important aspect of the separator analysis we address in this work is the connection between the 3-D separatrix surfaces and the locations of chromospheric emission signatures. Ribbons of emission in wavelengths such as H α, O V, and UV continuum emission have been shown in a number of observational studies to occur near the intersections of the separatix surface boundaries with the chromosphere (Démoulin et al, 1993; Loncope, 1996). Metcalf et al. (2003) traced the evolution of hard X-ray emission sources over the course of a large flare and found that the

X-ray sources generally track along and near the separatrix surface intersections with the chromosphere (see Figure 2.7). A further understanding of separators, QSLs and their evolution would require an understanding of the evolution of the chromospheric emissions and the relationship to the evolving magnetic field structures. In Chapter 5 of this thesis, we present a study tracing the evolution of chromospheric hard X-ray emission for two events from NOAA active region 10720. We compare the resulting distribution of HXR sources over time to the distribution QSLs in the solar magnetic field as determined from calculation of the squashing factor, Q.

2.3 Solar Energetic Particle Study Motivation

In Chapter 1, we discussed solar energetic particles as a key link between solar activity and the Earth environment. This section will provide a background for the study of the particle events relative to the activity occurring at the sun providing a key starting point for our investigations into SEPs and the solar magnetic fields.

2.3.1 Brief History of SEP observations

Originally seen as early as the 1940s, SEPs have always been associated with impulsive solar transient events. However, these early observations were assumed to result only from solar flares. Beginning in the 1980s, a two-class paradigm for SEP events began to take shape, replacing the flare-only scenario. In this picture, numerous, smaller, more localized, and shorter, usually on timescales of hours, SEP

events are associated with flares while larger SEP events, lasting periods of days and having greater spatial extent, are more directly linked to CME-associated shock acceleration (Reames, 1999 and references therein). Among the crucial diagnostics to distinguish one class of event from another, are elemental abundance ratios particularly the $^3He/^4He$ ratios and the heavy element ratios, such as Fe/O or Fe/C. In general, so-called "impulsive" events are confined to small regions of the Sun and generally show enhancements in both Fe/O and $^3He/^4He$. $^3He/^4He$ ratios and Fe/O ratios of order unity are typical values for impulsive events (Cohen, 2006). In contrast, shock-accelerated or "gradual" events were believed, in this paradigm, to result from the shock acceleration of particle populations of typical coronal abundances, Fe/O ratios approximately 0.134. Therefore, the elemental abundance ratios were believed to be consistent with standard coronal values.

Until the launch of the Advanced Composition Explorer (ACE; Stone et al., 1998), these classes were largely thought to be mutually exclusive with the solar wind particles only contributing to gradual events and flare particles only contributing during impulsive events. In-situ observations from the instruments on board ACE, the Ultra Low Energy Isotope Spectrometer (ULEIS) and the Solar Isotope Spectrometer (SIS), have blurred the lines of separation between the two classes. Studies of large, gradual SEP events (Tylka et al 2005; Desai et al 2006; Cane et al, 2006) have shown these events to have a mixed composition. While many events show the same solar

wind abundances expected for gradual events in the two-class paradigm, a number of events show significant enhancements in heavier elements and helium ratios, more consistent with the particle population seen in flare-accelerated events. Given the typical shock acceleration picture, much of the particle composition variations at low energies would result from the available particles to be accelerated, known as the seed population. These observations suggest that the seed population contains a component of particles from previous flares. This is necessary to produce the flare-like enhancements despite predominantly being shock-accelerated gradual events.

2.3.2 Connecting SEP observations to Solar Characteristics

One further aspect of SEP characteristics is the observed variation of the compositional ratios with increased energy. The explanation for these variations in composition with energy is a subject of great contention within the SEP research community. One proposed theory put forth by Tylka and Lee (2005) posits that the available seed population contains a small but significant fraction of flare suprathermals, preferentially shock-accelerated by quasi-perpendicularly oriented shocks, as defined by the angle between the magnetic field and the shock normal. These quasi-perpendicular shocks exhibit more rapid acceleration (Jokipii, 1982 Giacalone, 2005) but required particles with higher initial speeds (Forman and Webb, 1985; Jokipii, 1987) to fully take advantage of the rapid acceleration. As a result, events with quasi-perpendicular shock orientation would more rapidly accelerate solar energetic particles which be-

gin with higher initial speeds and energies. Therefore, quasi-perp events show enhancements similar to those in flare-accelerated impulsive events because the flare suprathermal component, having been previous accelerated by an earlier flare event, will possess the higher speeds necessary. In contrast, a similar event with a quasi-parallel shock orientation will pick up, for the most part, the typical coronal particles often associated with the solar wind.

In a competing theory, Cane et al. (2003, 2006) have suggested that a direct flare component and a shock-accelerated component of the seed population always exists with the dominant component being dependent on the physical properties of both the flare and the shock. These properties include the strength of the flare, the ease with which particles can reach Earth, called the connectedness of the flare, as well as the strength of the shock, and the energy of the particles being accelerated.

The need to explain the variety of observed abundance ratios and the wide array of behaviors with increasing energy has made it necessary to explore the variations in the pre-event solar environment to determine what role the ambient solar conditions and pre-event activity have in shaping the seed populations and particle transport for these events. The catalyst for this discussion stems specifically from the consideration of two large gradual SEP events from 21 April and 24 August in 2002. Both events were associated with well-connected west limb X-class flares of similar intensity (21 April is an X1 flare while 24 August is an X3). As shown in Figure 2.8, the composition of the

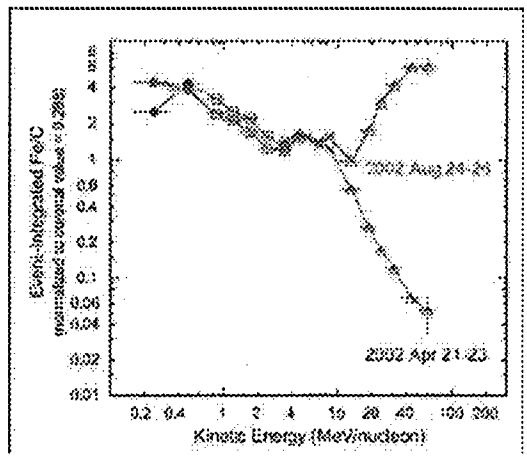

Figure 2.8 Comparison of Fe/C ratios with energy for two large SEP events with similar flare and CME characteristics from 21 April and 24 August 2002. At high energies, above 10 MeV/nucleon, The Fe/C ratio diverges for the two events with iron preferentially accelerated in the August event.

observed SEPs for these events are wildly different above 10 MeV/nucleon though they both exhibit significant enhancements below 10 MeV/nuc. The 24 August event shows significant enhancements in Fe/O and Fe/C ratios with values well above coronal averages, increasing with particle energy above 10 MeV/nucleon. In contrast, the 21 April event shows a significant decrease to orders of magnitude below average coronal values for energies above 10 MeV/nucleon. For two flares that behave so similarly at the Sun to produce such varied SEP characteristics suggests that the pre-event solar conditions may have direct implications for SEP production.

Alexander et al. (2004) and Liu et al. (2004) suggested that two notable differences in the 21 April and 24 August event were the magnetic configuration of the

corona and the overall flare activity of the respective active regions. Using these two events as a starting point for the study to be presented in Chapter 6 of this thesis, we address the magnetic field configuration using potential field source surface extrapolations to determine the locations and strengths of open-field regions. These extrapolations will determine the distribution of both open and closed field structures with the solar magnetic field extended to 2.5 solar radii. Open field structures are regions of field lines which extend beyond the 2.5 solar radii limit of the extrapolation. The extrapolation is limited by a source surface developed to force the field beyond 2.5 solar radii to be purely radial, simulating the effects of the solar wind. Within the extrapolated volume, out to 2.5 solar radii, one endpoint of the open field remains disconnected provide particles a pathway to interplanetary space. We compare the composition ratios for SEPs at various energies to the available open field magnetic flux obtained by the determination of the coronal field and the area of the enclosed open-field region with the event associated active region. The open field regions provide the accelerated particles access to Earth and the heliosphere in general. As a result a comparison of open field flux to the composition ratios, measured with ACE, gives us a means to clarify, the importance of the solar magnetic field on the particle populations measured in-situ. In addition we use a modified index of flare activity based on the initial work with active regions by Abramenko (2005) to quantify the activity of the associated active region prior to the events. Due to the importance dis-

cussed previously of a potential remnant flare particle component of the accelerated particle population, we look to quantify the flare activity of each given active region and investigate the influence of flare productivity, if any, in producing the observed compositional enhancements. We will further address the methods of our SEP study in Section 3.3 and present the results of our study in Chapter 6.

2.4 Project Overview

The studies presented here incorporate aspects of solar transient activity on a variety of distance scales, from the solar surface out to 1 AU, and on timescales of seconds and minutes to interplanetary events on scales of hours and days. Both flares and SEP events provide observational windows into the always volatile Sun-Earth system and provide a unique means to analyze the physical dynamics that govern this system. The work presented here advances the study of solar transient activity in four crucial areas:

- The study of UV and HXR flares with the resolution improvements provided TRACE, in the UV, and RHESSI, in the hard X-rays, allows us to build upon the timing and spatial relationships explored in earlier studies that were constrained by limited spatial resolution. The improved resolution provides an unprecedented ability to investigate the behavior of localized structure within the flaring region and to gain unique insight into the overall development and

temporal evolution of the energy release processes and magnetic topology of a wide array of flares.

Specifically, within this study, we focus on four main extensions to the UV and HXR studies discussed previously:

- We compare the overall spatially-integrated UV and HXR response both for the full field of view TRACE data and for selected localized source in an attempt to verify the temporal correlations discussed in prior works for the overall temporal development of the flare
- Within many events, we see a number of impulsive bursts across a given time profile. We conduct a correlation analysis for localized sources with time profiles that show significant brightening for specific bursts.
- For the individual impulsive bursts within the X-ray profile, we compare the spatial distributions of active UV sources and HXR sources and posit potential physical mechanisms and topological configurations necessary to explain the observed emission.
- For some events we concentrate on select UV sources with time profiles that deviate from the previously suggested UV/HXR relationships. We perform a timing analysis between the UV and lower energy hard X-rays (6-25 keV) and suggest that the UV emission may result from processes

other than the generally assumed injection of non-thermal electrons.

- To further investigate the importance of chromospheric signatures as diagnostic for magnetic topology changes, we compare the location and evolution of HXR flare footpoints sources relative to the location of separators, determined from vector magnetogram observations, for two large flares originating in NOAA AR 10720. This allows us to trace the evolution of the HXR emission and directly investigate any connection to the magnetic evolution of this complex active region.

- We address the role that the solar magnetic configuration plays in producing the vast array of SEP signatures seen in-situ with ACE. We do so by comparing the access to interplanetary space determined by open field availability from potential field source surface extrapolations to the observed in-situ abundance ratios.

- Finally, we address the relationship between SEP composition and the overall activity history of the event-associated active region. We achieve this by determining a numerical index of flare activity based upon modifications to the work of Abramenko (2005).

Chapter 3
Instrumentation and Methodology

The multi-wavelength analysis of solar flares and SEP events presented in the later chapters of this thesis requires the combination of numerous data sets from a variety of disparate instruments and a wide range of analysis techniques to most completely address the complex nature of this activity. This chapter is designed to provide something akin to a quick reference guide for the instrumentation, data, and analysis techniques used in our work. For simplicity, the chapter will be structured to cover all the instrumentation at the onset while the methodology for the flare and SEP studies will be presented separately. In addition, the methods used will be addressed in greater detail in the relevant research chapters.

Our analysis of flares incorporates image processing, including UV and white light images from TRACE, hard X-ray image reconstructions and high temporal resolution lightcurves from RHESSI, and white-light images and line-of-sight magnetograms from MDI on board SOHO (the white light data used for co-alignment of TRACE images: see Section 3.2.4). Our SEP analysis incorporates magnetic field modeling through potential field source surface (PFSS) extrapolations based upon the line-of-sight magnetogram input from MDI and in-situ particle measurements from the Solar Isotope Spectrometer (SIS) and the Ultra Low Energy Isotope Spectrometer (ULEIS)

on board ACE. This chapter will provide the requisite information about the various spacecraft and the instrument performance required by our analysis. We also detail the data processing and analysis techniques used in our study along with discussing critical aspects of the PFSS model as a means of determining magnetic flux from SEP event-associated active regions. As a final component, we will discuss our methods for quantifying flare activity within an active region based upon archival data from GOES observations.

3.1 Instrumentation

3.1.1 TRACE

The Transition Region and Coronal Explorer (TRACE: Handy et al., 1988; 1999) is a high resolution ultraviolet and extreme ultraviolet imaging telescope which directly images the solar atmosphere through normal incidence optics on a CCD array. TRACE images plasmas from 6000K, photospheric white light, to approximately 2MK, coronal EUV line emission, covering a maximum field of view of 512"x512" with each pixel being 0.5 arcseconds ($\sim$ 350km) on a side. The small pixel size allows for a spatial resolution of approximately one arcsecond. This limited field of view only permits imaging for a small fraction of the solar surface, at best the TRACE field of view only covers approximately 9 percent of the solar disk. The lack of full-disk imaging presents instrument pointing difficulties for TRACE due to the lack of continuous solar limb observation capabilities. While many instrument-specific data

corrections are taken care of through data prepping, there persists a TRACE pointing error of 5-12 arcseconds which is not corrected for in the prepped TRACE data. This pointing error results from flexes of the metering tube which holds together the aperture and CCD components of the telescope. To correct this we apply a co-alignment process with SOHO/MDI data to incorporate the accurate pointing information of SOHO into the TRACE observations (see Section 3.2.4).

The TRACE telescope images through a 30cm aperture that is divided into 4 quadrants, 3 for EUV imaging at 171, 195, and 284Å respectively and 1 for imaging in the ultraviolet and visible light. A detailed explanation of TRACE imaging capability is discussed by Handy et al. (1998). Here, our focus is centered on the UV imaging, specifically the 1600Å observations with the white light observations providing the context for correcting the misalignment of the TRACE data. We use data collected using the Flarewatch1600 observing program originally implemented by Harry Warren (see Section 3.2.2). The 1600Å observations permit the imaging of the UV continuum with a FWHM of 245Å using a narrow-band UV filter. Images taken at this wavelength show emissions from plasma at temperatures of 10000-100000 K. The response function of this continuum filter is shown in Figure 3.1. The TRACE data taken using Flarewatch1600 uses a two-phase observing approach, requiring that the field of view of the 1600Å data vary depending on the count rate. During initial Flarewatch observations, TRACE targets a 384"x384" field of view with 0.5" pixels;

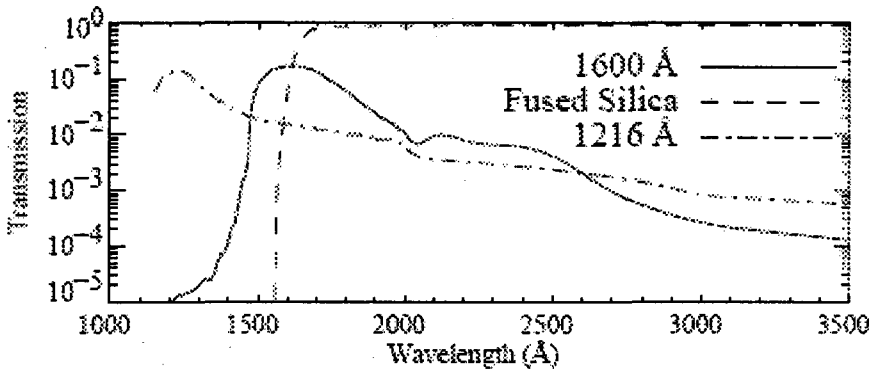

Figure 3.1 Instrumental transmission efficiency response versus wavelength for the TRACE ultraviolet (1600Å 1216Å) and white light (Fused Silica) observations. Taken from Handy et al. , 1998

however, when a count trigger is exceeded, the field of view is reduced to 256"x256" to allow for a faster cadence while maintaining the maximum resolution of approximately 1". A key aspect of this program is the time resolution it provides. During flare mode operations, 1600Å images are taken approximately every 1-2 seconds. During the pre-flare stage the cadence is approximately 4 seconds due to the larger field of view used in pre-flare imaging. In either mode, observations using Flarewatch1600 have been optimized to specifically image in the 1600Å band at cadences fast enough to capture the rapidly varying coronal conditions occurring during a flare. Typically when not in Flarewatch1600, the cadence of 1600Å observations is at best one minute when these images are included in the observing sequence. This typical slow cadence would not allow for an appropriate study of the dynamic response to the flare at UV wavelengths as in many cases only a few UV images would be taken over the course

of a flare.

In addition to the 1600Å observations, we also require white light context observations to be used for co-alignment purposes. These observations are taken with the same quadrant as the UV images using a broadband fused silica filter in place of the narrowband UV filter used earlier. The response function of both filters are shown in Figure 3.1. White light images are taken with a cadence of approximately one minute during pre-flare observations and provide a direct comparison with the SOHO/MDI white light *full disk* images. The white light data from TRACE and MDI observe the same structures but at different spatial resolution allowing us to register the TRACE data with that of MDI which has accurate pointing information. Using these common features and the accurate pointing of the SOHO spacecraft, we can correct the pointing information reported by TRACE. The specifics of the co-alignment procedure will be detailed in Section 3.2.4.

Together, the UV continuum and white light images produced by TRACE provide insight into the progression of the well-resolved UV sources both before and during the hard X-ray impulsive flare. These observations allow for a high time resolution study of the UV emission response to various portions of the flare and permit the UV emission to serve as a diagnostic and constraint for the short-timescale development of the flaring region.

3.1.2 RHESSI

The hard X-ray data presented in this work consists of observations by the Reuven Ramaty High Energy Solar Spectroscopic Imager (RHESSI). RHESSI is an X-ray and gamma ray imaging telescope with a spectral range from 3keV to 17MeV with a maximum spectral resolution of ~1keV. Physically, RHESSI is a rotating modulation collimator telescope consisting of nine germanium detectors, each with two rotating grids which control the photon transmission. Each of the detectors corresponds to a grid pair of varying coarseness, ranging in spatial resolution from 2.3 to 183 arcseconds for detectors 1 to 9. As the spacecraft rotates every 4 seconds each of the nine detectors collects a different fraction of photons from the solar source, varying with time and the orientation of the grids. Images from RHESSI are reconstructed by various transformation techniques, depending on algorithm, of the modulation patterns observed, as described in Figure 3.2.

The seven cases of modulation patterns shown in Figure 3.2 indicate how variations in source intensity, location, and spatial extent will modify the modulation patterns seen in the detector. Examples 1 and 2 show the variation in modulation pattern with intensity for point sources, with a weaker point source correspond to a less intense flux peak. Examples 3 and 4 describe variations in the vertical and horizontal location of a point source distribution. A vertical shift corresponds to a shift in the temporal profile of the modulation with the peaks shifted in time. A horizontal

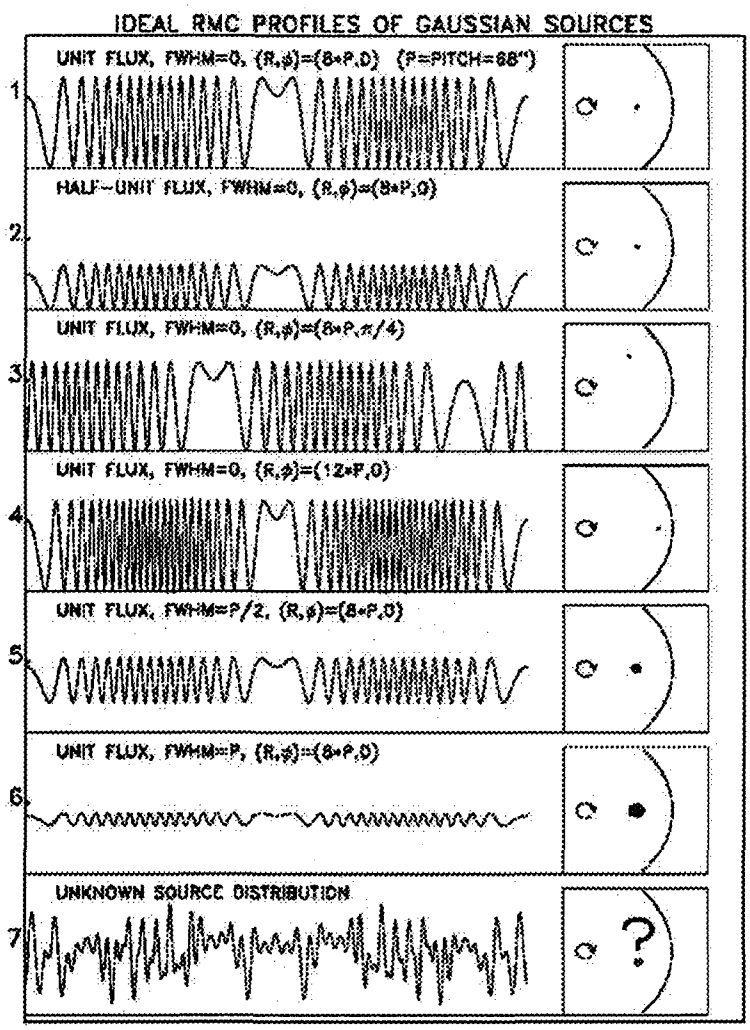

Figure 3.2 Ideal modulation patterns for a single RHESSI detector corresponding to a variety of spatial and distributions and varied source intensities.

shift reduces the period of oscillation in the modulation pattern. Examples 5 and 6 show the effects of extended sources. In both cases, the modulation peaks broaden in time due the extended nature of the source. Larger sources generally correspond to lower flux peaks. While these idealized cases make clear the effects of source variations on a detected modulation pattern; however, actual RHESSI data contains a complex spatial distribution leading to a wildly varying modulation pattern (example 7). Over the course of the integration, as counts increase, transforms of the modulation pattern allow convergence into localized hard X-ray sources reconstructing the images.

In our study the reconstructed images are created with a 128"x128" field of view centered on the flare region using pixels that are 2" on a side. Although a number of other image reconstruction techniques are available (back projection, CLEAN, maximum entropy methods), we choose to use the Pixon reconstruction algorithm (Metcalf et al. 1996) due to the improved photometry that it provides. Since the image reconstructions require sufficient counts for hard X-ray source convergence, the images require time intervals much longer than that of the direct imaging intervals used by TRACE, generally from 10 to 20 seconds for the HXR images presented in later chapter. Spatially, the HXR footpoints can be resolved to various spatial scales depending on which detectors and grid pairs are in use. The RHESSI instrument has a maximum spatial resolution of approximately two arcseconds for energies up to

100keV with the inclusion of detector 1 that uses the finest set of grids (resolution of 2.3 arcseconds).

As a consequence of the long image reconstruction time, we must limit the X-ray observations for the high cadence temporal evolution, driven by the 2-second TRACE cadence, to spatially-unresolved lightcurves. For non-imaged data, RHESSI provides a maximum temporal resolution of tens of milliseconds at all energies. Time profiles from RHESSI are produced from the measured number of photons collected for a given energy in a given time interval totaling photons from the detectors selected. The shortest time interval commonly used in the RHESSI analysis is 0.1 seconds, providing key insight into the variable injection of particles; however for most of our study these lightcurves will be rebinned to two second averages to match the cadences of the TRACE observations. The original RHESSI lightcurve with 0.1 second temporal resolution illustrates the small-scale variability in the X-ray signals likely due to a series of injections of energetic particles (see Chapters 1 and 2). Binning the data to match the TRACE resolution allows us to compare the UV and hard X-ray emission during large scale impulsive bursts. This comparison allows the investigation of the general burst characteristics of each flare.

3.1.3 Michelson Doppler Imager (MDI)

The Michelson Doppler Imager (MDI), on board the Solar and Heliospheric Observatory (SOHO) is designed to obtain magnetograms and white light intensitygrams

primarily for the entire solar disk. The MDI white light images provide a full-disk image of the solar photosphere at 4 arcsecond spatial resolution. This is significantly less than the TRACE resolution, but specific features such as sunspots, pores, and magnetic structures are clearly distinguished in both the MDI and TRACE observations. These simultaneous observations of the same structures, at approximately the same wavelength, provide selection points for image co-alignment and correction of TRACE metering tube pointing errors.

A second source of data we use from MDI for these studies is the 96-minute cadence full-disk line-of-sight magnetograms. These magnetograms aid in determining the magnetic configuration and evolution of the active regions. Changes in the magnetograms, such as an emerging flux systems, are suggestive of wide-reaching magnetic changes to the overall topology within the flare. A second application of these magnetograms relates directly to the SEP component of this thesis. The two arcsecond resolution magnetograms are combined together to create a synoptic map over a complete Carrington rotation (a 27.27 day period). This Carrington map of the solar surface radial magnetic fields (Figure 3.3) serves as the direct input for the potential field source surface models used to determine the solar magnetic connectivities associated with each SEP event (see Section 3.3.2 for a more complete explanation.)

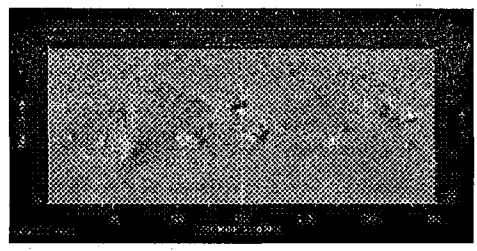

Figure 3.3 Synoptic Carrington map from SOHO/MDI for Carrington rotation 2025 (2 January 2005 to 29 January 2005) provided as a sample Carrington map of those used in the PFSS analysis

3.1.4 The Advanced Composition Explorer (ACE)

The Advanced Composition Explorer or ACE, launched in 1997, contains 6 instruments designed to the explore elemental and ionic composition for elements from helium to iron over the full range of particle energies from solar wind values, of order 1 keV/nuc, to cosmic ray energies, of order 500 MeV/nuc (Stone et al., 1998a). Of particular interest to this study are the Ultra Low Energy Isotope Spectrometer (ULEIS: Mason et al., 1998) for energies from approximately 45 keV/nuc to energies of order 1 MeV/nuc and the Solar Isotopic Spectrometer (SIS: Stone et al. 1989b) for energies from 10 to 100 MeV/nuc. The energy per nucleon measurement system is design to given all the elemental species a common scale for easy comparisons. Both of these instruments provide unique insight into the particle composition of a number of large SEP events. The in-situ measurements, particularly of helium, iron, oxygen, and carbon composition enhancements, provide critical diagnostics to distinguish the various components within the accelerated particle population. Mea-

sured values similar to those seen in the solar corona would be consistent with a picture of shock accelerated coronal material while events showing significant ^{3}He or Fe enhancements likely possess a strong component of previously accelerated flare suprathermal particles in addition to the coronal plasma population. These particles are then accelerated by the CME-associated shock driving the event. For our study we obtain ULEIS composition data from Desai et al. (2006) and SIS measurements from Tylka et al (2005).

3.2 Flare Study Methodology

Our study of solar flare observational signatures is two-fold. Primarily, we focus on determining relationships, both temporal and spatial, between the UV and hard X-ray chromospheric signatures for a wide spectrum of flares with the intent to use these relationships as constraints on the energy release mechanisms and magnetic topological configurations responsible for the observed flare emission. In addition, we look at the evolution and development of these chromospheric signatures independently with specific attention paid to determining how the evolution of the flare signatures relate to the development of the topology of the flaring region. We pay particular attention to the the development of current sheets, separators, and quasi-separatrix layers (QSLs) as discussed by Démoulin et al. (1997).

To accomplish the goals discussed requires the integration of a number of disparate datasets from varied instruments The combination of each of these into a

coherent analysis presents a number of significant steps in preparation for the complete analysis. These include defining the event selection criteria for each component of the study, selecting any appropriate observing programs necessary, developing a lightcurve analysis for the UV and HXR emission, particularly in the UV case for localized source as well as for the spatially-integrated flare, and lastly addressing the correction of uncertainties in the TRACE pointing through co-alignment with MDI white light intensitygrams. Each of these issues is critical to the analysis presented and is therefore explained in some detail below.

3.2.1 UV/HXR Event Selection Criteria

To optimize our study of UV and hard X-ray relationships in flares, our goal is to have complete high-cadence data in both wavelengths. This requires full coverage in both data sets from the initial impulsive phase through the gradual decay of the flare. To this end there are three criteria we use for event selection:

1. We select flares observed with the Flarewatch1600 observing program to ensure high cadence UV observations (see Section 3.2.2).

2. We verify that RHESSI data is available for the TRACE events selected.

3. We confirm that the hard X-ray data contains sufficient counts within the 25-100 keV energy range for pixon image reconstruction to be successful. The 25-100keV energy range is selected to minimize the effects of high-temperature

thermal emission, which dominates X-ray emission below 25 keV for most flares, This energy range is effective for most events; however, some of the stronger X-class events do show significant thermal emission in the 25-50keV range. For those instances, we limit the imaging energy interval to 50-100 keV.

The results of the flare selection are tabulated in Table 3.1. We have 14 events covering a wide range of flare classifications. The GOES classification system is explained in Section 1.1.1. The UV images of these flares show a number of structural types (single loop, two ribbon, c-shaped, and multiple ribbon flares are all represented) all of which provide unique constraints on the magnetic topologies available in the flaring region.

RHESSI Flare Number	Date	Time Range (UT)	GOES X-Ray Class
2070405	4 July 2002	07:28-07:35	M 1.1
2070703	7 July 2002	03:57-04:05	C 3.5
2071611	16 July 2002	06:36-06:45	C 6.5
2071705	17 July 2002	06:56-07:05	M 8.5
2071811	18 July 2002	22:56-23:04	C 8.2
4011911	19 January 2004	12:30-12:38	M 1.1
4111002	10 November 2004	02:03-02:11	X 2.5
4122801	28 December 2004	00:07-00:13	C 7.2
5011502	15 January 2005	00:38-00:45	X 1.2
5011555	15 January 2005	22:41-23:19	X 2.6
5011912	19 January 2005	10:19-10:28	M 2.7
5012106	21 January 2005	10:12-10:21	M 1.7
6120608	06 December 2006	18:41-18:56	X 6.5
6120609	06 December 2006	20:15-20:23	M 3.5

Table 3.1 A summary of dates, times, flare classes, and catalog number for the flares analyzed in our UV/HXR relationship study.

3.2.2 The Flarewatch1600 observing program

The strict requirement of high cadence UV measurements and imaging for this study requires the use of a specialized TRACE observing sequence which forgoes the typical TRACE EUV observations in favor of continual UV 1600Å observations. The Flarewatch1600 program is specifically intended to observe flares at 1600 Å at high cadence to focus on chromospheric signatures. The program works in two stages. During the pre-flare observations of a potential flaring region, TRACE images a 384"x384" field of view at an approximate 4 second cadence. Approximately once per minute in this mode, TRACE takes a single white light frame of the same field of view for a context images. When the count rate passes a flare threshold, the TRACE field of view reduces to 256"x256" centered on the brightest pixel. Once in flare mode, TRACE images only at 1600Å and no longer includes the white light context unless flare mode remains in effect from more than half an hour.

3.2.3 RHESSI and TRACE Lightcurves

As a critical step in our temporal analysis, we construct lightcurves for both the hard X-ray and UV emission for each flare. Figure 3.4 shows the full-resolution HXR profile from 25-100 keV RHESSI data for 6 December 2006 X6.5 event. The profile shows transient hard X-ray burst signatures superimposed on the larger scale emission. Aschwanden et al. (1996) have shown that these smaller scale transients

are the result of a series of electron injections while the large scale features represent a trapped, then precipitated, particle population. The large scale bursts serve as

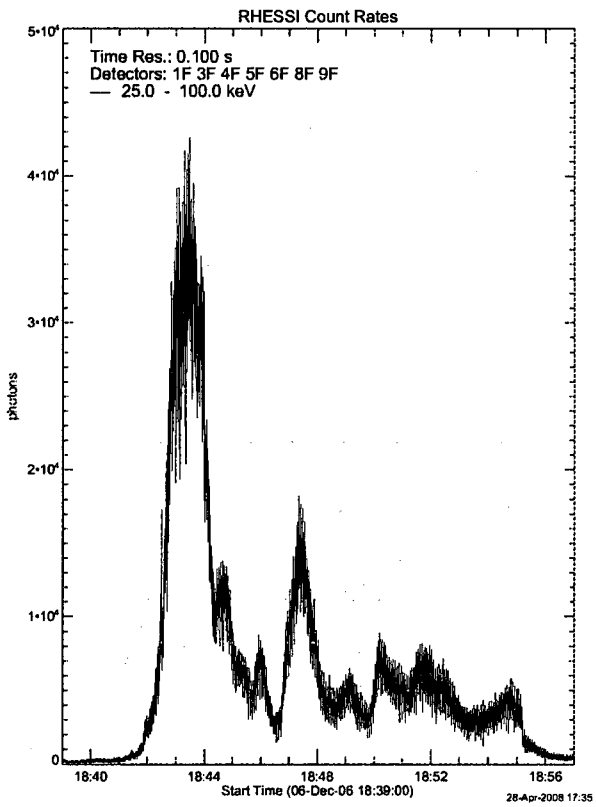

Figure 3.4 Example RHESSI hard X-ray lightcurve from RHESSI flare 6120608 shown at 0.1 second resolution.

the basis for our comparison between the UV and hard X-ray emission for both the complete spatially-integrated TRACE field of view and the signatures of individual sources. The spatially integrated emission treats the TRACE emission as if the field-of-view is not imaged, therefore, ignoring localized structures. The RHESSI emission

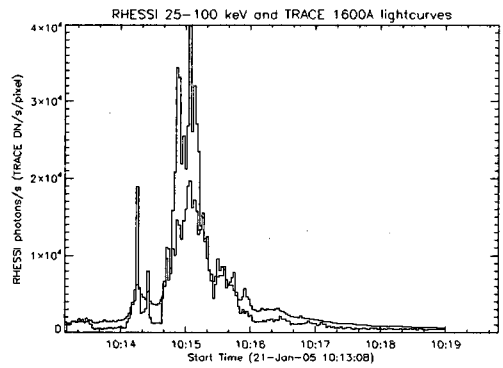

Figure 3.5 RHESSI and TRACE lightcurve comparison for 21 January 2005 M1.7 event. TRACE profile shown in blue.

used at high-cadence is spatially integrated for the full disk; however, localized sources of flare emission will dominate. We use the spatially-integrated data to match the cadence of TRACE as the imaged HXR data cannot achieve this cadence.

Comparison of the UV and hard X-ray time profiles requires the lightcurves to be of similar temporal cadence both for the full-field and individual source analysis. To achieve this, the hard X-ray data are binned to a 2-second cadence. In these curves the small-scale variance seen at full-resolution of the initial curves are to an great extent eliminated due to smoothing effects. However, the large scale bursts similar to those visible in the UV full field lightcurves remain clear (see Figure 3.5). For the correlation analysis with the UV, the 2s HXR data which correspond to TRACE image times are then used as a comparative dataset with the TRACE full-field observations.

UV Source Selection

The analysis of the individual source data begins with the source selection performed through the viewing of the TRACE observation sequence for the flare duration. We determine specific kernels which demonstrate clear enhancement during the time frame, using an image near the peak of both UV and HXR emission for the source selection. To select the sources in the study we have employed two distinct methods as our study has progressed. Initially, for our case study of a 16 July 2002 flare discussed in Alexander and Coyner (2006) and in Section 4.1.2, our sources are selected by visual inspection of spatially distinguishable kernels. The sources were enclosed in rectangular boxes based on user selected box corners. Figure 3.6 illustrates the selection of the six UV sources used in the C 6.5 flare event on 16 July 2002. Within the boxes, our algorithm totals the fluxes of those pixels above the image background levels. The flux values are then averaged to a flux per pixel value for each of the sources.

This method of source selection, while effective in determining the temporal characteristics of the UV source was improved upon for the latter results in our UV/HXR relationship study, discussed later in Section 4.2. The modifications made addressed two key issues in the initial source selection procedure:

1. Our box method of selection, while it encloses the emission enhancement, encompasses a larger area than the actual enhanced source.

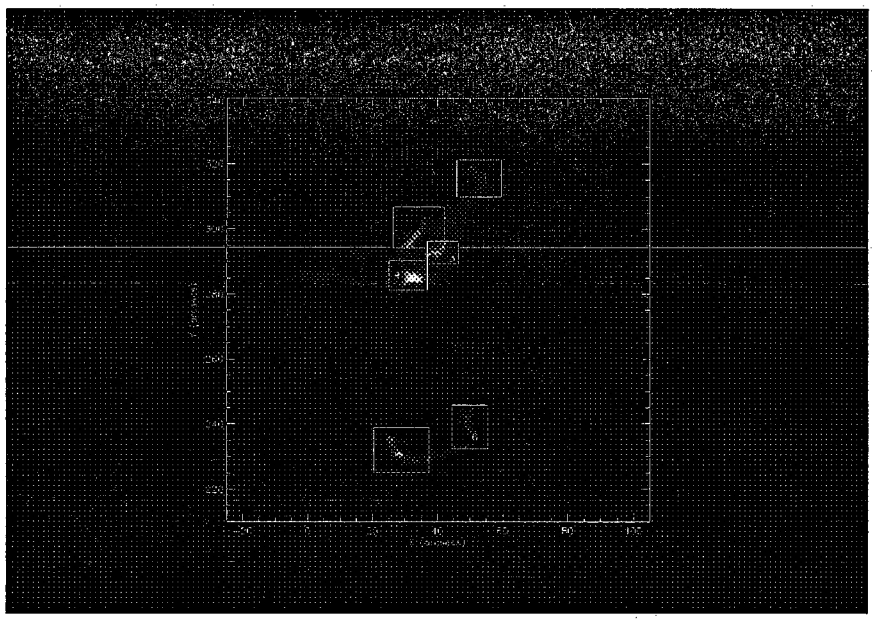

Figure 3.6 Example TRACE image from the 16 July 2002 event analysis of Alexander and Coyner (2006) used to illustrate initial source selection techniques used in the determination of the UV lightcurve for individual kernels observed in TRACE.

2. These rectangular selection regions, though selected to minimize overlap, did in fact do so in the 16 July 2002 event analysis, though there was not significant flux in the overlap region.

To improve the source selection method, the box method was replaced by a series of user-defined polygons using the IDL wdefroi.pro procedure within the lightcurve calculation. In each case, the polygons allowed us to refine the area so it more closely followed the borders of the enhanced emission kernel. Since the kernels are no longer restricted to a specific shape this also allows the prevention of source overlap which

will prevent contamination between source emission.

In both cases for this study, the calculated average flux per pixel of each source for each frame provides a clear representation of the temporal evolution of the UV response and provides a basis for correlation studies with the overall HXR emission. We are limited for high cadence studies to the overall, non-imaged hard X-ray emission due to the integration time limitations created by the HXR image reconstructions. The spatial locations of the emission enhancements provide key comparative data for the UV-HXR spatial relationship and potential visual constraints for the topology of the flare as chromospheric sources have been shown to lie along the boundaries of magnetic separatrix surfaces at their intersection with the chromosphere.

3.2.4 TRACE and SOHO/MDI Image Co-alignment

In order to facilitate spatial comparison of the UV and hard X-ray source locations, The TRACE pointing must be adjusted to account for the metering tube of the spacecraft undergoing minor flexes which are not accounted for in the raw positioning information provided by the satellite. The TRACE pointing has been shown to be in error by 5-12 arcseconds. Because there are no other observations in the UV continuum available, we must compare the TRACE white light context images and the MDI white light full-disk intensitygrams. Providing a set of comparable images with well defined pointing, the MDI images provide a means of co-aligning the TRACE images. The pairs of white light images show similar structures, (e.g. sunspot groups)

at different resolutions. Comparative images between the TRACE and MDI data are displayed in Figure 3.7. In both images there exist common sunspot structures and other features which are used as user-selected starting points for the co-alignment procedure.

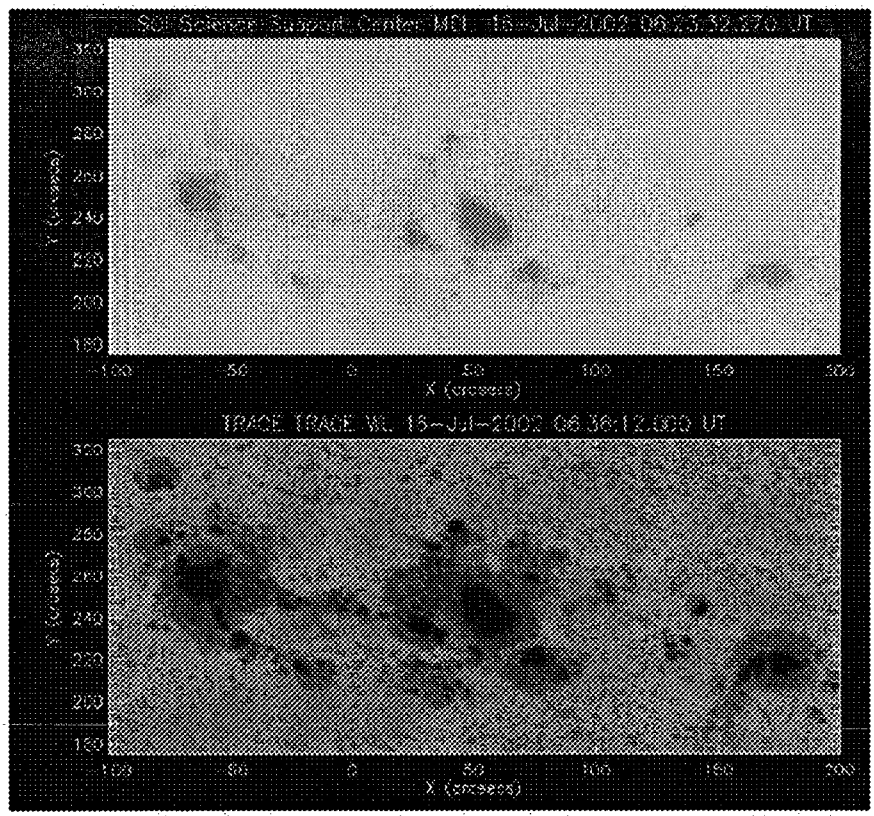

Figure 3.7 Comparative MDI white light image, showing specifically the sub-field of the TRACE field, and TRACE white light images for the 16 July 2002 event.

Co-alignment of TRACE and MDI images is performed through the IDL-based Solarsoft suite of software with the trace_mdi_align procedure. The procedure takes

the data for both datasets as indices, containing the fits header information for the observed data files, and the data cubes, which contained the images. The trace_mdi_align procedure asks for a region of interest in both the TRACE and MDI data. The user then selects features within the region that appear in both data sets. These selected points serve as an initial guess for the co-alignment procedure. For the co-alignment process, it is crucial that the images occur at nearby times to minimize effects such as solar rotation. For example, the timing separation of the images in the 16 July 2002 case shown is 15 minutes. The trace_mdi_align procedure takes the initial guess derived for the user-selected points and calculates the cross-correlation coefficient between the two data sets in the region of interest. From the initial correlation, the procedure uses an auto_align_images program to continually vary the position and stretching of the TRACE overlays until the correlation coefficient reaches a maximum value. A new image center is recorded based on this final shift.

The initial alignment of the images for the 16 July 2002 event shows a coordinate shift of approximately 4.7 arcseconds (4.5 in the y-direction and 1.0 in the x-direction) as depicted in Figure 3.8. The magnitude of the shift is within the range of the events in our study. The initial white light alignment is then passed through to the UV continuum images via the pointing corrections suggested by Metcalf (2003).

The corrected white light coordinates must be transferred to the UV image closest in time to the corrected white light reference image, typically 3-4 seconds later

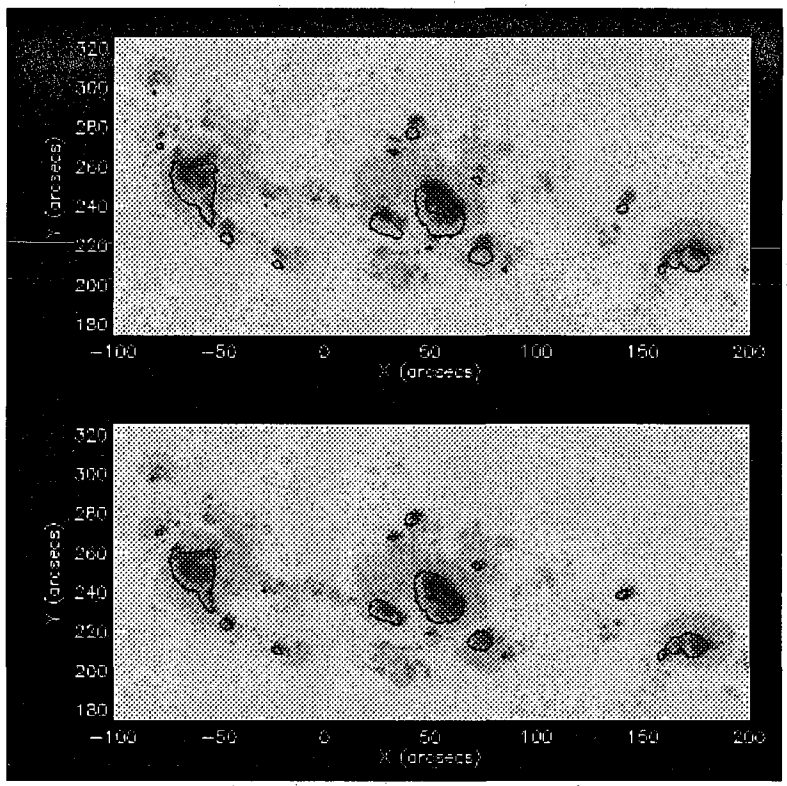

Figure 3.8 Before and after image maps for TRACE (pictured) and MDI (contours) for the white light image alignment of the 16 July 2002 event.

due to pre-flare Flarewatch1600 cadence. Once the corrected coordinates have been imported into a reference UV image, we use this reference image to align the remaining UV images through the use of the auto_align_images procedure for the complete set of 1600Å observations. The auto_align_images procedure employs the same cross-correlation analysis to execute the alignment for the 1600Å images as was applied in the white light case. The alignments are then verified through observation of the

TRACE movie sequence to verify that no discontinuous jumps occur. The variations in the central coordinates of the aligned UV images are displayed in Figure 3.9. The alignment results in an average of 3.6 arcseconds with the bulk of the shift being vertical.

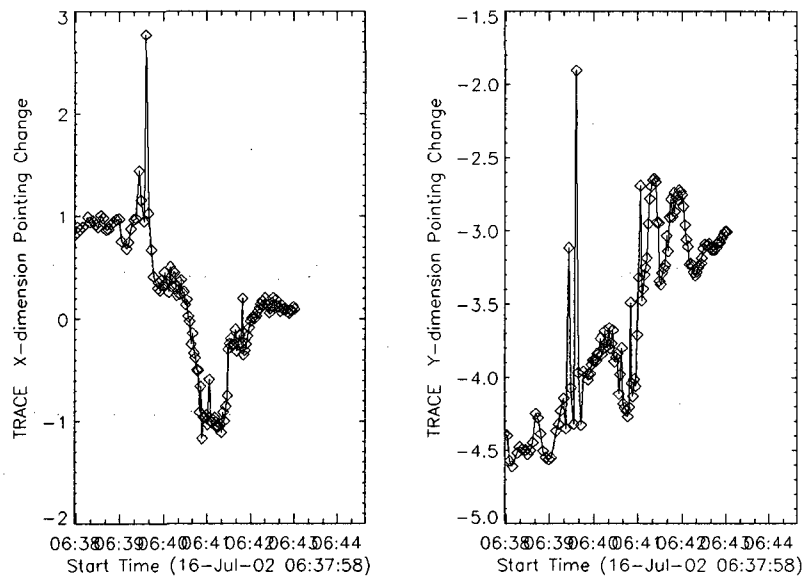

Figure 3.9 Plots of co-aligned XCEN and YCEN coordinate versus image time presented as a demonstration of the effectiveness of the co-alignment process

Quantifying the uncertainties in the co-alignment process, we plot the change in the XCEN and YCEN coordinates versus image time (see Figure 3.9) where XCEN and YCEN are the recorded central coordinates of the TRACE field of view. We calculate a standard deviation from our results for the coordinates assuming a normal

distribution. We determine an uncertainty in the co-alignment of $\pm$ 2 σ which for the 16 July 2002 case gives values of $\pm$ 1.14 arcseconds for the pre-flare 384"x384" images and $\pm$ 1.30 arcseconds for the 256"x256" images. These data must be addressed separately due to the systematic position shift resulting when TRACE goes into flare mode and centers on the brightest flare emission kernel. These results indicate that the co-alignment procedure used is accurate to approximately 1.3", or about 1000km; thus our co-alignment procedure is sufficiently capable of correcting the TRACE pointing such that notable separations between the UV and hard X-ray sources are likely the result of flare-related physics and not the alignment procedure.

3.3 SEP Study Methodology

Relating SEP characteristics measured in-situ at with the Advanced Composition Explorer (ACE) to the complex characteristics of the eruptive solar source region presents a number of unique challenges to incorporate the varied data sets, modelling, and numerical analysis. In this section each of these challenges will be addressed in detail beginning with the discussion of ACE data. We will also describe in detail our application of potential field source surface (PFSS) models to determine the available amounts of open field and thus access to the interplanetary space. Open field lines are defined by the models as field lines which extend to a radius beyond the solar corona. Particles along these lines stream out in a fashion similar to the solar wind though often at much higher speeds due to flare acceleration. A final component to

our study will be to quantify a measure of flare activity in the respective active regions associated with SEP events because remnant flare particles have been suggested as a small but significant component of the seed population for acceleration by the CME-driven shocks associated with the SEP events. We will then explore the importance of the variation in flare activity as it relates to the existence of enhancements in the heavy element composition above the traditional coronal values.

3.3.1 Elemental Flux Data from ACE

The elemental composition of SEP events was long believed to be a distinction between shock-accelerated gradual events and the small flare-associated impulsive events with the impulsive events showing enhanced abundances in Fe and other heavy elements along with ^{3}He. Recent ACE observations have shown that gradual events can often show these elemental enhancements as well based on the contributions of remnant flare particles to accelerated particle seed population (Mason et al., 2004). Further insight into the seed population for specific gradual SEP events requires comparison with the compositional measurements at ACE to determine if these enhancements are present.

The data used for this portion of our solar transient study is largely from two instruments aboard ACE: ULEIS (Desai et al., 2006) and SIS (Tylka et al, 2005, 2006; Cane et al, 2006). The compositional data used in our analysis is taken from the three studies cited above. All three studies choose SEP events which are determined to be

large SEP events based on the observed proton fluxes. For the events selected, time ranges are determined to limit the observed particles to those associated specifically with the SEP. For our study with ULEIS data we take the observations presented by Desai et al (2006) for heavy element ratios based upon the oxygen fluence measured for 0.32 0.45 MeV/nuc. Fluences for each element are totaled over the time frames selected for each event. Like the oxygen fluence, the other heavy element fluences cover the energy range 0.32 0.45 MeV/nuc. This allows for the direct comparison of of elemental composition without having to take into account energy variations. The total fluence for each element is measured and the ratios with oxygen that we use for compositional measurement are provided in Table 2 of Desai et al. (2006).

For the data from the respective Tylka and Cane studies (Tylka et al., 2005; Cane et al., 2006) the fluences, for iron in particular, are calculated, though each study uses a different energy range, the Tylka study focusing on 30-40 MeV/nuc while the Cane study extends the energy range to 25-80 MeV/nuc. In both of these cases the event fluences of iron are totaled over the time frames of each event which vary in duration but are designed to include only the SEP particles. These fluences are then normalized to the fluence measured for oxygen at these same energies. This ratio is then normalized again to the nominal coronal Fe/O ratio of 0.134 (Reames, 1995). This ratio of ratios is created such that event with enhanced Fe/O will show a ratio above 1. These events likely posses re-accelerated flare suprathermal particles whereas

those with ratios below 1 likely consist of typical coronal particles. The description of gradual events with seemingly flare associated enhancements is a subject of much theoretical debate within the energetic particle research community (Cohen, 2006; Cane et al. 2006; Tylka et al. 2005). For our work, these compositional measurements provide a link from the solar magnetic field configurations and flare activity measures to the nature of the particles accelerated from the Sun. Enhancements in heavy elements would indicate high energy flare particles but the mechanism for how these particles enter the accelerated particle population from solar activity remains ambiguous.

3.3.2 Solar Source Region Magnetic Field Characterization Via PFSS

A key process in our characterization of the solar precursor environment consists of the determination of the solar coronal magnetic fields both prior to and during the SEP associated eruption. Determining the connectivity within the solar coronal field is of key importance to the characterization of the solar source region environment. The magnetic field can be connected via both open and closed field. Open field regions are regions where the coronal field extends far beyond the local solar environment providing a direct connection to the heliosphere and interplanetary space for accelerated particles from solar eruptions. These regions are eventually closed somewhere in interplanetary space to maintain the divergence free condition ($\nabla \cdot B = 0$). Closed field is defined as the collection of magnetic field structures, often loop-like

in nature, which have both magnetic footpoints on the solar surface. The closed field regions are ideal configurations for magnetic traps that can potentially contain previously accelerated particles such as flare suprathermals.

Determining the magnetic field configuration in the solar orona is a significant challenge as coronal fields are not measurable; therefore, we must rely on extrapolations from the magnetic field line of sight observations at the photosphere. We then perform extrapolations from the photosphere using a PFSS model (Shrijver and DeRosa, 2003). PFSS models assume the coronal field to be potential, or current-free, such that:

$$\nabla \times B = 0 \tag{3.1}$$

in accordance with Maxwell's equations. The PFSS model uses a source surface defined at 2.5 solar radii as the boundary between the solar corona and interplanetary space (Luhmann et al., 1998; Hoeksema, 1995; Zhao and Hoeksema, 1996). This source surface is a mathematical construct to mimic the effects of the solar wind by creating a fully radial field at the boundary. Beyond this source surface the field will follow the standard Parker spiral through the heliosphere. The specifics of the PFSS model we used are discussed by Schrijver and DeRosa (2003). The initial inputs at the photosphere taken from the MDI synoptic maps derived from magnetogram observations and flux evolution models to create a full map of plausible magnetic data for the entire solar surface. Using these value as a starting point the

pfss_viewer Solarsoft routine the traces a user defined number of field lines in the process of extrapolating the field out to the source surface at 2.5 solar radii. These field lines traces help distinguish regions of closed and open field. Open flux regions are enclosed by field where the line traces are anchored to the photosphere only a one end and extend beyond the source surface at 2.5 solar radii. The open field regions distinguished in pink and green visually as shown in Figure 3.10 taken from Liu et al. (2004). Close field loops, on the other hand, form in many locations around the active region where closed magnetic structures such as loop arcades are prevalent. These loops serve as potential traps for energetic particles though most of the loops are contained in the low corona.

For our study, we focus on PFSS extrapolations for the specific active region responsible for the source eruption rather than on the global field. These extrapolations assume a potential, or current-free, coronal field building from the photospheric measurements of the active region field from MDI up to a height of 2.5 solar radii. We perform extrapolations of 400 field lines in the active region of interest. An example of this localized extrapolation is shown in 3.11. This image from 18 April 2002 shows a significant region of open magnetic field within the active region which provides direct access from the acceleration of particles into the heliosphere. Within the data collected in the model calculations, there are four separate maps of magnetic field distribution information. One shows the locations of the open field region, distinguishing

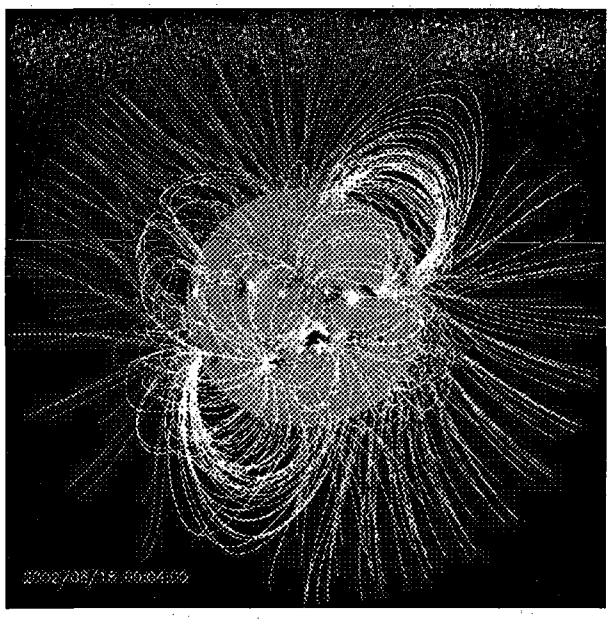

Figure 3.10 Global PFSS extrapolation from 18 April 2002 showing the developing field configuration prior to a large SEP event of 21 April 2002. Figure taken from Liu et al., 2004. Pink and green field lines are representative of open field regions of opposite polarity.

open field lines locations by non-zero pixel flags. The other three sets of data are the radial, theta, and phi components of the extrapolated field at heights in the corona up to the source surface boundary. Using the map of open field boundaries, we are able to calculate the magnetic flux passing through the open field region providing a quantitative measure of the open field component of the coronal field

3.3.3 Flare Productivity

In addition to the magnetic configuration, one key distinction among the solar source active regions associated with SEPs is the flare and CME productivity of the

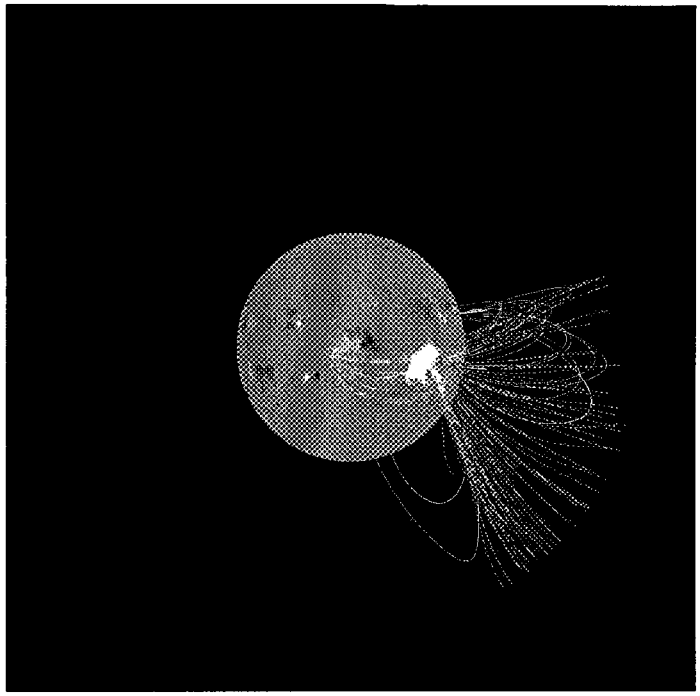

Figure 3.11 Example of localized active region PFSS extrapolation for an 18 April 2002 image. The large region of open field shown in pink provides significant access for accelerating particles into interplanetary space.

solar source active region. Flare productivity provides a second method of classify the solar source characteristics in addition to magnetic connectivity and complexity because the active regions with the greatest magnetic complexity generally are the most flare productive. Flare suprathermals are a critical component of the SEP seed population, contributing significantly to the observed composition enhancements; therefore, flare productivity of an active region may have direct implications on the available particles in the subsequent SEP events.

To quantify this we modify a measure of flare productivity known as the flare index shown in Equation 3.2 (Abramenko, 2005).

$$A = (100S^X + 10S^M + 1.0S^C + 0.1S^B)/\tau \tag{3.2}$$

In the flare index equation we take into account the logarithm scale of the flare classification system. The respective S-values are the nominal totals for the sum of flares in a given flare class where a C 3.0 adds 3 to the S^C total. The lifetime, τ, was initially the number of days the active region was on the disk. However, since future events would not be included in a potential event seed population, we limit τ to the time frame from the active region's first appearance until the event onset. The calculation yields that the most productive active regions would have the highest flare indices. In our analysis we use two versions of the modified calculation. The first takes into account the flare productivity of only the active region in question from first appearance to time of event. The second version takes into account possible flare particles from neighboring regions by including all the observed flares over the time range in question.

To this point, we have focused on the background and methodology used in our study. The chapters that follow will progress through the data analysis and results for the various components of the study: UV/HXR results in Chapter 4, discussion of our magnetic topology study incorporating the analysis of separators and hard X-ray distributions in Chapter 5, SEP study results are included in Chapter 6.

Chapter 4
Relationships between Hard X-ray and Ultraviolet Emission in Solar Flares

Solar flares, while intriguing on the surface due to their bright expansive explosions and the tremendous energy they release over such short time scales, are of tremendous interest scientifically due to the complexity of the flare response over the full range of the electromagnetic spectrum and the wide array of physical processes involved in the generation of flare emission. The exact nature of the physical processes involved and to what degree they combine and interact are not clearly understood. These aspects are all critical to a full understanding of the physical nature of the flaring process. Observations across multiple wavelengths provide a diagnostic mechanism for the particles and processes involved by permitting the comparison and interpretation of disparate emission signatures. Such observations also facilitate a direct link to both the flare trigger and the general physical development of the flare in its entirety: both crucial physical considerations necessary for a complete understanding of solar flares and their effects on the Sun and the heliosphere.

One key observational relationship which can be directly related to the energy trigger and the associated particle acceleration processes is the temporal and spatial comparison of ultraviolet and hard X-ray emission. To this end, the study presented here addresses the UV/hard X-ray relationship utilizing high spatial and temporal

resolution data from the TRACE (UV) and RHESSI (hard X-ray) satellites. Initially, we analyze the temporal and spatial development of 8 events from 2002-2004 observed over the full duration of the flare at hard X-ray energies, using RHESSI (see Section 3.1.2) and high-cadence (approximately 2 seconds), high spatial resolution ($\sim$ 1 arc-second) UV data, using the TRACE satellite (see Section 3.1.1). The events of the initial study cover a range of importance class from C3.5 X2.5 in GOES soft X-ray intensity (see Section 1.1.1). We begin by presenting a case study of a C 6.5 flare event from 16 July 2002. This flare is a smaller magnitude more spatially-confined two-ribbon flare in comparison to others in our study; however, its temporal and spatial development still possesses more complexity than would be typically expected for a weaker flare, providing important insight into the UV/HXR relationship, and the significant role of the magnetic environment in which the flare occurs.

We analyze the UV development of the flare both as an unresolved event to compare with previous studies which lacked spatially-resolved hard X-ray data, and on the scale of localized UV source evolution utilizing the full resolution of the TRACE telescope. The UV data in both cases are directly compared to the temporal evolution of the spatially-integrated hard X-ray (25-100 keV) emission seen from RHESSI. This comparison for correlated UV and hard X-ray emission is critical, as discussed by Cheng et al. (1998) and in Section 2.1.1, because it provides and observational means of tracing both the UV and the hard X-ray emission to the same flare energy

release. The improved imaging capability of RHESSI is the means for determining the spatial distribution of the flare hard X-ray emission and its evolution over time. As was discussed in Chapter 3, X-ray imaging greatly limits the temporal resolution of the spatially distributed hard X-ray emission as the integration time required to create an X-ray image is typically several times the cadence of the TRACE UV data. In the spatial analysis, we compare the locations and evolution of the sources of localized emission in both wavelengths to determine the spatial structure of the flare and what the observed distribution of UV and HXR intensity enhancements tell us about the physical processes leading to the observed distributions. Each of the emission kernels provides direct information on the likely sites of the strongest energy dissipation and particle acceleration. When combined with the temporal results, the spatially-resolved observations provide substantial insight into the flare initiation, development, and the magnetic environment in which it occurs. Comparisons of simultaneous spatially-resolved emission permit the determination of any spatial separation between temporally correlated UV and HXR sources. In combination with the temporal correlations, the spatial separations of correlated UV and HXR emission provide observational limits on the emission mechanisms and help to clarify the magnetic structure of the flaring region. The observed separations indicate the need for a more complex magnetic topology for flares than is depicted in the models such as the CSHKP model (Figure 1.6) or the Kane-Donnelly-Frost model, first discussed in

Section 2.1.1 . Additional soft X-ray imaging from RHESSI and magnetogram data from SOHO/MDI permit the further topological investigation of the overall X-ray structure and coronal magnetic field structures that may be potentially responsible for the observed flare emissions.

Moreover, as the flares evolve, the emission enhancements appear in different locations implying variations in the connectivities. The next section details the results of our analysis for the 16 July 2002 flare, also discussed in Alexander and Coyner (2006). This flare provides a detailed case study of the variation in the temporal and spatial relationship between the UV and HXR emission throughout the flare evolution and also serves as a basis for comparison with more intense and complex events, studied later in this chapter.

4.1 The 16 July 2002 Event Overview

The 16 July 2002 C 6.5 flare peaks in the soft X-rays at 06:42 UT. The GOES soft X-ray profile of the event illustrates the overall temporal behavior of the flare, tracing the thermal emission of the hottest flare plasma (see bottom of Figure 4.1). While the soft X-ray profile allows us to quickly compare the general characteristics of different flares, only the hard X-ray timing is critical for our study. The RHESSI profile for the 25-100 keV energy range (shown in Figure 4.1 at both full and binned resolutions (Top)) shows a single large scale burst of approximately 4 minutes duration. The single burst contains a number of smaller scale events on the time scales of tenths

of seconds. These small scale events group together as a series of secondary bursts when the data is smoothed to match the 2s cadence of the UV data. The hard X-ray emission shows a steep rise signifying the impulsive phase of the event reaching its peak at ~06:40:25 UT, approximately one minute after the hard X-ray initiation. This peak is followed by a consistent decay until 06:43:00 UT. Within this overall behavior we see a smaller burst structure with two primary bursts evident: one from 06:39:30 06:40:10, with a peak at 06:40:00 UT, and the subsequent burst beginning at 06:40:10 until 06:40:40. Each of these bursts exhibits further sub-structure down to the 0.1 second resolution shown, consistent with the repeat and bursty injection of particles discussed by Aschwanden (1998).

The overall UV time profile, obtained from the spatial integration over the full TRACE field of view, depicts a multi-burst structure showing a strong similarity to the HXR evolution as expected from previous works (e.g. Cheng et al, 1988; also see Figure 4.2 for the UV profile.). Much like its HXR counterpart, two bursts are evident in the UV profile over the time range 06:39:30 06:41:00. Two considerably smaller bursts are also evident during the following sixty seconds, after the hard X-ray emission has essentially fallen off. The two bursts that occur during the impulsive phase show similar characteristics to those seen in the hard X-ray emission. We will quantify these observations through cross-correlation analysis for both the full field of view, the individual ribbons, and selected individual sources in Section 4.1.1.

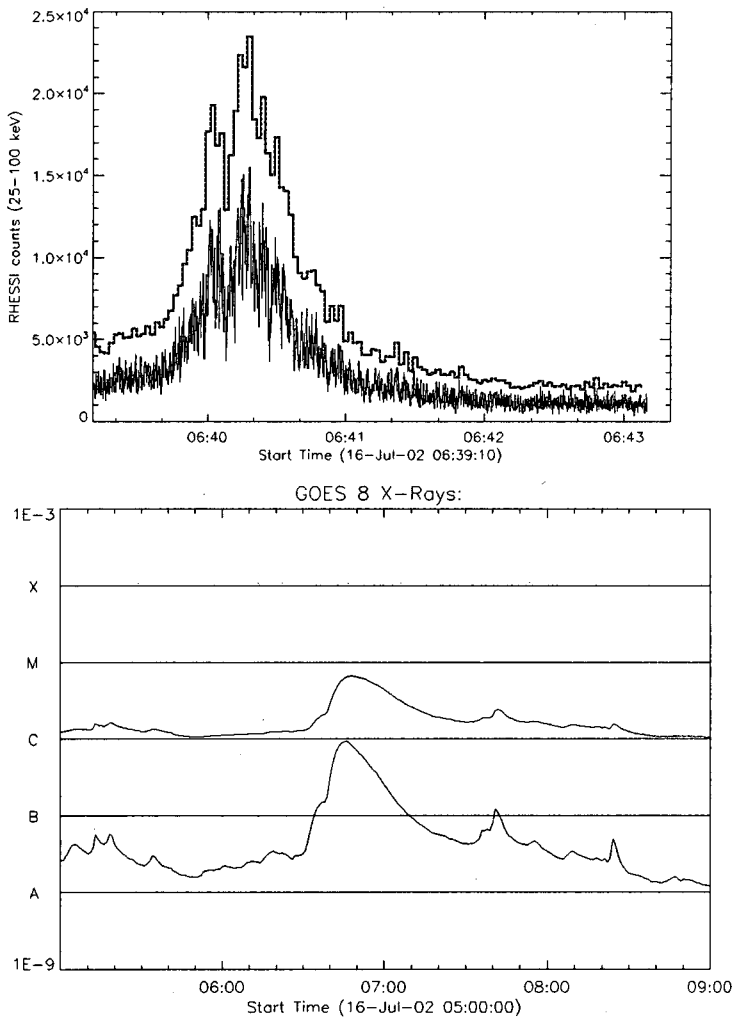

Figure 4.1 Top: RHESSI hard X-ray lightcurve for the energy range of 25–100 keV from flare 2071611 shown at 0.1 second and 2s (binned) resolution for the time range 06:39:10–06:43:10. Bottom: GOES soft X-ray plot used for flare classification and general X-ray context of the event

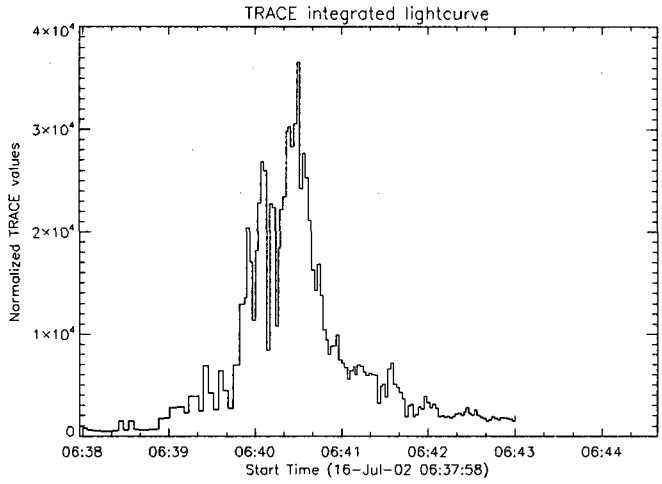

Figure 4.2 Lightcurve showing the temporal evolution of the TRACE 1600Å data: the emission has been integrated over the whole field of view. A number of clear burst structures are visible.

Spatially, the 16 July 2002 event shows a flaring region exhibiting a standard two ribbon morphology with the two ribbons being separated by about 70,000 km, on average. Over the course of the flare, these ribbons develop sporadic, isolated UV enhancements. The top ribbon shows emission enhancements contained in four main segments along that ribbon over an area of 85"x45". Throughout the temporal evolution of the flare, these emission enhancements vary widely in location and appearance. In direct contrast, the lower ribbon is much more compact and remains consistent in spatial extent for the duration of the flare; however, there are significant variations in intensity from the two end segments of this ribbon as the flare evolves. The western endpoint shows notable brightening prior to and following the hard X-ray

activity with little appreciable activity seen during the hard X-ray impulsive phase. The majority of the UV activity in the lower ribbon during the hard X-ray emission is concentrated near the left (eastern) endpoint. A sequence of TRACE UV images illustrating the evolution of the UV ribbons is displayed in Figure 4.3. The image sequence clearly indicates significant evolution of the UV emission in the top ribbon as the flare progresses while the the lower ribbon remains nearly identical in spatial extent throughout the duration of the flare.

In contrast to the extended and widely varying evolution of the UV signatures for this event, the hard X-ray counterparts, in the 25-100 keV energy range, are much more strongly confined. The strongest of the HXR sources appear fixed throughout the duration of the flares into a 20"x10" subregion of the solar surface, centered on the eastern end of the lower UV ribbon. This X-ray complex shows a single source for the most part during the evolution, though at various times the intense complex separates into two tightly confined footpoints providing the anchor points for a well-defined hard X-ray loop. Meanwhile, a region near the expansive upper UV ribbon shows a very weak but detectable hard X-ray emission source (see Figure 4.4). This source is not co-spatial with the ultraviolet enhancements and will be addressed later in this chapter.

The RHESSI images in this study are constructed using 10-20 second reconstruction times to allow for significant enough photon counts for the image reconstruction

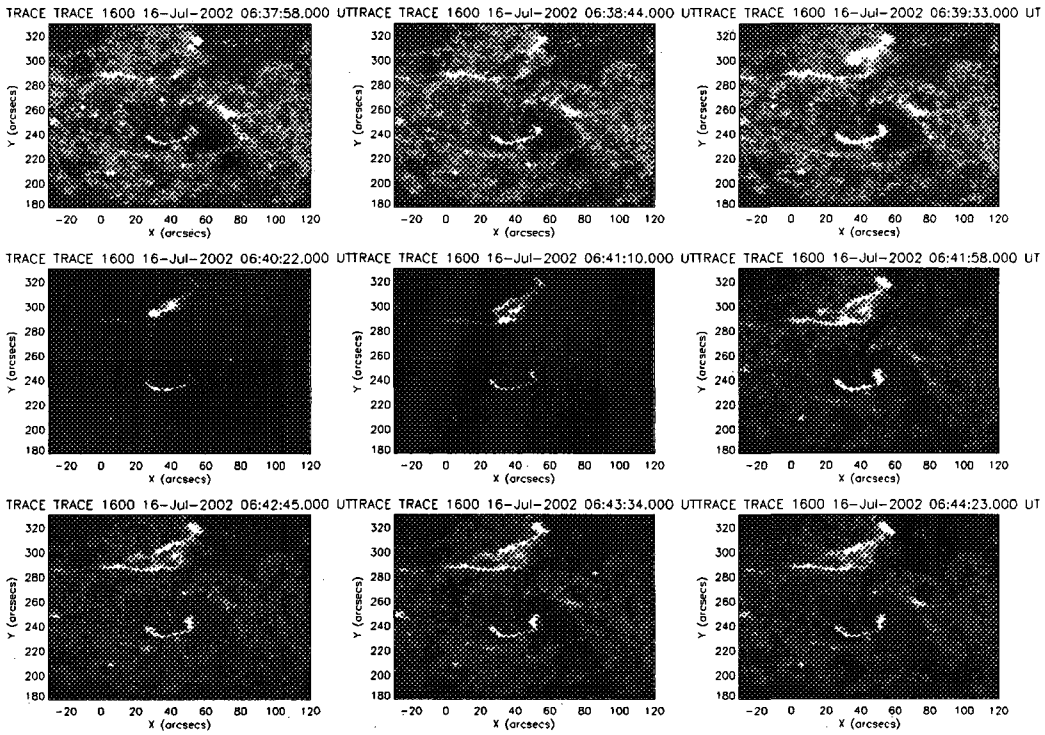

Figure 4.3 TRACE UV image sequence illustrating the evolution of the UV ribbons over time. Note that the lower ribbon is very well defined throughout while the upper ribbon shows significant variation.

algorithm to converge. A sample image of the flaring region showing the spatial development in both wavelengths near the flare peak is shown in Figure 4.4 with the image itself being generated from a 20-second reconstruction using the PIXON algorithm (see Section 3.1.2) and the overlaid contours detailing where the UV enhancements are in relation to the reconstructed X-ray sources.

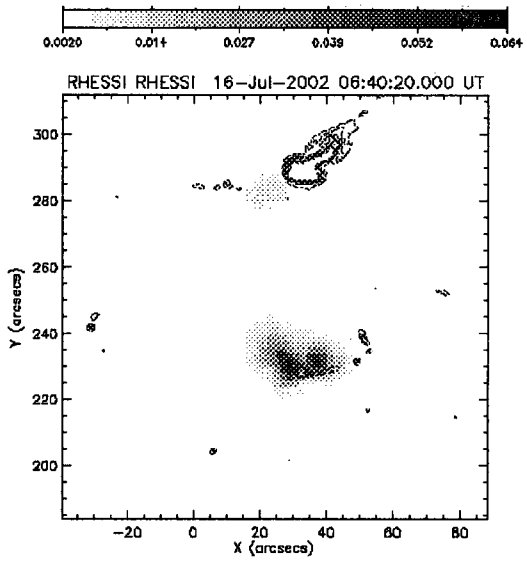

Figure 4.4 RHESSI Pixon image covering the 25–100 keV energy range with 20s time resolution for the time frame 06:40:20–06:40:40. RHESSI values (photons cm^{-2} s^{-1} $arcsec^{-2}$) and gray scale key are shown above the figure. The contours show the TRACE UV ribbon locations.

4.1.1 Temporal Analysis of the 2002 July 16 Case Study

With the general behavior of the event in both wavelengths described above, we address now the specific details of the results from the temporal analysis of the flare for both the full field of view and the individual localized source cases. The generally impulsive and bursty nature of both the UV and HXR emission are qualitatively suggestive of a temporal relationship similar to that reported by Cheng et al. (1988). To quantify these results we perform a linear cross-correlation analysis to determine the nature of the temporal and spatial relationships between the UV and HXR emission

when treating the flare as a single spatially-integrated source and the more complex spatial and temporal relationships when treating the flares as comprised of localized UV emission kernels.

Full-Field Temporal Analysis

To quantify this relationship we perform a correlation analysis and calculate the linear correlation coefficient for the whole HXR burst time frame and independently for the two large-scale HXR sub-bursts discussed above. The results of these calculations are provided in Table 4.1. Within this analysis, we have removed a data point

Time range (UT)	*Number of Points*	*Correlation Coefficient(r_1)*	*Confidence Level*	*Confidence Interval*
06:39:00–06:41:30	66	0.817	0.99	0.677–0.900
Individual Burst Correlations				
06:39:30–06:40:10	17	0.848	0.99	0.508–0.959
06:40:10–06:40:40	16	-0.128	0.90	-0.514–0.301

Table 4.1 Full-field correlation and statistical confidence results for the analysis of the 16 July 2002 event.

corresponding to a RHESSI instrumental attenuator change near 06:39:10. This is standard procedure as this data point produced an anomalous single point spike in the X-ray data. and was removed specifically to ensure that instrumental effects cannot skew the correlation results. The datasets show a strong overall correlation with a linear coefficient over the time frame 06:39:00 06:41:30 of r=0.817 for the burst activity as a whole. The linear correlation used is consistent with previous results (Cheng et al., 1988) and is further substantiated by the scatter plot comparison of the

full field data (Figure 4.5). While the data show a linear trend consistent with the measured correlation coefficient, a significant amount of scatter is present. To clarify this, we identify the points with greater than 2σ residuals from the best linear fit as filled triangles. While these large residual points influence the best fit and correlation results, their effects cannot be excluded as they arise naturally within the data as opposed to the instrumental effects such as the attenuator change.

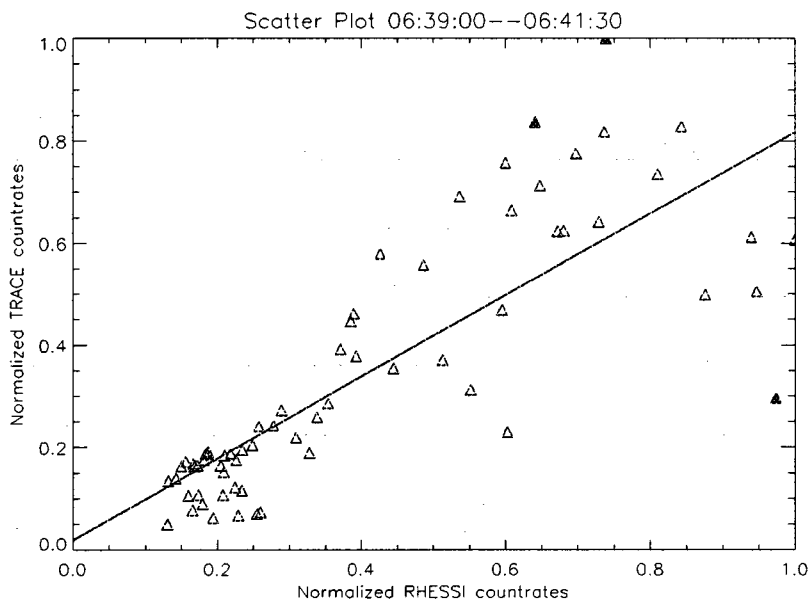

Figure 4.5 Scatter plot of TRACE normalized countrates vs. RHESSI normalized countrates illustrating the linear correlation determined for the full field of view data. Filled triangle symbols indicate 2σ scatter from the best fit line.

The time frame selected covers only the large bursts to minimize the effects of the low activity wings. This time frame contains 66 UV/HXR flux pairs rendering

the measured correlation significant to the 99% level, as determined using critical values for the correlation coefficient (Rohlf and Sokal, 1995). For each correlation measurement, we determine a confidence interval providing a range of coefficient values within which the true correlation must lie for a given significance level. Both the confidence levels and the corresponding intervals are given in Table 4.1.

Source Selection and Individual Source Analysis

Although the overall flare behavior in both the UV and HXR shows a significant temporal correlation, the UV emission demonstrates significant variability in temporal evolution within the two visible ribbons. Both ribbons are clearly defined throughout the flaring time frame, but the upper ribbon is much larger in spatial extent with its evolution appearing more as a loose collection of enhanced kernels rather than a single, continuous ribbon. In terms of overall activity, the UV ribbons also show distinct differences in their temporal behavior. The upper ribbon displays decidedly more activity relative to its lower UV ribbon counterpart: the lower ribbon, at its brightest point, is only 53% of the maximum UV source emission. The upper ribbon is the more readily associated with the bulk of the hard X-ray activity. The relative strengths and spatial locations of the ribbons suggests a clear departure from traditional single-loop flare models as the dominant UV ribbon is not directly associated with appreciable co-spatial emission. The temporal correlation results for each ribbon confirms the dominant association of the upper ribbon with the hard X-ray emission though the

correlation seen in these ribbons is weaker than in the full-field case. Correlations for the upper and lower UV ribbons separately were 0.780 and 0.576 respectively (see Table 4.2). The stronger correlation with the HXR emission and the upper ribbon deviates from the co-spatial and co-temporal emission expected for these wavelengths in the standard flare picture, as the HXR emission is spatially concentrated on the other ribbon. This implies that while the bulk of the UV emission observed can be directly correlated in time with the hard X-rays and therefore, traced to the same energy release, a more complex UV/HXR relationship is required to explain the emission as the individual sources evolve within the ribbon.

UV Source	*Time Range*	*Correlation (r_1)*	*Conf. Level*	*Conf. Interval*	*Comments*
Upper ribbon					
Complete Ribbon	06:39:00–06:41:30	0.780	0.99	0.617–0.879	duration of HXR
	06:39:30–06:40:10	0.775	0.99	0.330–0.938	1^{st} HXR burst
Individual Sources					
Source 1	06:38:40–06:39:40	0.892	0.99	0.614–0.973	pre-HXR
	06:41:30–06:42:30	0.191	0.90	-0.257–0.571	post-HXR
Source 2	06:39:00–06:41:30	0.630	0.99	0.394–0.788	duration of UV Source 2
	06:39:50–06:40:10	0.702	0.95	0.215–0.909	1^{st} HXR burst
	06:40:10–06:40:30	0.461	0.90	-0.082–0.793	HXR flare peak
Source 3	06:40:00–06:42:00	0.532	0.99	0.254–0.729	duration of UV Source 3
	06:39:30–06:40:10	0.610	0.99	0.019–0.885	1^{st} HXR Burst
	06:40:10–06:40:30	0.722	0.95	0.215–0.922	HXR flare peak
Source 4	06:40:20–06:42:00	0.923	0.99	0.846–0.962	duration of UV Source 4
	06:40:20–06:40:50	0.912	0.99	0.677-0.978	2^{nd} HXR burst
Lower ribbon					
Complete Ribbon	06:39:00–06:41:30	0.576	0.99	0.320–0.754	duration of HXR
	06:39:30–06:40:10	0.397	0.90	-0.020–0.696	1^{st} HXR burst
	06:40:10–06:40:40	0.570	0.95	0.104-0.831	2^{nd} HXR burst
Individual Sources					
Source 5	06:39:00–06:41:30	0.581	0.99	0.327–0.757	duration of UV Source 5
	06:39:40–06:40:10	0.251	0.90	-0.235–0.636	pre-HXR
	06:40:10–06:40:40	0.452	0.90	0.047–0.792	HXR flare peak
Source 6	06:38:40–06:39:40	0.864	0.99	0.532–0.965	pre-HXR
	06:41:30–06:42:30	-0.377	0.95	-0.641 – -0.033	post-HXR

Table 4.2 Complete ribbon and individual source correlation and statistical confidence results

Because of the apparent fragmentation of the upper ribbon and the fluctuations of the endpoints of the southern ribbon, we choose to investigate the behavior and evolution of the individual enhanced kernels within both UV ribbons and determine their relationship to the notable X-ray bursts. For the X-ray comparison, we must use the spatially unresolved X-ray emission. We cannot compare temporal evolution in individual X-ray sources with the individual UV sources because the integration times required for the image reconstructions eliminate the ability to perform high-cadence analysis.

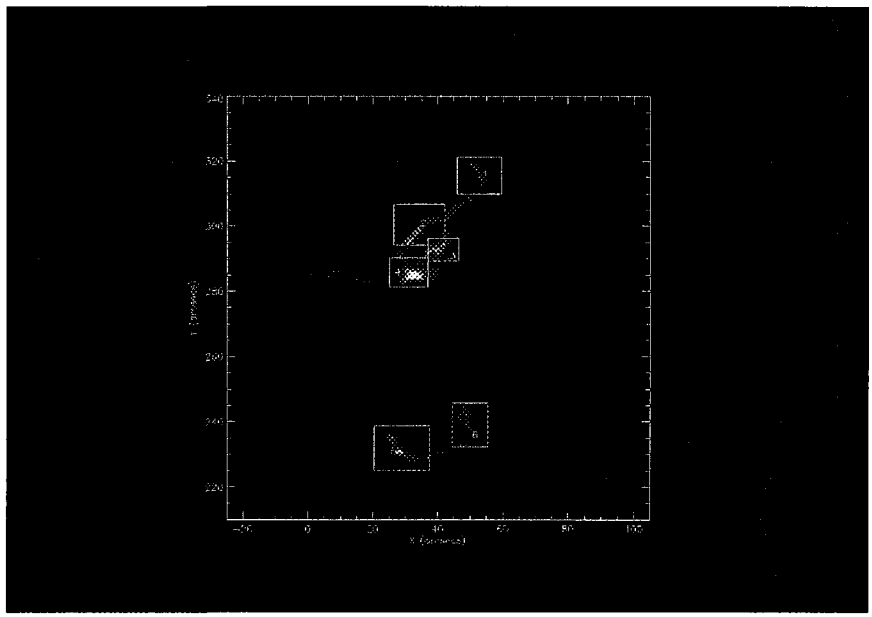

Figure 4.6 Reproduction of Figure 3.6 for quick reference to the source identifications and spatial locations used in our analysis of the 16 July 2002 event.

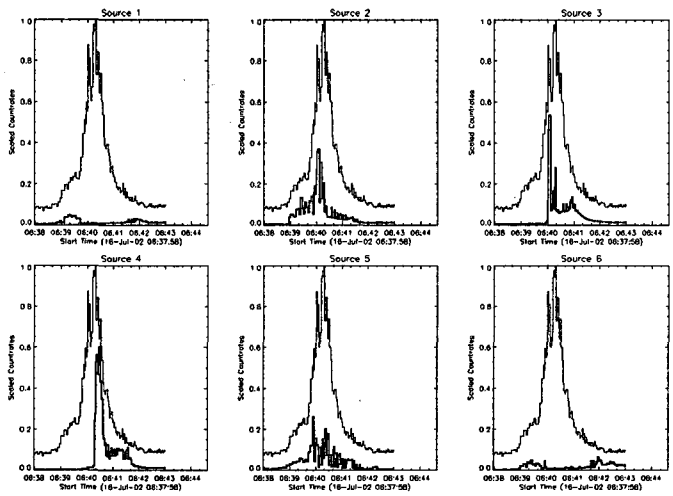

Figure 4.7 UV emission profiles for the 6 sources discussed each scaled to 0.6 of normalized count rates (thick curves) and plotted against the normalized HXR profile (thin curve). All UV profiles shown are scaled to a common maximum.

Figure 4.6, illustrates the selected enhanced UV kernels used in this portion of the analysis. We separate the northern ribbon into four main kernels each of which displays enhanced emission over the course of the ribbon evolution. Initially, these sources brighten in a progression from the the northern and western end (Box 1) to the southern and eastern end (Box 4). While the boxes for sources 2 and 3 do noticeably overlap, visual inspection of the TRACE images confirms that the two areas enclose predominantly separate brightenings. For each of the UV sources identified we calculate the integrated UV emission and perform a correlation analysis over the respective times when the sources are active. Lightcurves for the individual kernels are shown in Figure 4.7.

The individual UV kernels exhibit a number of interesting developments. Source 1, in the northwest corner of the ribbon, brightens during two distinct periods. The initial brightening occurs early in the impulsive rise of the HXR emission; however, this initial brightening dims prior to the onset of the first strong HXR burst. Source 1 does not contribute during the bulk of the hard X-ray emission, rising again at $\sim$ 06:41:20 after both significant HXR bursts have effectively ended. As a consequence, Source 1 is largely uncorrelated with the HXR data despite being a significant source of UV emission. In contrast, Sources 2 and 3 show their most significant contributions during the initial burst of HXR emission. The brightest of these sources, Source 2, is the first to activate. As Source 2 reaches its peak, emission begins in earnest in region 3. Following the initial burst of HXRs, emission from these two UV sources diminishes with no appreciable impulse during the second burst. The UV source which appears most prevalently during the second burst of hard X-rays is Source 4 in the southern portion of the upper UV ribbon. Source 4 is the strongest UV emission recorded overall.

The southern UV ribbon is dominated by emission in the two endpoints. The western endpoint (Source 6) shows similar behavior to that of Source 1 as it contributes the majority of its emission both prior to and following the hard X-ray emission. The lower ribbon's association with the HXR emission appears to be confined to the co-spatiality of Source 5 at the eastern end of the lower ribbon to the dominant hard

X-ray source. The time profile of Source 5 shows similarities to the X-ray behavior although the UV peak occurs prior to the two major hard X-ray bursts. For the correlation analysis of the individual sources we consider the time frames in which each source is clearly active in relation to the HXR emission. The times used can be inferred from the profiles shown in Figure 4.7. All correlation results for the individual sources with respect to both the overall time frame and individual burst behavior are included in Table 4.2.

Source 1 produces, at its peak, only ~20% of the maximum UV emission with emission occuring from 06:38:40 06:39:40 and then reoccurring from 06:41:30 06:42:30. The comparison of the emission from Source 1 with precursor HXR emission shows a strong correlation mostly due to low levels of activity. However, the post-burst period is consistent with no correlation. Source 2 shows emission over the period 06:39:00 06:41:30 with the most intense emission occurring between 06:39:50 06:40:30 spanning the bulk of the HXR bursts. We focus on the bursts detectable in the X-ray profiles, there are multiple active UV sources during each of the X-ray bursts. Source 2, and to a lesser extent Source 3, show a correlation with the initial burst while the second burst shows correlation with Sources 3 and 4.

Emission in the lower ribbon during the hard X-ray bursts shows a moderate correlation for the duration of the HXR activity which, although weaker than its upper ribbon counterpart, is still significant to a 99% level. This ribbon's emission

is largely governed by Source 5 at the eastern end of the ribbon. Source 5 shows a 99% significance level correlation for the duration of the impulsive phase of the flare from 06:39:00 06:41:30, though correlations with the smaller bursts with this range are not as well defined.

While these timing results are significant in their own right, for their connection to energy release timing (see Section 4.1.3), they gain further importance when taken in combination with the spatial distribution results. Our next section will further elucidate the important spatial results and the complexities necessary to produce them within the 16 July 2002 event.

4.1.2 Spatial Analysis

In the previous section, we determined that the temporal evolution of the UV and hard X-ray emission were strongly correlated both for the spatially-unresolved full field comparison and for the evolution of the ribbons and individual kernels. The correlated emission implies that the UV and hard X-ray emission signatures are governed by the same energy input mechanism, believed to be magnetic reconnection in the solar corona. However, this temporal association is only one important aspect in the overall understanding of flare behavior. It is also imperative to determine the spatial associations of these temporally correlated emissions if we are to gain insight into the structure of the solar magnetic field leading to solar flares, and gain a clearer knowledge of the energy distribution throughout the solar atmosphere. Using

images from TRACE and image reconstructions from RHESSI, we have been able to spatially localize emission sources for both the UV and hard X-ray wavelengths over the majority of the flare duration. We concentrate on the spatial distribution of emission during periods of greatest activity.

Using the high cadence of the UV observations provided by the flarewatch program (See Section 3.2.2), we track the evolution of the UV emission throughout the periods of significant HXR activity. Figure 4.8 presents six UV image maps representing the flare development over the course of both impulsive bursts discussed in our temporal analysis with the contours of the 25 100 keV hard X-ray emission overlaid covering this time period. Each image depicts the hard X-ray contours resulting from 10-second integration image reconstruction overlaid atop the TRACE 1600Å images from the center of the integration interval. The observations show the strongest hard X-ray source for this period as a confined source, distinguishable as two separate footpoints during the initial X-ray peak, with its centroid near [30", 231"] from disk center. This spatial location is nearly co-spatial with UV Source 5 on the lower UV ribbon. In contrast, there appears to be no well-defined hard X-ray source with counts above 10% of the hard X-ray maximum emission corresponding to the upper ribbon. Despite this, we cannot rule out low-levels of hard X-rays in this upper ribbon, but the lack of emission above the 10 % level indicates that any hard X-ray source within the upper ribbon must be much weaker than the source associated with the UV emission in

the lower ribbon. From our temporal ribbon analysis, we find that the upper ribbon correlated well temporally with the hard X-ray emission yet the hard X-rays appear to be spatially associated with the lower ribbon.

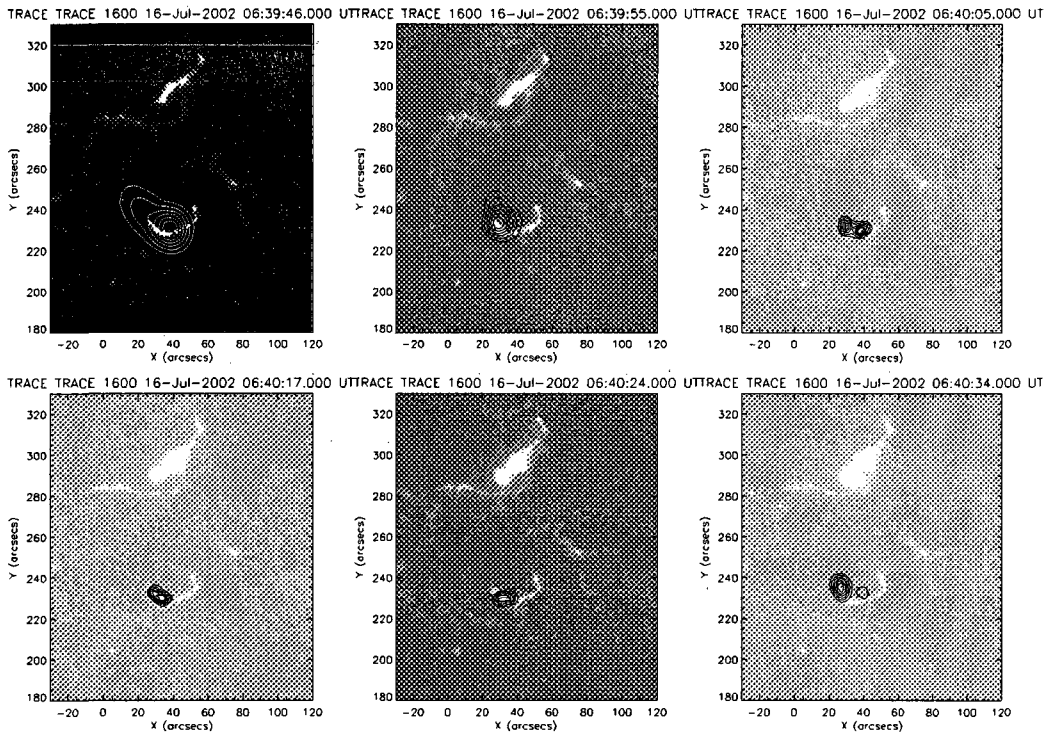

Figure 4.8 Series of TRACE 1600 Å images with contours from the corresponding 25–100 keV RHESSI images integrated from 06:39:40-06:40:40. The time range covers both major HXR bursts discussed. The contours shown represent X-ray emission levels of greater than 40 percent of the maximum recorded for each RHESSI image.

The observations in Figure 4.8 illustrate aspects of the UV evolution resulting from the timing study. In the initial image (06:39:46), Source 1 on the northern UV ribbon and Source 6 on the western side of the lower ribbon produce significant emission.

These two sources fade in comparison to the others during the flare evolution and then reappear as the flare emission falls off, consistent with the timing results shown in Figure 4.7. As the UV sources of the upper ribbon activate, the emission progresses along the ribbon to the south and east. In contrast, the X-ray and lower ribbon emissions remain well-confined and generally stationary throughout the time frame of greatest activity. As the X-ray counts rise, two localized HXR sources become more apparent (see 06:40:05 image in Figure 4.8). This pair of sources act as a set of conjugate X-ray footpoints of a tightly confined magnetic loop occupying only a 20"x20" region near the eastern end of the lower ribbon. On the other hand, the UV sources brighten sequentially, consistent with the timing results, along the upper ribbon until its maximum brightening in the lower center of the ribbon (Source 4).

In addition to the UV and HXR emission, we note evidence of a magnetic connection between the temporally correlated HXR and northern ribbon UV sources in the form of a loop structure depicted in 6 25 keV X-ray emission (Figure 4.9). This elongated loop shows an evident footpoint occurring near the left end of the lower UV ribbon, nearly co-spatial with the 25 100 keV X-ray ribbon with the other footpoint existing on a weakly emitting extension of the upper UV ribbon.

From the observations in TRACE and RHESSI, we have constructed an observational picture of this flare involving two observed interacting X-ray loop structures coupled with a complex extended UV ribbon morphology. The X-ray morphology

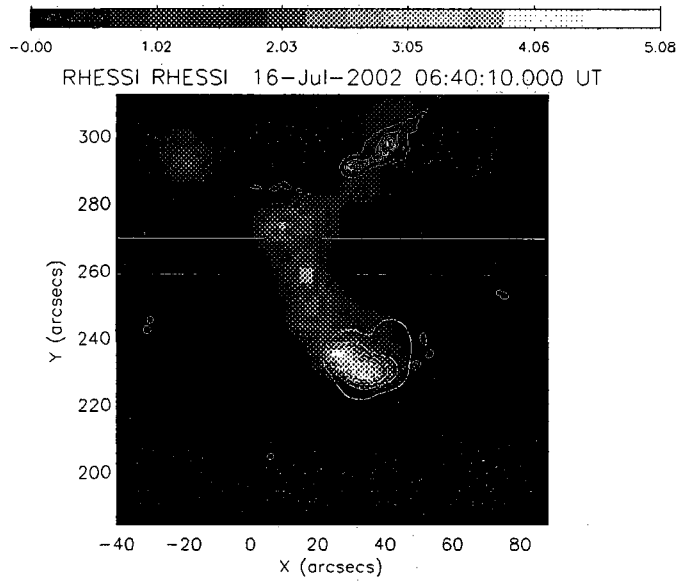

Figure 4.9 Soft X-ray (6–25 keV) image from RHESSI during a 10-second integration near the HXR peak emission (06:40:10–06:40:20) shown with the TRACE contours from the 06:40:15 image. The SXR sources indicate a soft X-ray loop connecting the two UV ribbons. One footpoint of the soft X-ray loop is cospatial with the HXR (25-100 keV) emission (shown as yellow contours).

consists of a compact hard X-ray structure 20" long exhibiting strong footpoints at 25 100 keV resulting from non thermal bremsstrahlung emission and an elongated (50" 70") thermal emission loop seen in softer X-rays linking the two UV ribbons. The emission throughout these structure must be governed by the same energy release process in order to maintain the temporal correlations observed.

An overall interpretation of the behavior of this event requires a simultaneous explanation of both the multiple ribbon structures and the temporal relationships. The

hard X-ray emission at 25 100 keV (non-thermal) and 6 25 keV ('thermal') together with the correlated UV ribbon emission strongly suggests a 3D scenario in which the reconnection is driven by the interaction of two or more magnetic flux systems. An additional and notable complication is the need to reproduce and explain the evolution of both UV ribbons with time allowing for the apparent spatial expansion of the upper ribbon while maintaining the spatial stability of the X-ray and UV emission of the lower ribbon. Since both emissions result from particles accelerating within magnetic structures in the flare region, a complex and variable magnetic topology, involving both the interactions between the observed loop structures and larger scale interactions of independent flux systems within the active region, is required to produce both the temporal and spatial variability of emission sources throughout the flare. A further explanation of this connectivity picture and its implications will be addressed in Chapter 4.1.3.

We have reported both timing correlation results and spatial development analysis to explore relationships between UV and hard X-ray emission for a medium sized flare occurring on 2002 July 16. The full field of view temporal correlation results verified findings previously reported, (Cheng et al., 1988). There were significant variations in both the temporal and spatial evolution for the individual sources identified as well as for the two composite ribbons. These developmental differences suggest a more complicated and much more dynamic system is needed to address the chromospheric

signatures of this flare than traditional loop-based flare interpretations. In the next section, we discuss of the implications of this event and address several contributing factors to explain the behavior observed. In addition, we lay the groundwork for our subsequent study of larger flares.

4.1.3 16 July 2002 Physical Interpretation

The separation of the UV emission into individual sources provides an opportunity to perform a more detailed examination of the multiple contributing components to the overall temporal behavior. Assuming the respective hard X-ray bursts are associated with particle production enhancements from reconnection sites in the solar corona, the distribution of the correlated UV emission relative to the isolated hard X-ray sources provides an observational diagnostic of the role of and structural nature of the magnetic topology in particle production and transport. For the 2002 July 16 flare, the TRACE observations detail an extended two-ribbon structure with the bulk of the UV brightening associated temporally with the hard X-ray bursts lying within the upper, or northern ribbon. This ribbon brightens in four spatially separated sources which appear in sequence as a progression over time along the ribbon.

The hard X-ray imaging data displayed a much simpler picture with the hard X-ray footpoints confined to a small area situated adjacent to the lower, or southern UV ribbon. The strong temporal correlation between the UV sources in the northern ribbon and the hard X-ray sources (separated by 50 70 arcseconds or 36,000 50,000

km) suggest a more complicated overall picture of solar flares than the single loop models of earlier work. Models such as the partial precipitation model (Kane, Donnelly, and Frost, 1979) assumed a single loop structure in which the spatial separation of the HXR and UV emission was only possible in terms of the assumed atmospheric height of the emission. In our case the clear spatial separation on the solar disk along with the localized hard X-ray emission and extended UV emission imply the need for a complex multi-component magnetic structure. Such magnetic complexity is a key aspect in the understanding of coronal mass ejections, the largest of which are often accompanied by large flares. Several models involve multipolar magnetic configurations to provide the initial conditions for eruptions to occur (e.g. Antiochos, 1998).

From the observations in TRACE and RHESSI, we have determined an observational picture of this flare involving two observed X-ray loop structures coupled to a more complex extended UV ribbon morphology. The X-ray morphology consists of a compact structure 20" long exhibiting strong footpoints at 25 100 keV and an elongated (50" 70") loop evident at 6 25 keV: the latter connecting the two UV ribbons. The emission throughout this structure must be governed by the same energy release process in order to maintain the temporal relationships observed. How this energy release process relates to the magnetic topology is a crucial question in understanding the timing signature we observe.

An overall interpretation of the behavior of this event requires a simultaneous explanation of both the multiple ribbon structures and the temporal relationships. The hard X-ray emission at 25 100 keV (non-thermal) and 6 25 keV ('thermal') together with the correlated UV ribbon emission strongly suggests a 3D scenario in which the reconnection is driven by the interaction of two or more magnetic flux systems. This overall structure is defined by the interaction along separators at the boundary of these flux systems or separatrices. The global structure is defined through the interaction of these larger temporally evolving systems, while a secondary component within the structure is the interaction between observed loops, like those seen in both energy ranges considered. We expound upon these components to provide a base for understanding the topological development of solar flares.

Role of Separatrix Surfaces

Our observation of the 16 July 2002 event provides significant evidence for a complex magnetic reconnection picture governing the overall flare emission. A plausible means of generating this implied complexity is the interaction of two, or more, separatrix surfaces via one or more common separators or QSLs (discussed earlier in Section 2.2.2). In this interpretation, the chromospheric signatures arise from reconnection at the separator and vary over time as the flux systems evolve. The evidence for this scenario is based both on the emission distributions of chromospheric sources and on the magnetic development of the active region responsible for the flare. Magnetically,

the time sequence of the MDI magnetograms shown in Figure 4.10 indicate the ongoing evolution of a strong emerging flux system, denoted S1N1, in the vicinity of the observed flare emissions. The interaction of this system with the pre-existing field is driven by continued flux emergence in the active region. As the system evolves with time, it drives temporal variations in the location and behavior of the separator(s). In this scenario, the spatial and temporal evolution of the UV ribbons are a consequence of the changing connectivity of magnetic field lines, across the separatrix surfaces, to the reconnection site.

The emission-based evidence arises from the observed evolution of the UV enhanced sources of the upper ribbon, brightening as a progression down the ribbon as the flare evolves. We see this ribbon develop predominately as a series of four separate enhanced kernels over the duration of the flare. UV emission originates from a number of mechanisms. However, the HXR emission results from the energy deposition by injected electrons through thick-target bremsstrahlung emission (Brown, 1971). Since the UV enhancements are temporally correlated, the emission in these kernels likely originates from the same energy release and associated accelerated particle population. Therefore, the individual spatially separated brightenings must result from the injection of newly accelerated electrons at the reconnection site. The spatial progression of the UV emission in the upper ribbon suggests changing connectivities between the reconnection site in the corona and the particle energy deposition sites

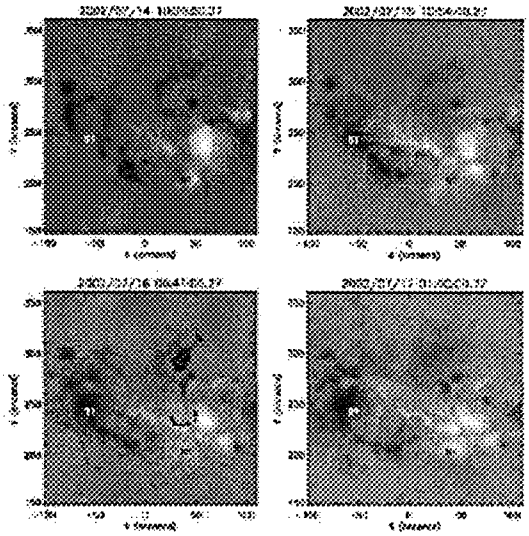

Figure 4.10 MDI magnetograms depicting the magnetic field evolution from 2002 July 15 through 2002 July 17 for AR 10030. TRACE 1600 $\AA$ contours are overlaid on the magnetogram for 2002 July 16 to provide the flare ribbon locations with respect to the magnetic field configuration. All images are differentially rotated to 06:41:00 on 2002 July 16. Over the course of the three days shown, we see significant development of the magnetic bipole S1N1. We note the continued evolution the new emerging magnetic system (S1N1) throughout the period of the flare, presumably driving an interacting with the pre-existing magnetic systems. (Alexander and Coyner, 2006)

in the chromosphere, corresponding to the enhanced kernels. The lowest energy hard X-ray emission, 6-25 keV, shows the existence of substantial heating within the volume of the flaring region enclosing both UV ribbons, which serve as outer boundaries for the flare emission in the chromosphere. To illustrate reconnection within a separator system, we refer to a cartoon depiction from Vlahos (2006) shown in Figure 4.11. This picture illustrates the interaction of two separatrix systems depicted as three-dimensional domes. The two separatrices interact along a separator and give

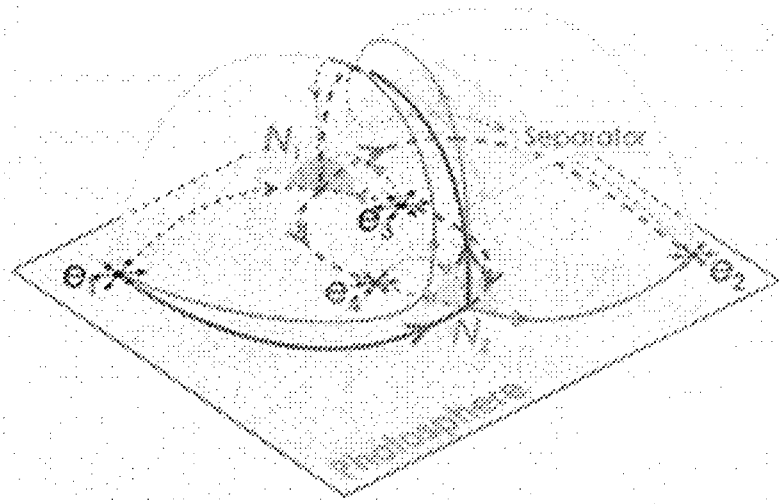

Figure 4.11 3-D depiction of magnetic reconnection along a separator due to the interact of two separatrix systems. Image taken from Vlahos (2006) based on the representation by Lau (1993).

rise to four connectivity region, given e1 and e3 are positive charges while e2 and e4 are negative. For the 16 July 2002 flare, we contend that two or more of these separatrix domains interact to produce the observed signatures for the global flaring region with these interactions of the systems occurring at separators, or QSLs, as defined by Equation 2.5. The observed progression of emission would result naturally from the evolution of a newly-emerging flux system. As these global connectivities change, we observe see the signatures of multiple ribbons, in this case the confined HXR ribbon and the longer soft X-ray ribbon, develop and interact as discussed in Section 4.1.3 providing additional evidence of the dynamical evolution of the separator(s) and

the connections within the magnetic volume, i.e. the progression of the reconnection along the separator. The more dynamic behavior exhibited by the UV source of the upper ribbon is consistent with the scenario described with the reconnection site expected to be closer to the southern ribbon near the hard X-ray emission based on the interaction point of the observed loops.

A detailed knowledge of the coronal magnetic field in this flaring region is required to confirm the hypothesis adopted above. The time sequence of MDI magnetograms in Figure 4.10 show the ongoing evolution of a strong emerging flux system, denoted S1N1, in the vicinity of the observed flare emissions. This flux system initially emerged on 14 July 2002 and gave rise to an X3 flare peaking at 20:08 UT on July 15 (see Liu et al., 2003). The interaction of this evolving flux system with previously existing coronal fields is perpetuated by the continued emergence of new flux. As the system develops, it forces the evolution of the separator(s) resulting in a time-dependent energy release reflected in the observed correlated UV and HXR emission signatures. In this scenario, the spatial and temporal evolution of the UV ribbons are a direct consequence of the changing magnetic connectivity across the separatrix surfaces to the reconnection site in the corona.

Smaller Scale Loop Interactions

As the name implies, the loop interaction scenario is a consequence of the interaction of two, or more, magnetic loop structures observed in the flare. Potential causes

of these loop interactions include the emergence of a new magnetic bipole into the flaring region magnetic system to interact with the existing coronal magnetic field or the result of large-scale photospheric motions bringing the observed loop structures together and allowing for interactions to take place. The second scenario results because the magnetic field lines are tied to the photosphere due to the dominance of plasma pressure over magnetic pressure in the photosphere. Consequently, the field moves with the photospheric plasma. If the loop fields are oriented with oppositely directed fields approaching each other, reconnection can occur to change the field configuration, releasing energy in the process (Nishio et al, 1997).

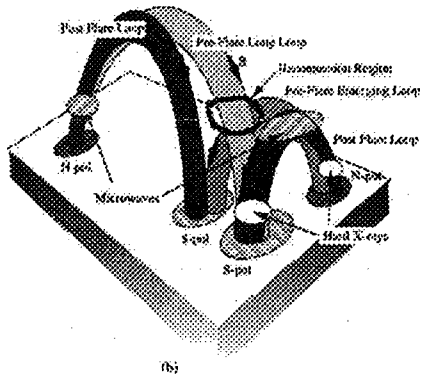

Figure 4.12 Sketch interpretation from Nishio et al. (1997) depicting the loop-loop interaction scenario as seen in their study with HXR and microwave emission

The imaging observations discussed in this chapter suggest that reconnection due to the interactions of the two loops is likely. The hard X-ray observations clearly

indicate two closely spaced sources co-spatial with the southern ribbon of the 16 July 2002 event which serve as well-defined footpoints for what we be. Such high-energy emission is the result of the interaction of reconnection-accelerated particles with the ambient ions in the high-density chromosphere. As a result the X-ray sources observed represent the footpoints of a newly energized magnetic loop. The lower energy thermally-dominated X-rays (12-25 keV) indicate a pre-existing loop connecting the two UV ribbons (see Figure 4.9) with one footpoint near the higher energy sources. This description indicates a scenario similar to that depicted in Figure 4.12. This scenario is consistent with the temporal correlation results which indicate that the brightest sources in the northern UV ribbon are correlated with the hard X-ray emission along with a strong UV source in the southern ribbon near the hard X-ray structures. The correlation between the UV ribbons indicate a direct connection between the ribbon directly leading to a loop-loop interaction picture.

While this picture can provide a suitable explanation for the bulk of the hard X-ray sources and the emission from the brighter UV sources. It is unable to explain all of the flare-associated ribbon structures or their temporal development. However, the loop-loop secenario must be a piece of a larger topological picture which distributes the energy from the reconnection site within the interaction region of the loop structures throughout the whole system.

4.1.4 Conclusions and Extensions for Further Study

The results presented here have illustrated that even for a small relatively simple flare, the dynamics of the flaring region are still highly complex. The results we present here have shown that the 3D magnetic topology of the active region plays a critical role in the development and evolution of the flare, rather than emission confined to loop-like magnetic structures. The example of this C6.5 event clearly indicates that the simplified 2-D models, like the one shown in Figure 1.6, are insufficient to fully address the observed behavior of the emission. With the results we presented here as a foundation, and the preliminary understanding of temporal and spatial development in flares, we look to expand and further generalize our results to flares of all sizes by investigating a number of larger flares observed under the same program.

4.2 Relationships Between and Evolution of Localized Emission Sources in Large Flares

The results presented in the previous sections, emphasize the importance of the spatial and temporal development of localized sources within the overall spatial emission distributions of solar flares. It is commonly anticipated that larger, more intense events will demonstrate more complex spatial and temporal development, likely the result of increased magnetic complexity and the stronger magnetic energy release. Building upon our previous investigation, we now consider the specific evolution of

large flares, those of GOES classification M or higher. We have chosen to focus primarily on the localized source relationships because, while the full field results largely only confirm the work of Cheng et al (1988), the investigation of the localized emission uses the improved resolution available from RHESSI and TRACE to gain insight into the interplay of physical mechanisms and varied available particle populations within the localized structure in flares. For this study, we have 11 events listed in Table 4.3. While each of these events has unique characteristics, there are numerous observed traits in common. To illustrate these, we will focus the bulk of this section on the analysis of the X 6.5 event from 2006 December 6. Later sections will address specific features of other events which have particular implications for timing and topological development of these large scale flaring regions.

Flare Date	*Flare Times (IIXR)*	*GOES Class*	*Comments*
04 July 2002	07:28:00–07:35:00	M 1.1	Spatial separation but temporal correlation throughout flare.
17 July 2002	06:58:00–07:08:00	M 8.5	Largely co-spatial co-temporal emission. Also Late developing UV sources with no IIXRs
19 January 2004	12:30:00–12:41:00	M 1.1	co-spatial co-temporal correlated emission; UV sources develop late with no IIXRs
10 November 2004	02:03:00–02:13:00	X 2.5	Complex multiple ribbon multiple injection event
15 January 2005	00:38:00–00:45:00	X 1.2	multiple burst event
15 January 2005	22:13:00–23:19:00	X 2.6	UV Full FOV profile differs strongly from IIXR; largely co-spatial emission; limited temporal correlation
19 January 2005	10:19:00–10:28:00	M 2.7	co-spatial co-temporal emission; multiple burst event
21 January 2005	10:12:00–10:21:00	M 1.7	co-spatial co-temporal; multiple bursts in timing
06 December 2006	18:39:00–18:56:00	X 6.5	Soft X-ray correlation with some sources; multiple bursts
06 December 2006	20:15:00–20:23:00	M 3.5	Soft X-ray correlation with some sources
07 December 2006	19:00:00–19:10:00	M 2.0	

Table 4.3 Flare events included in the individual source evolution study presented here. The X 6.5 event from 06 December 2006 will be a significant portion of the discussion contained in this and follow sections though other events of this list will be shown as further examples throughout.

To complete this study, we modified our methodology such that our localized sources are defined by a series of user-defined polygons rather than the simple rec-

tangular boxes described above. These polygons minimize the overlap between our selected sources reducing the potential of contamination between the adjacent sources while also giving a more accurate representation of the area of the selected enhancement kernels. This is more important in these larger events where sources of emission are more numerous and more closely spaced than the previous event. With this modification, we follow the procedures outlined in Section 3.2.3.

4.2.1 2006 December 6 X 6.5 Flare Overview

Among the 11 events in our study (Table 4.3) this event is the strong in terms of peak soft X-ray emission (1-8 Å) detected by the GOES satellite. In the low-energy X-rays, both from observations by GOES and by RHESSI, this event shows a long-duration smoothly developing temporal profile lasting approximately one hour in 3-12 keV RHESSI observations. It is the larger of two overlapping events, the other, an M3.5 event, evident in GOES over a three hour period from 18:00-21:00 UT. As shown in Figure 4.13, however, the 25-100 keV hard X-rays occur as a series of impulsive bursts over 17 minutes from 18:39 18:56 UT, beginning some 10 minutes after the onset of soft X-ray emission in GOES. This impulsive emission is dominated by a primary burst, spanning 18:41:00 18:46:30, followed by a second more strongly peaked burst occurring over the time range 18:46:30 18:48:30. Subsequently, three weaker bursts in the hard X-rays occur after 18:49:30, each with RHESSI photon counts less than 25 % of the peak of the RHESSI X-ray profile. While there exists

only a minimal UV response to the later hard X-ray emission impulses (see Figure 4.14), there does exist evidence of weaker ultraviolet sources active and correlated with the HXR emission during these bursts, implying that locally there is still a UV response to the energy release indicated by the HXR bursts; however, this response is weak compared to other components of the UV emission and is therefore suppressed on the larger spatial scales. We analyze the development of these individual UV sources shown in this later phase of the flare. It is worthwhile to note that each of the large impulsive bursts identified show significant temporal structure on time scales of tenths of seconds (Aschwanden, 1998). However, the limited time resolution of TRACE restricts us from considering this fine-scale structure.

In the UV, we observe that the majority of the enhanced emission sources occur along a long, predominately north-south oriented, ribbon. As is common within all the events we study here, the ribbon appears to brighten as a group of disjointed enhanced emission kernels which we show here as ten distinct UV sources, eight along the primary ribbon (Group 1) and two found more to the west and north of the main ribbon (Group 2). Many of the Group 1 sources show co-temporal brightening corresponding co-spatially with the hard X-ray emission seen from RHESSI, a departure from the spatial separations that dominated the previous event, while the Group 2 sources (Sources 1 and 2 of Figure 4.15) show significant time delays from the hard X-rays and a generally smoother behavior in time than their Group 1 counterparts.

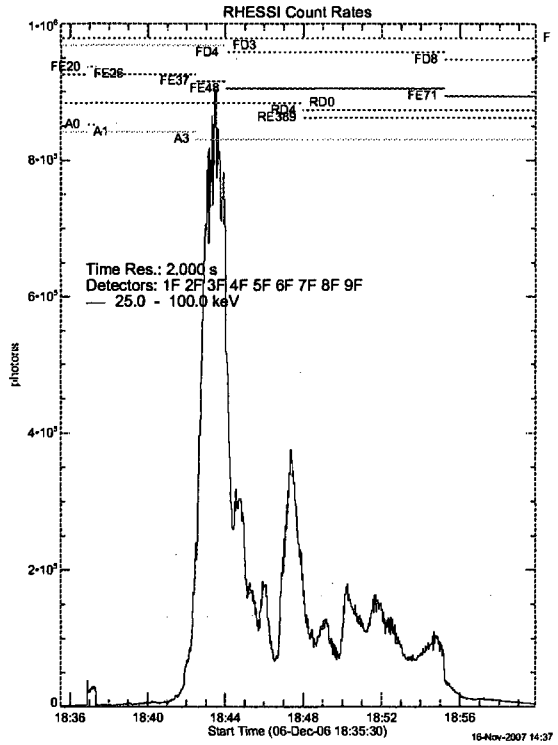

Figure 4.13 Observed hard X-ray time profile for the 25-100 keV energy range over the time range 18:36–19:00 UT. The bulk of the X=rays seen in this energy are the result of several impulsive bursts starting at approximately 18:40 and continuing to approximately 18:56 UT

We perform a linear temporal correlation analysis comparing the localized UV source emission profiles to the overall HXR emission for each source shown in Figure 4.15. The sources were numbered in order of selection generally in a southward progression through the field of view. Sources 1 and 2 are located off the main ribbon, defined earlier as Group 2. The remainder are ribbon sources included in Group 1. Hereafter the sources will be addressed by their source numbers or for collective discussion by

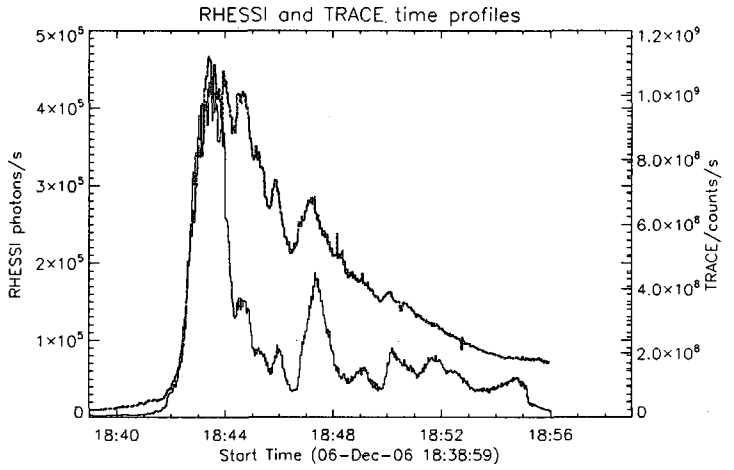

Figure 4.14 Figure 1.5 is reproduced here showing the full field of view UV profile in direct comparison with the hard X-ray emission profile for the 6 December 2006 X6.5 event. Note the time range after 18:49:30 UT. We find minimal burst structure within the UV profile for this period.

group.

4.2.2 6 December 2006 Temporal Analysis

We compare the evolution of each UV ribbon source with the spatially-integrated HXR evolution for both the duration of the flare as a whole and for individual impulses themselves. The correlation results are summarized in Table 4.4. During the primary hard X-ray burst, UV sources 3, 5 and 6, comprising much of the main ribbon (see Figure 4.15), show statistically significant temporal correlation, providing strong evidence connecting the emission signatures to the same coronal trigger event.

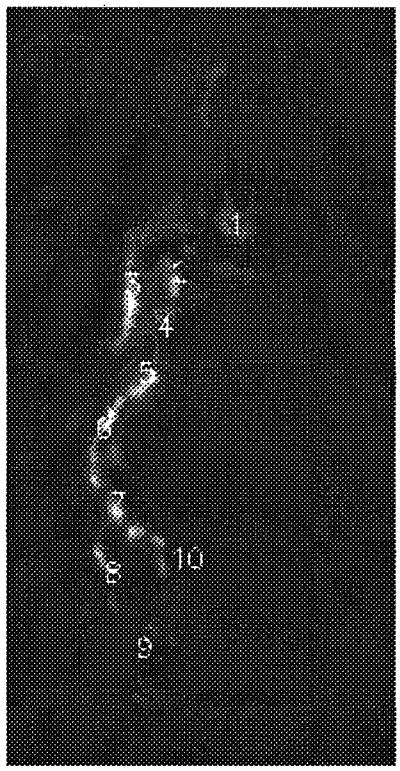

Figure 4.15 TRACE image from near the peak of the initial X-ray bursts with each of the 10 sources from the analysis presented here shown. Sources 1 and 2 develop later in time the other ribbon sources and are therefore considered Group 2 sources.

Figure 4.16 shows direct comparisons of the temporal evolution of the spatially-integrated hard X-ray emission (panel A) and the emission of UV sources 3, 5, and 6 respectively (panels B, C, and D). We are limited to the spatially-integrated X-ray emission due to the integration times required to image the localized X-ray sources, typically 10-20 seconds. The strongest temporal correlation for the entire flare as well as for the primary burst occurs with UV Source 3, with a correlation coefficient of

Time Range	*UV Source*	*R coefficient*	*Confidence Level*	*Confidence Interval*
18:41:00–18:56:00	3	0.9225	0.99	0.9024–0.9386
18:41:00–18:56:00	5	0.8673	0.99	0.8341–0.8942
18:41:00–18:56:00	6	0.7698	0.99	0.7160–0.8145
18:41:00–18:56:00	8	0.7817	0.99	0.7303–0.8243
18:41:00–18:46:30	3	0.9420	0.99	0.9153–0.9604
18:41:00–18:46:30	5	0.8488	0.99	0.7840–0.8953
18:41:00–18:46:30	6	0.7549	0.99	0.6573–0.8276
18:41:00–18:46:30	8	0.7677	0.99	0.6743–0.8369
18:46:30–18:48:30	7	0.8295	0.99	0.6957–0.9077

Table 4.4 6 December 2006 X 6.5 Event Correlation Results

0.942 for the initial burst. The three sources shown in Figure 4.16 show both a strong UV response to the flare energy release and exhibit a similar impulsive burst pattern closely resembling the bursts seen in the HXR emission. These source correlations are consistent with the overall correlation picture addressed in previous studies by Cheng et al. (1988); however, we must consider the fact that the correlated emission is only a component of the UV emission observed within the flare. Additional sources of UV flux are seen but they do not share temporal profile characteristics similar to those of the hard X-rays. The second major burst from 18:46:30 18:48:30 is directly evident in the profiles of two of the weaker UV sources (Sources 7 and 8), although the other sources in the main UV ribbon are still clearly emitting. The subsequent weaker bursts, seen in the hard X-ray emission after 18:49:30, are not clearly nor prominently reflected in the observed full field of view UV emission. This suggests that while there still exists a component of correlated, HXR-associated emission, this component is no longer as dominant as it was in the earlier impulsive bursts.

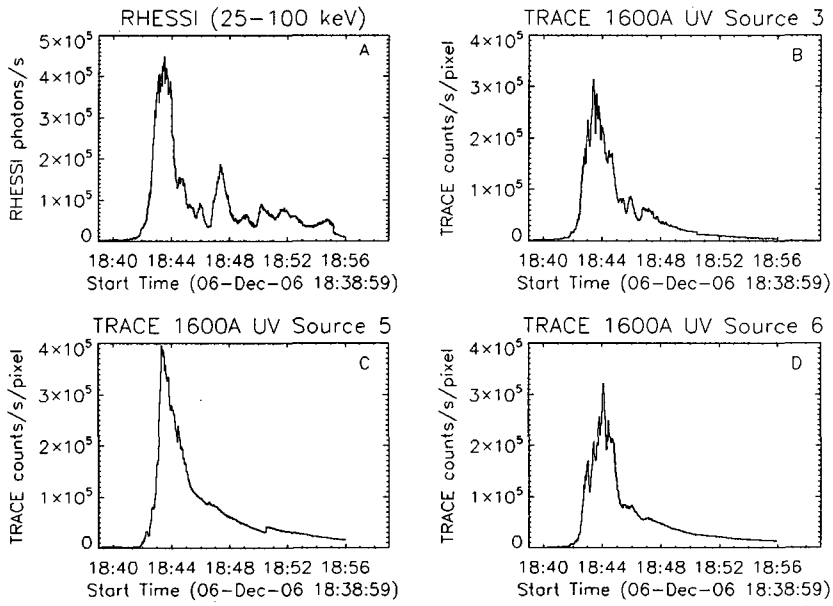

Figure 4.16 RHESSI 25-100 keV spatially integrated lightcurve (panel A) shown for comparison with the TRACE UV lightcurves for Sources 3 (panel B), 5 (panel C), and 6 (panel D). These UV sources show the strongest temporal correlation with the HXR response for both the initial HXR burst and the overall profile.

This leads to the implication that UV emissions associated with other mechanisms, such as the interactions with a thermal particle population or bulk chromospheric heating, contribute significantly to the correlated emission. The secondary bursts, in both wavelengths at later times, will be addressed later in the spatial development discussion. It should also be noted that UV emission was present from Sources 4, 9, and 10; the emission from these three sources was largely uncorrelated with the HXR emission.

Sources 7 and 8 of the UV ribbon show a clear response from 18:46:30 18:48:30 to

the secondary flare impulse. Given the different spatial locations of the hard X-ray sources for this burst, it is likely that this impulse results from reconnection occurring in a different region of the corona than the primary energy release. These emission sources are much weaker than those associated with the first burst with the UV flux found in sources 7 and 8 approximately 25 % of the of peak source flux recorded during the initial burst. During the second burst, while we see UV emission in both sources 7 and 8, only Source 7 shows statistically significant temporal correlation. Source 8 shows strong emission but actually precedes the peak of the HXR emission; although it shows significant activity no temporal correlation is evident. The southern location of these sources follows the southward development of the X-ray emission though the development of the hard X-ray is the more prominent development of this phase of the flare. This change in the centroid of HXR emission is consistent with studies of the two-phase production of a Moreton wave, a flare-associated wave seen in chromospheric emission, originating in this flare region (Gilbert et al., 2008). The coincidence between the flare location and the origin of two Moreton waves can be viewed as observational signatures of a sequence of strong energy releases associated with filament activation and the eruption of a powerful CME. The subsequent weak X-ray bursts after 18:48:30 are in large part unseen in the UV emission. Only UV Source 8 shows any burst-like emission after 18:49:30 despite consistent and strong HXR emission visible in the southern regions of a weakened UV ribbon. We perform

further analysis of individual UV sources seen during this later portion of the flare shown in Figure 4.17.

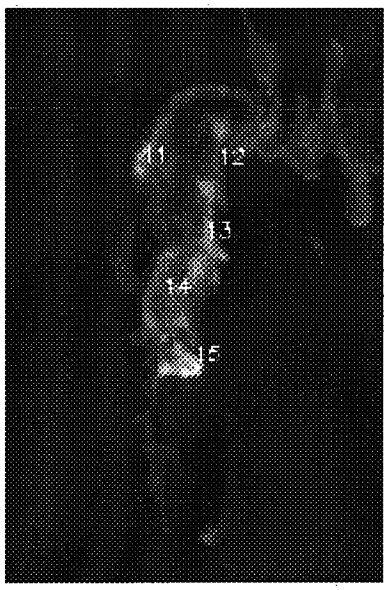

Figure 4.17 TRACE image during the latter stages of the flare showing the 5 active UV sources seen after 18:49:30 UT shown as Sources 11-15 for easier reference. These source selections are used in the discussion of the later X-ray and UV behavior only.

Of these five sources, only one shows a significant temporal correlation (Source 15) with a correlation coefficient of 0.8981 for the time frame 18:51:00 18:56:00 UT. A comparison of the HXR time profile with that of Source 15 is presented in Figure 4.18. The spatial development of these later sources occurs primarily along the existing UV ribbon and does not include a co-spatial UV source development with the intense HXR source.

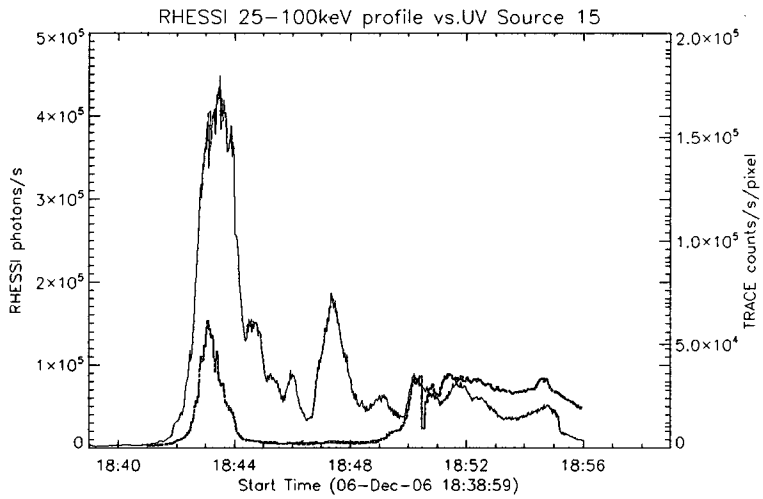

Figure 4.18 Comparative time profiles for RHESSI 25-100 keV emission and TRACE UV emission for Source 15 as shown in 4.17

4.2.3 6 December 2006 Spatial Analysis

In the previous section, we confirmed the existence of a strong temporal correlation between UV sources along the main UV ribbon and the overall spatially-unresolved HXR emission suggestive that both emissions are governed by the same time-dependent flare impulse although with a clear spatial development in the UV; however, in order to further clarify the nature of the driving mechanism, we must investigate the spatial development of the emission kernels in both wavelengths and any relationship between them. We focus here on specific localized sources as we follow the evolution of the flare during each of the critical impulses of activity. The

high-cadence UV observations allow us to track the UV source evolution throughout the duration of the HXR activity; however, in order to produce spatially-resolved maps of HXR emission, we require integration times of at least 10 seconds for the image reconstructions to remain statistically significant.

For the main impulse, 18:41:00 18:46:30, the bulk of the UV emission evolves along a segmented north-south oriented ribbon approximately 120 arcseconds (87Mm) in length. The main ribbon can be divided into northern, central, and southern components each possessing significant UV enhancements in the forms of the numbered sources discussed previously . The hard X-ray emission (25-100 keV) is concentrated into two main sources. The more northern HXR source is fairly localized (covering an area approximately 20 x 10 arcseconds-squared) while the southern HXR emission region initially appears as a more extended source; however, as the HXR emission in this region evolves this source complex becomes resolvable into multiple footpoints.

The HXR sources are seen to be co-spatial with their UV counterparts particularly along the northern and central portions of the main ribbon. Figure 4.19 shows a pair of spatial map overlays depicting the evolution of the UV and HXR (25-100 keV) emissions for a 40 second sequence centered near the peak emission time of the primary HXR burst. The northernmost X-ray source is essentially co-spatial with UV Source 3 while the southern X-ray emission extends along the central region of the flare ribbon, co-spatial with the UV Sources 5 and 6. This spatial analysis

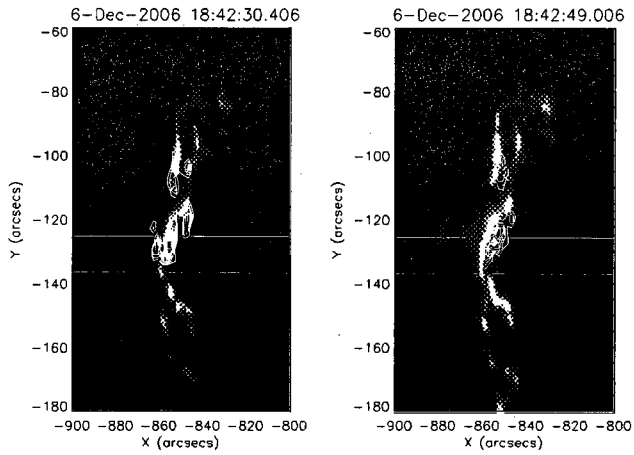

Figure 4.19 TRACE and RHESSI map overlays for 40 seconds near the peak of the initial HXR burst. HXR data shown 25-100 keV emission with contours corresponding to greater than 20 percent of the respective image maxima.

is consistent with temporal correlation results shown in the previous sections. The existence of localized HXR emission co-spatial with the temporally correlated UV emission sources is suggestive of emission results in line with models put forth by Kane, Donnelly, and Frost (Kane and Donnelly, 1971; Donnelly and Kane, 1978; Kane, Frost, and Donnelly, 1979) where both sets of emission result from different parts of a single accelerated electron population, which reach different heights in the atmosphere based on the particle energy; however, this loop picture is only a component of the overall emission. UV brightenings beyond those associated directly with the HXR production sites, including the Group 2 sources which brighten with significant time delays compared to hard X-ray emission, are seen within the UV

data. Also, as this event evolves, we see the development of a strong isolated HXR sources clearly separated from the UV emission discussed in greater detail in the next section. The combination of these observations imply that the emission picture in the standard flare scenario can only account for a portion of the emission observed. Spatial separations between correlated emission developing at different times in the flare suggest the need for a complex magnetic topology within the flaring region which evolves over time. Finally, the development of delayed sources indicate that UV emission could plausibly be in response to additional physical processes than sole direct injection of non-thermal electrons.

4.2.4 6 December 2006 as a Multiple-Burst Event

For five of the large events in this study, we see temporal profiles which show multiple impulsive bursts of significant intensity over the course of the hard X-ray emission. Of particular interest in these events is the evolution of the HXR source emission for each burst relative to both the prior bursts for the event and the corresponding evolving UV emission. One such key example is the 6 December 2006 event which has been the focus of this section. In the December 6 event, we see that the later bursts, primarily from 18:46:30 18:48:30 with subsequent minor bursts in the HXR after 18:49:30, are dominated in the hard X-rays by an intense and more southerly located HXR source beginning near the center of the UV ribbon and progressing over time to the south and west (see Figure 4.20). The nearest UV sources to the dom-

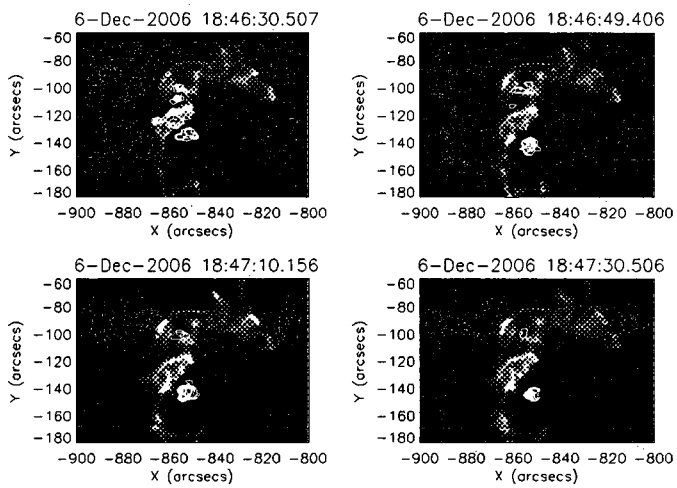

Figure 4.20 TRACE and RHESSI map overlays for an 80 second period during the second HXR burst from 18:46:20–18:47:40. HXR data shown 25-100 keV emission with contours corresponding to greater than 20 percent of the respective image maxima. We note the develop of a strong southern HXR source with no direct UV counterpart.

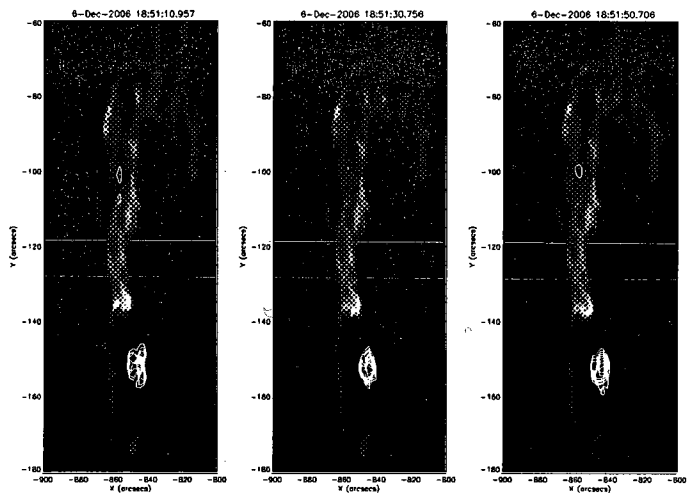

Figure 4.21 Map overlays for a 60 second interval between 18:51:00–18:52:00. There is a clear, strong HXR source in the southern part of the FOV consistent with the southward X-ray development. However, there is not a significant corresponding co-spatial UV source.

inant X-rays for the bulk of the secondary burst are Sources 7 and 8. In relation to the temporal analysis, these sources show significant activity during the interval of interest, both possessing a significant rise in emission 18:46:30 18:48:30 with source 7, in particular, showing a significant correlation with the HXR emission (correlation coefficient of 0.8295). Despite the temporal correlation and spatially proximity, there is no directly co-spatial hard X-ray emission apparent for either Source 7 or 8. During the later stages of the flare (after 18:49:30 UT), the X-ray source to the south and west of the UV persists. However there is again a significant separation between the HXR source and the most significant UV brightening (see Figure 4.21). Spatially-separated, temporally correlated emission is consistent with the ideas dis-

cussed by Alexander and Coyner (2006) and is suggestive of a required interacting 3-D system to successfully reproduce the observed emission in all locations. A fading HXR source appears on the northern-central portion of the UV ribbon; however, this source is weakening throughout the later evolution of the event while the aforementioned southern source remains strong. As the flare evolves after 18:49:30 UT (see Figure 4.21), the bulk of the HXR emission is still confined in an intense HXR source significantly separated from the bulk of the UV emission lying to the south and west. The UV emission is dominated by a bright source near the southern tip of what was the central ribbon fragment in the earlier emission. This brightening (Source 15 from Figure '4.17) shows strong temporal correlation with the HXR emission. However, there is no corresponding co-spatial activity in the UV and HXR emission distributions suggesting again a larger scale structure is necessary to connect the emissions. The development of the strong southern kernel of HXR emission, which did not exist during the primary HXR impulse, indicates a probable second flare event involving a distinct group of magnetic structures. The southern location of this new HXR emission for the later bursts (including those not apparent in the UV profile) is consistent with the derivation by Gilbert et al. (2008) of a set of two temporally and spatially separated origins of two chromospheric waves associated with these events. The additional and distinct energy release suggests that an evolving, and complex magnetic topology is required to produce the distinct and separate emissions as the

flare evolves.

4.2.5 Further Examples of Multiple Burst Events

Multiple impulse activity, such as described above, is similar to that seen in other M and X class events in our study with complex temporal profiles. A second clear example of a multi-burst event is the 2004 November 10 X2.5 flare. Figure 4.22 displays the overall HXR time profile along with a series of four UV and HXR map overlays corresponding to the four impulsive bursts in the HXR profile of the November event. We see that each of the bursts corresponds to a different set of HXR footpoints localized to small portions of an active and complex UV ribbon system observed by TRACE. Each of the bursts shows that the strongest UV and HXR activity exists in close proximity, confined to localized regions within a much larger complex UV ribbon system. Each of these bright UV sources demonstrates a statistically significant correlation with the overall HXR emission for the respective burst in question. The observations of separate sets of footpoints corresponding to different bursts within the time profile suggest multiple-burst flares can be envisaged as a series of reconnection-driven events isolated to different regions in the solar corona, likely the result of the interaction of distinct magnetic systems within an evolving topology of the overall flaring region. While the X-ray sources and the correlated UV emissions are reasonably compact and localized for each impulse, consistent with direct particle injection from a nearby reconnection site, the overall extended UV ribbons

still remain consistent emitters and are continually visible in the TRACE images. This suggests that the non-thermal electrons responsible for the hard X-ray emission are likely only responsible for a portion the visible UV emission. For regions of UV emission not corresponding to a direct energy deposition site, the UV emission may arise in part due to other mechanisms. Possibilities include the effects of a thermal electron population or bulk heating of the chromospheric flaring region via thermal conduction fronts (Czaykowska, Alexander and DePontieu, 2001; Wülser et al, 1994).

Another example of a multiple burst event is the X1.3 event of 2005 January 15 (Coyner and Alexander, 2006). Its X-ray emission shows three distinct impulses. The first two are rather short duration pulses of approximately 40 seconds. The UV emission for the event covers a long east-west oriented ribbon which shows the common fragmentation of UV ribbons into disparate sources. For these extended ribbons the most significantly temporally correlated emission occurs at the endpoints (labeled as Sources 1 and 2 in Figure 4.23 top) of the visible UV ribbon for the first two of the 3 impulses. Both these sources show clear temporal correlation for the two strongest peaks. Spatially the X-rays evolve over the course of the flare with the HXR emission beginning as a general large source in the center of the UV ribbon, distant from the correlated endpoint emission early on but as the flare approaches its peak, it evolves into a number of distinct discernible footpoints running the length of the UV ribbon. One source develops co-spatially with the temporally correlated west

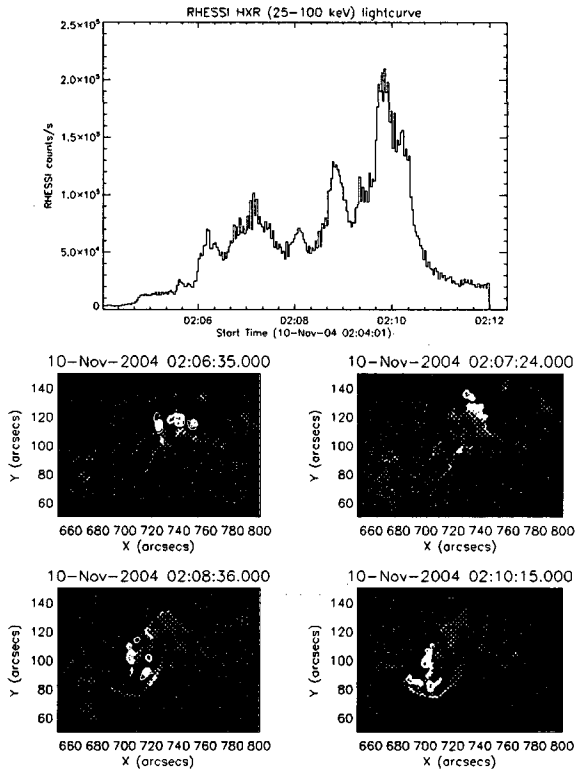

Figure 4.22 Top: RHESSI 25-100 keV lightcurve for 2004 November 10 02:03:00–02:12:00 UT. Bottom: A set of four UV and HXR map overlays corresponding to four distinct bursts in the time profile illustrating the evolution of the 2004 November 10 event.

endpoint (Source 1 in Figure 4.23). See Figure 4.23 for a clearer representation of the spatial HXR evolution during the peak emission.

4.2.6 UV Sources Uncorrelated with HXR Emission

While the primary focus of this study is the evolution of localized UV sources with respect to the hard X-ray emission, there are four events that provide evidence

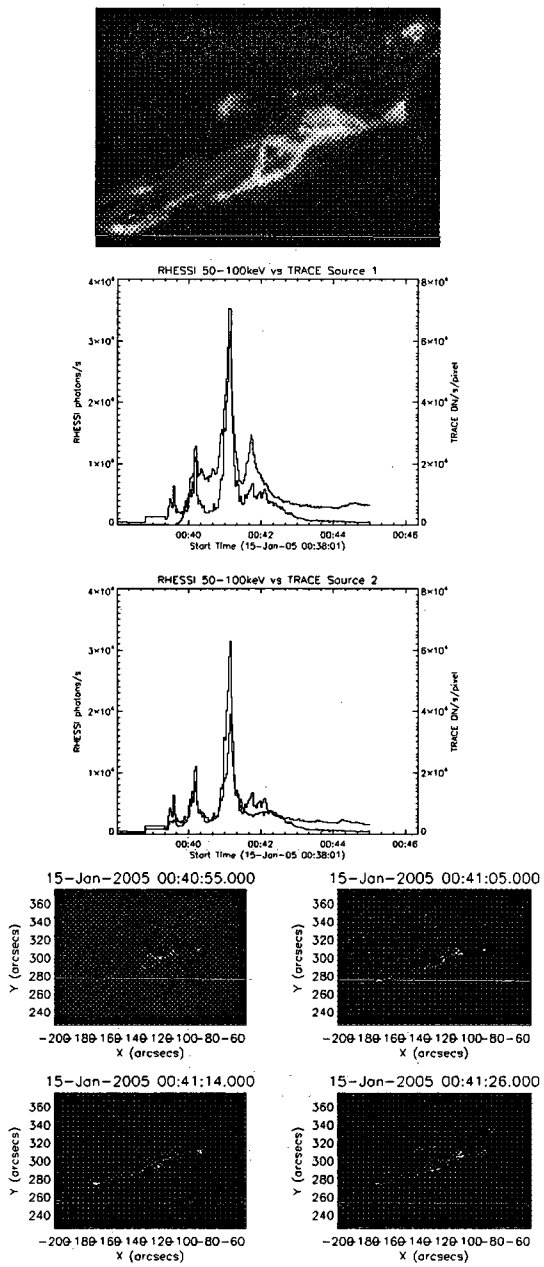

Figure 4.23 Example of TRACE ribbon with 2 sources used in lightcurve comparisons below (top) Lightcurve comparisons between RHESSI 50-100keV with Sources 1 and 2 as marked above (middle) and a series of images from the peak of the flare showing the contours of the hard X-ray emission for each image (bottom)

of significant UV brightenings with a delayed onset and no significant correlation to the high-energy HXR emission, in either space or time. As examples of these events, we discuss here the nature of the sources for the two 2006 December 6 flares, the X6.5 event discussed throughout this chapter and an M3.5 evemt beginning at 20:15 UT. For the X 6.5 event, the Group 2 sources, existing off the main ribbon, exhibited significant onset delays and varied profile shapes from that of the hard X-ray emission. We see the bulk of their development occurring approximately 2 minutes after the peak of the strongest impulse of HXR emission. UV source 1, which is the farthest from the main ribbon of emission, shows a significant time delay and slower rise than many of its HXR-correlated counterparts. We find no significant temporal correlation between the HXR emission and the UV sources (R=0.266 for Source 1) The source shows the general profile characteristics of the 6-25 keV X-ray emission with a more significant correlation. This emission is believed to be largely thermal emission. This indicates a departure from the direct injection of non-thermal particles responsible for the HXR-correlated emission.

Figure 4.24 shows the comparative time profiles of UV source 1 and the profile of the lower energy, 6 25 keV, X-rays. The lower energy X-rays show a single longer duration event compared to their higher energy counterparts, having a discernible emission profile from 18:42:30 18:49:30. It reaches its peak emission at 18:44:54 followed by steady decay. UV source 1 shows similar delayed onset and a similar ex-

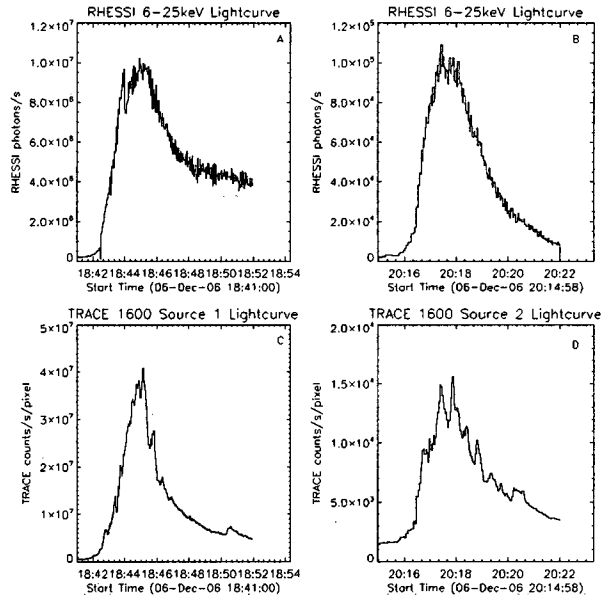

Figure 4.24 Comparative lightcurves for delayed onset UV Sources and 6-25 keV X-ray emission for the X 6.5 event (panels A and C) and the M 3.5 event (panels B and D) from 2006 December 6.

tended profile to the SXR emission curve. We have performed a correlation analysis on the localized UV sources and soft X-ray emission and find that source 1 shows the strongest correlation (R=0.8844) for the burst duration and has a similar peak time to the SXR profile (source 1 peaking at 18:45:07). It is important to note that these profiles are significantly delayed from the peaks of the HXR profiles (the HXR profile peaks at 18:43:29 85 seconds prior to the SXR curve).

A second example also included in Figure 4.24 comes from the analysis of the later M 3.5 flare from 2006 December 6. In this case, the HXR profile shows a drastic and

rapid rise to produce a short duration X-ray burst; however, one of the UV sources shows a much slower rise and more gaussian form than the HXR profile with the peak occurring significantly later in the evolution. Comparing this source profile with the 6 25 keV X-ray observations, we find significant statistical correlation (R=0.9610) between the temporal development at the two wavelengths. Again, unlike the 25-100 keV HXR profile which peaks sharply at 20:16:50, the soft X-ray profile peaks 20:17:27 and the UV Source 2 at 20:17:53. In both these examples the significant time delays and deviation in temporal profile shape from the HXR emission suggest that these UV sources are likely responding to a different component of the flare activity than the non-thermal particles believed responsible for the hard X-rays. The source profiles shown show a much smoother, more gaussian profile, suggesting a strong contribution from thermal emission (see next section).

4.2.7 Interpretation and Conclusions

Observational Summary

The observations discussed in the previous section present a summary of our 11-flare study. While each event is unique, we find a number of interesting traits which tend to arise in these events using chromospheric emission from the UV and hard X-ray observation as diagnostics of the complex magnetic structures and energy release development in large M and X class flares. We find for all of the events studied the UV emission develops in complex, fragmented, ribbons with UV enhancements in small

localized kernels. For 10 of the 11 events, during the initial impulses, we find the bulk of the temporally correlated UV and HXR emission to be co-spatial as well as co-temporal; although, for later impulses there are significant contributions to the UV in addition to the co-spatial emission resulting from particles accelerated to produce both X-ray and UV emission. The HXR emission for all the events is consistently more localized than the UV which shows a more extended development. Analysis of the individual UV and HXR sources provides critical insight in the magnetic evolution of these large flare events.

A primary result is the confirmation of the temporal correlation of the overall hard X-ray profile with observed UV source profiles, and the subsequent comparison of the spatial distribution of emissions in both these crucial wavelengths. Our analysis of these flares finds several localized UV sources which show a strong correlation with the X-ray temporal profile, consistent with the results seen for earlier spatially-unresolved studies, like those conducted by Cheng et al. (1988). Our comparisons of the UV and HXR spatial distributions demonstrate that for 10 of the large flares the strongest sources of temporally correlated emission are co-spatial with the resolved X-ray sources at energies above 25 keV during at least the initial bursts of flare energy. Later bursts however show indication of significant spatial separation between the UV and HXR temporally-correlated emission lending support to the need for more complex magnetic structures which must evolve over time to reproduce the disparate

emission kernels. It is also noteworthy that the UV emission shows a greater spatial extent than the HXR emission indicating that emission persist throughout the flaring region. This indicates that additional mechanisms such as chromospheric heating or other thermal processes could also contribute to the UV emission for the flares. These observations indicate that the simple injection of non-thermal electrons from the energy release site is insufficient to characterize all the emission seen within the flares.

In six of the events studied here, we find that the temporal profiles of the hard X-rays demonstrate evidence of multiple bursts of impulsive flare activity (only 5 in the UV emission). In these events, with the exception of the 2004 November 10 event, the initial burst is the most intense energy release while the subsequent bursts are diminished in flux but still exhibit impulsive character. Each of these bursts correspond spatially to a new set of X-ray footpoints in a spatially distinct locations within the UV ribbon system. This combination of temporal and spatial observations strongly imply that these event could result from one or more secondary reconnection events creating the subsequent impulses. These impulses in flares are believed to be governed by the interaction of the magnetic field in the corona above the flaring region. One plausible explanation of these later bursts is that they would be less intense energy releases from newly developed reconnection events as the complex magnetic configuration relaxes into one of many available equilibrium states until reaching a

stable nearly potential final configuration. This is consistent with the theoretical investigations of BC Low which describe the evolution of tangential discontinuities and current sheets to release energy from the complex magnetic field (Low, 2006). Low's study found that a 3-D bipolar field can be mathematically shown to have an infinite number of equilibrium states of varied energy. The transition between these equilibrium states spawns from the formation of a current sheet near a developing tangential discontinuity in the magnetic field. These current sheets allow for the release of free magnetic energy through an additional reconnection which would directly translate to an additional impulses of chromospheric emission.

Spatially, we find that these subsequent bursts often correspond to independent sets of X-ray footpoints developing in different localized regions within the envelope of the flare, typically defined by the observed UV ribbon system. The new X-ray footpoints often correspond to localized brightenings in the UV. However, we find some cases where spatially separations do develop. These additional brightenings are superimposed on the persistent ribbon-like structure observed by TRACE. This implies that while the most intense activity occurs in association with a localized reconnection, the extended emission indicates that the entire complex flare region is still actively dissipating energy.

These observations have direct implications for the magnetic evolution of the flaring region by provide observational support to the largely theoretical understanding

of the importance of 3D magnetic reconnection and the interaction of structures such as separatrix surfaces and their boundaries, the separators. These multi-burst events, in particular, show clear response to multiple reconnection events within the corona, requiring that reconnection within flares is not a static process but can be temporally-evolving as a result of a changing 3D field. Also the continuous emission from the complex UV ribbons throughout the flaring region indicates the particle acceleration and energy dissipation occurs throughout the flaring region

Finally, we discussed the existence of UV sources which do not exhibit the strong relationship between the UV and the HXR emission seen in prior studies. These sources, as observed in both 2006 December 6 events, develop spatially separated from the main ribbon of UV and HXR activity and show a significant time delay of order minutes from the onset of the HXR burst emission. These sources exhibit much broader emission profiles and are more generally correlated with the lower energy (6-25 keV) X-ray emission, suggesting a thermal origin, in direct contrast to the non-thermal particles theorized to cause the observed impulsive phase HXR emission.

Implications for Particle Transport and Magnetic Topology

Recently, a number of studies have highlighted the importance of the 3-D magnetic topology described by the distribution of the separatrix surfaces and their interaction at special field lines called separators The separators, or in more practical cases quasi-separatrix layers (QSLs), serve as preferred locations for magnetic reconnection and,

by extension, flare energy release within the corona (Démoulin et al., 1993; Longcope, 1996; Metcalf et al., 2003; Titov et al., 2002). These separators and their associated separatrix systems have been directly linked in recent studies to the chromospheric flare signatures we observe. In wavelengths such as Hα and hard X-rays it has been demonstrated that the observed footpoints and emission ribbons occur along the intersections of the separatrix surfaces with the chromosphere (Metcalf et al., 2003; Mandrini et al., 1997; Longcope et al., 2001). While we present here a number of direct implications from the analysis of radiative emission signatures, in order to fully address and characterize solar flare activity, it is critical to link the observed temporal and spatial signatures to the physical processes and magnetic environment that result in large flares. Such a study of the magnetic field development for flaring active region will be reported in Chapter 5.

In accordance with the general complexity of large flare event regions, our observations provide evidence for large flares being the result of time-varying evolution of the 3-D coronal magnetic field involving the interaction of multiple bipolar flux systems to quickly release large quantities of magnetic free energy through the relaxation of the non-potential magnetic field. The necessity for time-varying flux systems and energy release is two-fold. The multiple UV and HXR sources exhibiting co-temporal behavior show the strongest emission and are often but not always found to be co-spatial, consistent with the models of Kane, Frost, and Donnelly (1979); however,

the additional observations presented here require a more complex overall picture. While the spatially-integrated profiles and the strongest individual sources have the observed temporal connection for the most intense bursts of hard X-ray emission, there exist intense emission signatures which persist with no simple co-spatial equivalent. While the UV sources appear in extended ribbons, the HXR signatures are more localized sources occurring only on portions of the visible UV emission ribbons similar to the results put forth by Warren and Warshall (2001). UV ribbons, delineating the extended boundaries of the flare emission region, require that the magnetic topology of these flaring regions must be a 3-D system in which likely multiple separatrix surfaces must intersect the chromosphere along the visible UV ribbons to facilitate the emission seen.

For the larger events, we see temporal profiles consisting of multiple impulsive bursts of HXR emission. In these events, we find that the individual bursts relate to independent spatially-disconnected sets of HXR footpoints. Such a multiple reconnection scenario is observationally supported by the X-ray image sequences similar to those shown in Figure 4.22. Here, we observe an initial set of footpoints in the western half of the flaring region, containing strong X-ray emission visible from approximately 02:06 02:08 UT. Subsequently a set of three HXR sources emerge in eastern portion of the flaring ribbons along a distinct set of UV sources. As the flare energy is released from the magnetic field, the field relaxes into a lower energy con-

figuration. As the field changes, the development of new HXR sources suggests the separatrix systems within the active region interact in a spatially different location to produce an additional location for further reconnection elsewhere in the corona. This would permit the active region field to further relax consistent to the findings of Low by releasing additional energy and producing the second set of HXR sources.

A final implication particularly related to energy release in these large flares is that multiple physical processes may be necessary to produce the observed chromospheric emission. In the case of the most intense sources visible in either wavelength, the co-temporal, co-spatial emission implies that both the HXR and UV emission for these source can be traced to a common coronal origin and result from the same physical processes, believed to be impulsive injection of non-thermal electrons. This picture is similar to the scenario put forth by Kane, Frost, and Donnelly, where emission signatures at different wavelengths occur at different heights in the solar atmosphere, based on the energies and pitch angles of the contributing electrons. We must be able to address the persistently visible emission from the entirety of the complex UV ribbon system and the UV emission seen during the later small X-ray bursts in the 2006 December 6 X6.5 event. For these later, weaker HXR bursts (18:49 18:56 UT), the UV time profile shows a steady decline which more closely resembles that of a thermal decay rather than a response to a non-thermal source (see Figure 4.14). Incorporating these emissions and the observations of delayed UV sources evolving

away from the main ribbons of activity would require that the UV emission arises from at least two distinct sources: a response to the directly-injected particle population from the flare impulsive phase and a more delayed response to the bulk heating of the chromosphere as the flare progresses.

Interpretation of Delayed UV Sources

Studies of observed chromospheric signatures of flares have provided evidence for multiple processes involved in their production. Kitahara and Kurokawa (1990), in a study of Hα and hard X-ray emissions in flares, found Hα sources with time profiles of three distinct types, matching the profiles of hard X-ray, soft X-ray, and thermal conduction front associated emission. In our analysis, we find UV sources in 4 of our events which display sources that exhibit a significantly delayed response from the temporal behavior of the hard X-ray emission. These sources generally evolve away from the main ribbons of UV activity and, while weaker than their hard X-ray associated counterparts, persist throughout the latter stages of the flares. These sources deviate significantly from the the hard X-ray association which dominates the full field of view UV emission; however, their temporal behavior possess comparable delays, characteristics and statistically significant correlations with the lower energy X-ray emission (6-25 keV). This is important to note because it has been shown that softer X-ray emission arises from thermal processes or the acceleration to higher energies of a thermal component of the electron population generated by the coronal

magnetic energy release within the flare process (Joshi et al., 2007).

Our findings detailed in chapter show that while the complete flare region emission profiles for both wavelengths show strong temporal correlation and similar temporal evolution in the vast majority of cases confirming the spatially-unresolved results of previous studies (Cheng et al., 1988). However, when our temporal and spatially analysis is applied to well-resolved localized sources, we find a much more complicated emission picture where the co-spatial and co-temporal emission expected in most flare models serves as only a component of the emission distribution seen while spatial separated correlated UV and HXR emission and late developing UV sources are also present. Within many of these flares, we see localized, temporally correlated ultraviolet and X-ray sources which show clear spatial separation. These separations along with the temporal correlations provide observational support for the need for a time-varying 3-D magnetic topology of the flaring region governing the particle transport and emission within the flare. For many of the large events we find temporal profiles with multiple intense impulsive bursts with each burst corresponding to a unique set of hard X-ray emission sources. These observations suggest that these later impulses could result from additional reconnection events within the coronal field. In the next chapter, we will further explore the connections between the evolution of the chromospheric emission and that of the coronal magnetic field. Finally, we find evidence within these events of emission sources which depart drastically from

the temporal correlations observed in the bulk of the emission. These delayed onset sources show a clearer association in time and in profile characteristic with the lower energy X-rays believed association with a thermal population of particles.

The studies detailed in this chapter demonstrate that the standard flare model, which predicts co-spatial and co-temporal hard X-ray and ultraviolet emission, only accounts for part of a more complex emission scenario within flares. Our results have shown evidence for temporally correlated but spatially separated emission requiring the existence of a complex magnetic topology to transport accelerated particles and produce the observed emission. In complex events, showing multiple impulses, we find that these events can be related to multiple magnetic reconnections as evidenced by disparate HXR source distributions corresponding in time to different impulses of X-ray emission as the flare progresses. We also find a number of sources in the UV which develop with significant delays compared with the HXR emission with these sources strongly related to lower energy most likely thermal emission. This is suggestive that, in addition to the bremsstrahlung emission and direct heating of the chromosphere by precipitation of non-thermal electrons, additional thermal particles or thermal physical processes contribute to the flare emission.

Chapter 5
Relating Hard X-ray Evolution to Changing Magnetic Topology

In the previous chapters we have discussed the important role of the solar magnetic field in the creation and evolution of solar transients, particularly solar flares. Flares produce emission resulting from the acceleration of particles due directly to the release of magnetic energy from the relaxation of the solar coronal field. As a result, a study of solar transients must, at least in part, address the nature of the magnetic topology of this field and how its structure varies over time to release energy and accelerate particles. As discussed in Section 2.2.2, the complex 3-D field structure can be described by constructing separatrix surfaces each containing an independent bipolar magnetic flux system with the complex active region field. These separatrix surfaces can then interact due to either photospheric motion bringing existing separatrix systems together or due to the emergence of new separatrix systems within the active region, as new magnetic flux rises from below the photosphere to increase the complexity of the growing active region. Locations where these systems interact are naturally evolving locations for magnetic reconnection to occur as oppositely directed field are brought close enough together to allow for diffusion across the field and changing of connectivity. The location of these interactions have been suggested to be coincident with defined magnetic separators, single field line boundaries between

these magnetic systems serving as a 3-D representation of a neutral line or polarity inversion line separating the oppositely directed fields and spawning current sheets and reconnection in the corona (Priest, Longcope, and Heyvaerts, 2005; Longcope and Magara, 2004).

For complex systems where no absolute magnetic nulls can be found, structures known as quasi-separatrix layers or QSLs can be determined from the existence of large discontinuities in the coronal field. Interaction of these fields initiate magnetic energy release and significant particle acceleration (seen observationally through chromospheric emission kernels), create and then dissipate large coronal currents via the existence and gradual disappearance of strong current sheets, and modify the magnetic topology to lower energy equilibrium states by changing the magnetic connectivities within the larger systems eventually arriving at a near-potential equilibrium. While our discussion in Section 2.2.2 was largely theoretical, the observations presented here provide direct evidence of the importance of separators, QSLs and the overall separatrix systems to the solar magnetic field development and, most critically, the role of the magnetic field in initiating and prolonging the flaring process and provide us with a visible constraint on the nature and structure of the magnetic configurations in regions of the solar atmospheric where direct magnetic measurements are not possible.

The work presented in this chapter will focus primarily on the discussion of the

hard X-ray evolution for a pair of flare events from NOAA active region 10720 in an attempt to relate the observational signatures and evolution to a model-based understanding of complex magnetic fields and the particle acceleration associated with them. We focus here on observations of the hard X-ray evolution and its relationship with the magnetic field. In this particular study, we analyze the evolution of two large flares within NOAA Active region AR 10720 in hard X-rays from 25-100 keV. While this active region produced a number of large events as it crossed the solar disk, we focus on two large flares from 17 January 2005 due to the availability of complete RHESSI data and the availability of vector magnetograms for magnetic field extrapolations. We report here on the hard X-ray structure and the relation of its evolution to the location of separators or QSLs within the magnetic topology of AR 10720. To determine the location of these QSLs and separators, we rely on force free magnetic field extrapolations constructed by our colleague Lirong Tian, which are detailed in Tian, Alexander, and Coyner (2008) hereafter TAC.

5.1 Magnetic Field Extrapolation Techniques

While the solar environment is not a force-free environment as a whole, it is widely considered a valid assumption for solar studies that the regions between the chromosphere and the corona beyond approximately 600km above the photospheric surface (Metcalf et al., 1995). Force-free extrapolations rely on two main equations of electrodynamics:

$$\nabla \times \mathbf{B} = \mu_0 \mathbf{J} = \alpha \mathbf{B} \tag{5.1}$$

$$\nabla \cdot \mathbf{B} = 0 \tag{5.2}$$

where $\mathbf{B}$ is the magnetic field vector at a given point in the solar atmosphere and $\mathbf{J}$ represents the stored currents within the magnetic field. The force-free parameter α is, in general, variable throughout the atmosphere as a function of location. As a result these extrapolated fields are classified as *non-linear force-free fields.*

To advance our study of the magnetic structure in the upper solar atmosphere, we adopt a linear force-free extrapolation to reconstruct the 3D magnetic fields in the chromosphere and corona. This method applies equations 5.1 and 5.2 with an observed photospheric boundary field in order to determine the magnetic structure of the chromosphere and corona: when adopting the simpler *linear force-free* case, the force-free parameter α is constant everywhere on the boundary. Both linear force-free and non-linear force-free field extrapolations use a lower boundary condition input of the measured photospheric vector fields. The photospheric fields are measurable due to the increased strength of the field, and detectable measurements of Zeeman splitting determined via doppler shifts in both left and right circularly polarized light measured with MDI. The difference between these values is a measure of the Zeeman splitting which determines the magnetic field strength. (Scherrer et al. 1995). The magnetic fields are then determined for each point in the corona in accordance with

Equations 5.1 and 5.2 to extrapolate the complete field. The locations of quasi-separatrix layers or QSLs are then determined from the computed 3-D magnetic fields according to a mathematical definitions based on regions of strong gradients in the magnetic fields. We use two measures to determine the locations of the separators and QSLs. An initial measure, typically referred to as the *norm*, provides a measure of the discontinuities using the gradients of the position variations between the two footpoints of the traced field line as shown below.

$$N_+^2(x,y) = [(\frac{\partial P_x}{\partial x})^2 + (\frac{\partial P_x}{\partial y})^2 + (\frac{\partial P_y}{\partial x})^2 + (\frac{\partial P_y}{\partial y})^2] \tag{5.3}$$

where P_x and P_y are the differences in x and y coordinates respectively for the two footpoints of each traced field line.

Titov et al. (2002) have improved upon the norm calculation to take into account conjugate footpoints while allowing for the two mapping regions to be of different sizes and shapes. The *squashing factor* Q is defined by:

$$Q(x,y) = \frac{N_+^2}{|det(D_+)|} \tag{5.4}$$

with D_+ defined as:

$$\begin{pmatrix} \frac{\partial P_x}{\partial x} & \frac{\partial P_x}{\partial y} \\ \frac{\partial P_y}{\partial x} & \frac{\partial P_y}{\partial y} \end{pmatrix} \tag{5.5}$$

Both the norm and the squashing factor are dimensionless quantities which increase significantly as the field approaches a discontinuity or a region of severe gradi-

ents in magnetic field. Field line mappings of Q and N show narrow regions of very high values providing the outlines of the QSLs within the coronal field map. These QSLs are generally very thin allowing for the significant build up of current sheets and the storage of magnetic energy in a strongly non-potential region of the corona prior to a reconnection event which will relax the non-potentiality to a lower energy equilibrium state. Therefore, comparing the observed hard X-ray signatures with the location of the corresponding QSLs provides direct insight into the nature of the energy release and current dissipation during solar flares.

5.2 Active Region 10720 and Our Selected events

The events for this study occur in NOAA active region 10720, a complex and flare productive active region which appeared on the solar disk from 11-20 January 2005. We chose this active region due to the magnetic complexity and numerous intense flare events detected as it evolved across the disk. Over this period, the active region produced five X-class events and 16 M-class events. The complete list of flares above GOES classification of M1.0 are presented in Table 5.1. Within the list of notable events, we are limited to flares for which we have both coverage in RHESSI for the full duration of hard X-ray emission, to track the hard X-ray evolution and vector magnetic field information which we obtain from the ground-based Huairou Solar Observing System (HSOS). These requirements restrict us to two events from 17 January 2005 shown in bold in Table 5.1.

Date	Begin	Max	Class
14 Jan 2005	1353	1411	M1.8
14 Jan 2005	1753	1757	M1.5
14 Jan 2005	2108	2126	M1.9
15 Jan 2005	0022	0043	X1.2/1B
15 Jan 2005	0409	0416	M1.3
15 Jan 2005	0426	0431	M8.4
15 Jan 2005	0554	0638	M8.6
15 Jan 2005	1141	1148	M1.2
15 Jan 2005	2201	2208	M1.0
15 Jan 2005	2225	2302	X2.6/3B
16 Jan 2005	2155	2203	M2.4
17 Jan 2005	0310	0321	**M2.6**
17 Jan 2005	0659	0952	**X3.8**
18 Jan 2005	1123	1132	M1.6
18 Jan 2005	1540	1549	M4.6
19 Jan 2005	0726	0813	M6.7
19 Jan 2005	0803	0822	X1.3
19 Jan 2005	1015	1023	M2.7
19 Jan 2005	1539	1539	M1.6
20 Jan 2005	0636	0701	X7.1/2B
21 Jan 2005	1010	1016	M1.7

Table 5.1 Large Flares Produced by Active Region 10720 from 14-21 January 2005

The two events we consider here, an M2.6 event peaking at 03:21UT and an X3.8 extended event peaking at 09:52UT, both originate along a complex, primarily east-west oriented, ribbon structure seen at UV wavelengths. The same extended UV ribbon system persists, extending across the complete active region, for the duration of both events; however, each of the X-ray flares occur in localized regions confined on opposite sides of the extended UV ribbon. The earlier M2.6 event shows X-ray emission appearing confined to the eastern half of the UV ribbons shown in the UV emission. The later, larger flare appear as a series of four localized kernels of HXR emission near the western edge of the ultraviolet emission ribbons. We will discuss the evolution of these sources for both events both from the context of the hard X-rays alone and in relation to the magnetic fields and currents in the corona in Section 5.3.1.

5.3 HXR Results for AR10720 Events

In terms of hard X-ray emission both of the events in this study appear as multiple impulsive burst events exhibiting two dominate bursts each. As expected, the HXR emission of the X3.8 event is a more intense. The M2.6 event, shown in Figure 5.1, has a clearly defined pair of impulsive bursts, each with a very sharp rise and then a gradual fall-off. Each burst lasts 2-3 minutes in duration. In terms of hard X-ray emission, these bursts can be seen as distinct flares as there is no discernible overlap, but rather a clear temporal separation between the two. The first impulse shows a steep rise near 03:13 UT followed by a sharp peak and a rapid fall off until 03:15:30

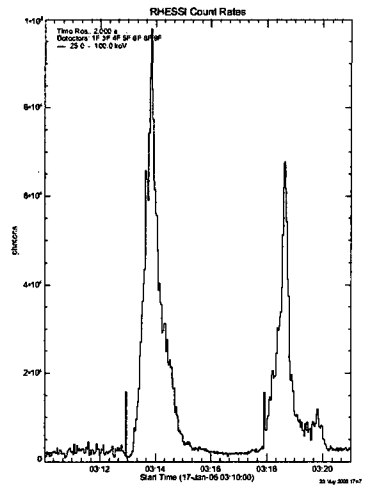

Figure 5.1 RHESSI 25-100keV hard X-ray profile for the M2.6 event from 17 January 2005. Hard X-ray activity persists from 03:13-03:21UT in two large impulsive bursts.

UT where the X-ray emission returns to a background level. The initial burst is markedly more intense than the later one. The second burst rises abruptly from this background beginning at 03:18 UT with a peak at 03:18:40 UT topping out at $\sim$ 70 percent of the intensity of the stronger primary impulse. A gradual fall off persists until 03:21 UT.

The second event, (see Figure 5.2) is a more complex multi-burst event with its 25-100keV X-ray emission lasting 22 minutes in duration. There is a small burst of precursor emission from 09:41:00-09:42:45. The most intense series of bursts in the X-rays begins at approximately 09:43 UT lasting until approximately 09:48 UT. This primary burst shows an extremely quick rise and an intense peak occurring at

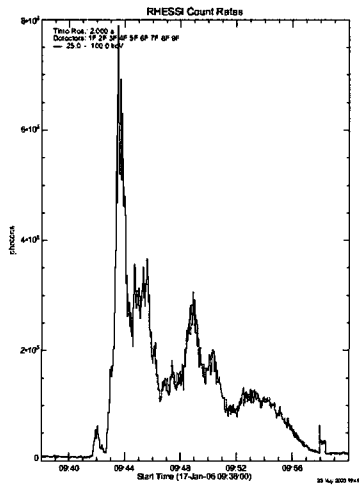

Figure 5.2 RHESSI 25-100keV hard X-ray profile for the X3.8 event from 17 January 2005.

approximately 09:44 UT with an equally quick fall off until $\sim$ 09:44:30. A second burst in this complex begins near 09:43:30 and rises to a plateau at approximately 45 percent of the maximum flux in the first intense peak. This secondary burst has a broader shape extending to 09:46:30 UT. A weak impulsive period from 09:48-09:52 UT shows two additional impulses in the HXR emission. The largest peak in this timeframe reaches 35 percent of the maximum emission at approximately 09:49 UT. This active period shows one more small burst between 09:49:30-09:51:00 UT but this impulse shows only a small rise relative to the apparent background levels.

These flares provide two significant cases for study of the X-ray evolution in comparison with the developing magnetic field. The bulk of this chapter will focus on the evolution of these X-ray sources through the duration of the event and its relationship

to the evolving magnetic field and the determined location of the separators and QSL determined from force free magnetic field extrapolations.

5.3.1 Hard X-ray Spatial Evolution

The temporal information discussed above provides general insight into the behavior of hard X-ray emission integrated over the whole region of flare emission. For the purposes of directly relating observed emission signatures to the magnetic development of the active region, the spatial distribution of discernible X-ray sources is of greater importance. To investigate this for the two events here, we generate a series of hard X-ray image reconstructions over the duration of each flare with 20 second integration times used to generate each image. The 20s integration time is necessary to ensure that the image reconstruction contains enough counts to converge to a solution. Using these images, we trace the hard X-ray evolution of sources seen in each of the impulsive bursts for both events. Figure 5.3 shows four panels of individual Pixon reconstructions from images near the burst peaks for the two flares, with the top panels showing hard X-ray emission from the peaks of the bursts within the M2.6 event at 03:13:40 and 03:18:40 UT, while the lower panels show peak hard X-ray emission of the larger X3.8 event at 09:43:20 and 09:48:20 respectively.

Over the course of the smaller event we see that hard X-ray emission progresses and expands into a number of localized kernels down a ribbon stretching to the south and east across the image field. The image from the initial most intense peak shows

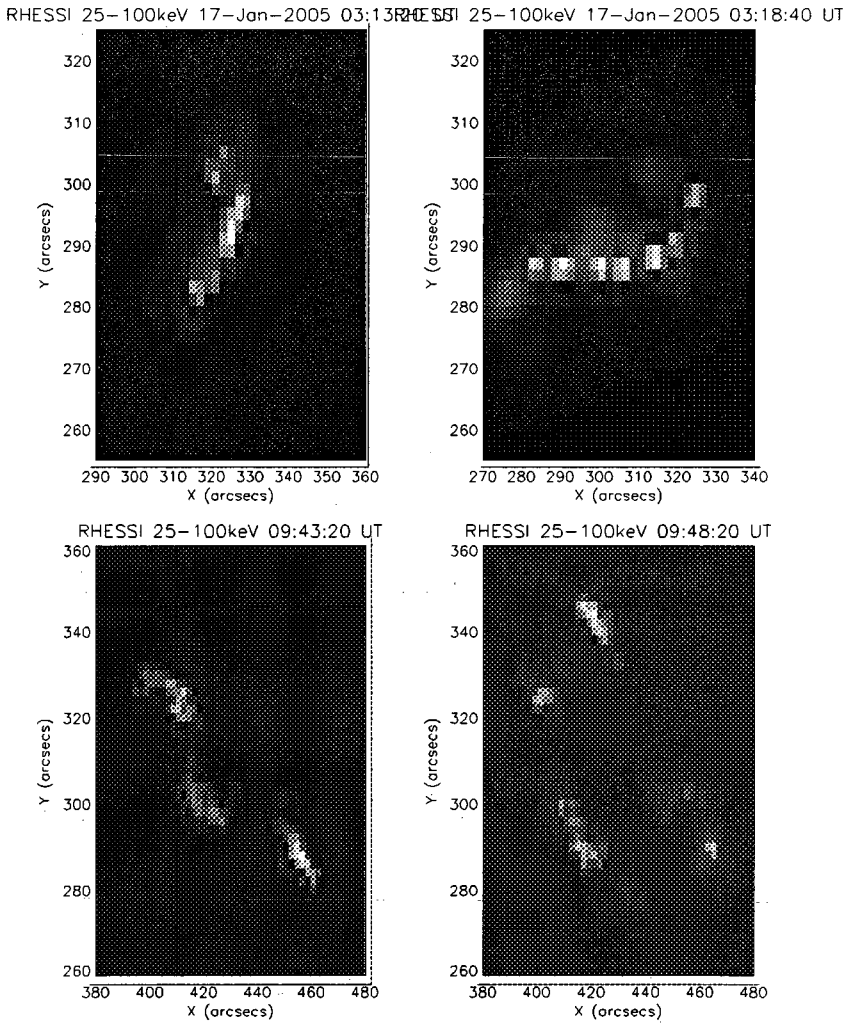

Figure 5.3 Four panels of RHESSI 25-100keV energy pixon reconstruction maps for the peaks of four bursts within the 2 flares studied here. The top 2 panel represent the peak images of the M2.6 event and the lower panel are similar peaks from the X3.8 event.

three confined X-ray sources to the north and center of the image field. Of the three sources, the central kernel and the source directly southwards show the strongest emission. These two sources persist and continue to contribute significant hard X-ray emission over the duration spanned by both of the main hard X-ray bursts; however, the emission in the later impulse is increased by the development of a series of smaller emission sources along a primarily eastward line from 315 to 275 arcseconds, relative to disk center in the x-direction. The evolution of these sources suggests a number of changes to the magnetic structure of the flaring region in the form newly developed sets of magnetic connections. The new magnetic structures allow for particle transport from the flare acceleration site in the corona into the chromosphere. The accelerated particles deposit energy when the reach the chromosphere producing the hard X-ray signatures observed.

The second event shows, over the course of the emission, four discernible localized sources. Three of the sources appear during the period of the initial burst group and persist through the weaker impulses later in the flare. The spatial development of this flare is as follows:

- The two southern sources show the most intense emission through the primary impulsive energy release and strong sustained emission throughout the flare.
- The upper left source appears during the primary energy release, but it is markedly weaker in total flux than its two southern counterparts.

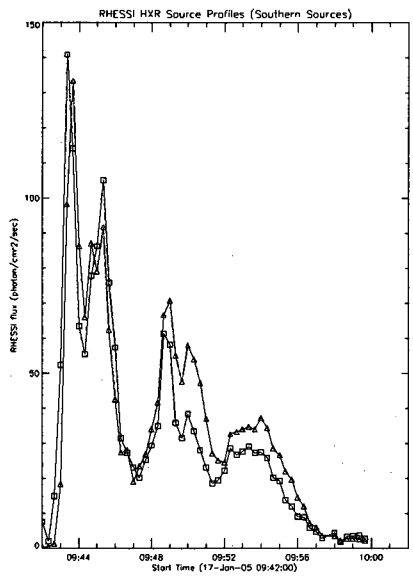

Figure 5.4 Comparative imaged HXR emission temporal profile for the southern sources visible in the X3.8 events. These sources show strong, consistent emission throughout the impulsive bursts of the event. The temporal evolution also show significant evidence of footpoint conjugacy (Correlation Coefficient of 0.918).

- The second burst shows all four sources active at the peak with the source to the upper right only appearing during this time frame.

In the particular case of the X3.8 event, the locations and the persistence of some of the X-ray kernels are visually suggestive of the existence of strong magnetic connections between some of the sources. A mechanism for testing these connections, based solely upon the HXR data, is to analyze the imaged temporal profiles for signs of conjugacy. Conjugate footpoints are emission sources which serves as chromospheric footpoints for opposite ends of the same magnetic structure. These sources, being

magnetically connected, will show similar temporal evolution and response to particle acceleration and energy release within the loop. To obtain this light curve we use the peak HXR images shown in Figure 5.3 to determine the locations and areas of source kernels. We enclose each of the source areas and determine the total X-ray flux within these areas for each image. We then use these flux measurements to generate a time series for each image in our series. Figure 5.4 shows the imaged emission profiles for the two southern sources for the X3.8 event. Of the two sources, the eastern source,shown with triangles, exhibits the strongest total emission. The western footpoint of the loop shows the strongest flux at the initial peak but the fluxes of both these sources are quite similar throughout. A correlation analysis of the two sources shows a strong temporal correlation (R=0.918) indicating that these two sources are well-connected conjugate footpoints linked by a single magnetic that has been energized by the flare energy release.

The two northern sources do not show any significant correlation over the course of the flare, primarily because the upper right source does not become appreciably active until the later, weaker burst of activity. However, during this later burst, the northern sources do show similar time profiles suggesting that during this weaker activity, these sources show evidence of a temporal association and thus are likely magnetically connected. This again suggests that these sources are connected to the same energy release site and their emission is a response to the same physical

processes. Such connections provide insight into the structure of the magnetic field and the location and timing of energy release within the corona.

5.3.2 Ultraviolet, Hard X-ray and Magnetic Field Relationship

Having discussed the X-ray development of the two flares in this study, we now relate the observed X-ray emission to observations in the UV and measurements of the magnetic field to obtain a more complete picture of the link between flare emission and the magnetic complexity of the flaring region. To this end, we discuss the development of the hard X-ray emission sources relative to the chromospheric ribbon structures in the UV as well as the magnetic structure within the chromosphere. These chromospheric relationships provide a base from which we then expand to investigate the connection between chromospheric emission and the development of QSL structures in the corona.

The M2.6 Event of 17 January 2005

The smaller of our two events shows a complex ribbon system with two primary ribbons and a series of apparent connections between them. The clearest ribbon extends nearly 200 arcseconds in east-west extent (from 225 to 425 from disk center) and approximately 50 arcseconds in north-south extent (from 240 to 290 arcseconds from disk center). The second clearly defined ribbon is located in the northern part of the active region, ranging from 310 to 350 arcseconds in the y-direction and from

approximately 290 to 380 arcseconds in the x-direction with all coordinates relative to disk center. The X-ray sources primarily lie along the eastern half of the lower UV ribbon. This location appears consistent with the location of the magnetic neutral line which runs along the boundaries of the positive and negative polarities. Figure 5.5 shows these overlay plots for both the significant bursts of activity in the early event.

The first image focuses on the time range 03:13:00 to 03:15:00 UT, showing the development of the x-ray centroids over time. The color used depicts the earliest times in blue progressing to red for later times. The lower image shows the X-ray progression from 03:17:20 to 03:19:20. HXR sources in the later frame comprise a series of strong emission kernels forming an east-west aligned line of emission extending from approximately 275 to 325 arcseconds from disk center in the x-direction. Each of these sources appears as a chromospheric source in a region of the same magnetic polarity. The numerous sources located along a clearly visible ribbon structure is consistent with the standard flare picture of a developing arcade. However, the footpoints in the opposite polarity region are not evident in the hard X-ray observations. This observation suggests that high energy electrons responsible for the hard X-ray emission may be preferentially contained within one leg of the magnetic loop. while higher energy particles, capable of producing UV emission but not hard X-rays are contained in the other leg. This scenario suggest that the particle acceleration mech-

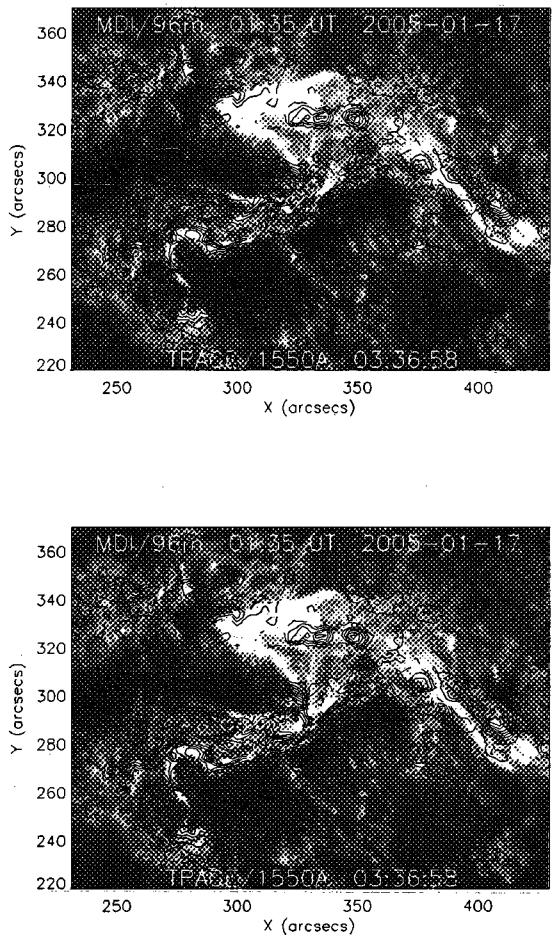

Figure 5.5 HXR sources overlaid on a TRACE UV 1550 Å context image with contours of positive and negative polarity found from the MDI 96 minute cadence magnetogram (positive polarities shown in green negative in orange). (a)03:13 to 03:15 UT; (b) 03:17:20 to 03:19:20. The HXR images are produced at 10-second resolution. The color table for the HXR emission is color table 5 which show early times as blue, intermediate times as red and orange, and later times as yellow. The data in the overlays for all instruments have been differentially rotated to the TRACE image time.

anism must have some degree of energy dependence. The specifics of this mechanism are unknown; however, one possible mechanism involves a magnetic trapping scenario with an energy-dependent pitch angle distribution as discussed in McClements and Alexander (2005) and Alexander and Metcalf (2002).

In addition to the shape of the hard X-ray distribution, we use the image reconstructions from RHESSI to determine the flux-weighted centroid for each hard X-ray source. This provides a clearer picture of the evolution of the X-ray flux than that provided by the sources themselves. This is accomplished by selecting the hard X-ray sources via the polygon method as described in the previous chapters. Within each polygon we calculate the X-ray flux and use the x and y positions to determined the centroid for each image in the X-ray sequence. The centroid positions are differentially rotated to the time of the TRACE context image in order to provide a direct comparison with the TRACE data and the magnetic development. The rotation of each image is performed specifically to eliminate the differential rotation from the source motion, leaving any apparent motion observed to be the shift in the actual centroid for each of the given sources. The centroids are overplotted on the UV ribbons and the line of sight photospheric magnetic field contours for direct comparison (see Figure 5.6). Within the figure the centroids are shown changing with time by a sliding color scale with earlier times in blue and later times shown in yellow.

The course of the M2.6 event followed in Figure 5.6 shows the development of six

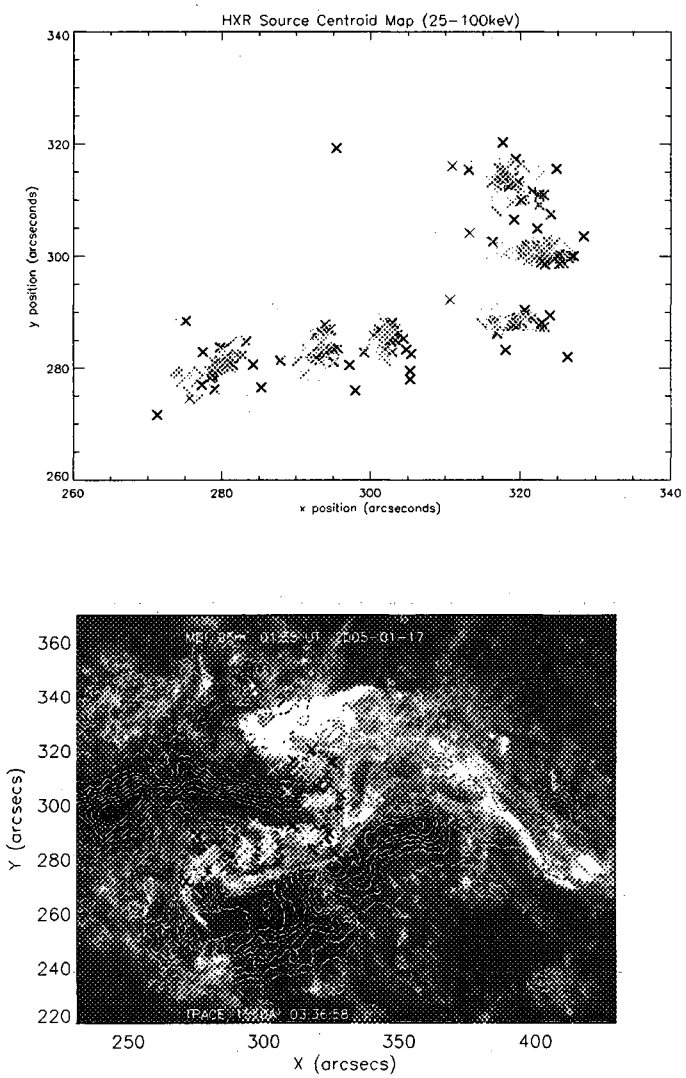

Figure 5.6 Shown at top is a centroid map for the discernible localized sources for the M 2.6 event. The centroids are calculated from 10 second integrations of 25-100 keV energies in the RHESSI images. The source region were selected from the RHESSI image at 03:18:40 UT. Differential rotation and TRACE co-alignment have been taken into account by differentially rotating the data to the TRACE context image time.

isolated emission sources existing primarily co-spatial with the eastern portion of the complex UV ribbon system. The UV ribbon system is largely comprised of two well-defined horizontally oriented ribbons, as described earlier, with notable connections visible between them. The first two sources observed develop along a north-south connection between the two main east-west oriented ribbons. These sources are noticeably visible primarily during the first emission burst from 03:13-03:15 UT. These two sources generally only show a slight eastward drift, though the centroid for the earlier times are more easily defined because of source visibility. Four of the six sources that appear to evolve with generally eastward motion along the southern ribbon. These sources appear most evident during the later bursts of activity, along and near the southern UV ribbon. They remain reasonably stable along the ribbon with only a slight eastward drift.

Large opposite polarity regions of magnetic field, shown as orange and green contours in Figure 5.6, are evident in the region near the UV ribbon and HXR sources described with a long a well-defined neutral line marking the region of X-ray and UV emission. In most flare models, reconnection is believed to occur in the corona above existing chromospheric neutral lines. The chromospheric hard X-ray signatures and the observed magnetic structures indicate that the HXR kernels are the result of one of more reconnection events consistent with the standard flare emission picture. To clarify the magnetic structure throughout the corona and its relationship to the

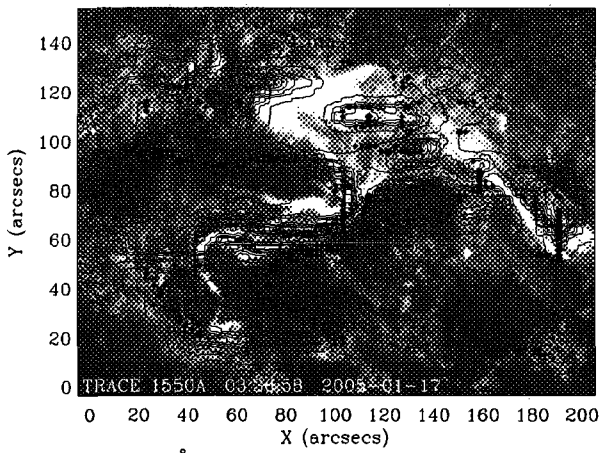

Figure 5.7 TRACE 1550 Å context image with overlaid contours of Huairou vector magnetogram data with positive polarity shown in yellow and negative in blue from 03:51 UT. The orange symbols indicate the locations of QSLs from the analysis described in Tian, Alexander, and Coyner (2008). Each symbol indicates a Q of greater than 100 with larger symbols corresponding to larger Q.

emission seen, we compare the emission source and magnetic structure locations to the locations of the QSLs in the corona defined through the force-free field extrapolations.

Figure 5.7 shows the combination of the TRACE 1550 Å context image with contours shown from the Huairou vector magnetogram data. In addition the circular symbols represent points in the corona where the squashing factor Q has a value greater than 100. As discussed earlier, regions of high Q, indicate significant gradients in the coronal field and are stronger observational evidence of QSLs and by extension sites of probable magnetic reconnection events within the corona. Based upon the Huairou data taken just after the flare at 03:51 UT, a long region of high Q is found along the lower UV ribbon consistent with the positions of the HXR emission kernels.

This region represents an extended QSL in the corona, five arcseconds above the photosphere, lying above the southern portion of the active region. The existence of a QSL along the active flaring region alongside the chromospheric hard X-ray signatures suggests that these sources are the result of particle acceleration and energy release at the QSL.

The results we show here illustrate a consistent picture of the chromospheric response being a direct results of relaxation within the coronal field due to one or more reconnections. In this M 2.6 event, however, we do not see significant X-ray evolution over the duration of the flare because many of the sources show activity in localized stationary sources. We will further discuss the evolutionary aspects in the context of the X3.8 event in the next section.

The X3.8 Event of 17 January 2005

The X3.8 flare actually shows flare development in the UV from 06:54 UT lasting over three hours in duration. While the majority of the event is seen in 1600 Å emission, data gaps exist in the TRACE images between 09:20 to 09:55 UT limiting our discussion here to only the hard X-ray emission. The hard X-ray emission occurs from 09:42 to 10:00 UT. While the TRACE 1550Å context image from 08:36 UT shows a similar UV ribbon structure to the M2.6 flare, the flare emission in the second event is localized to regions on the western side of the active region. The hard X-ray emission arises in the form of four discernible source kernels within a 70x70

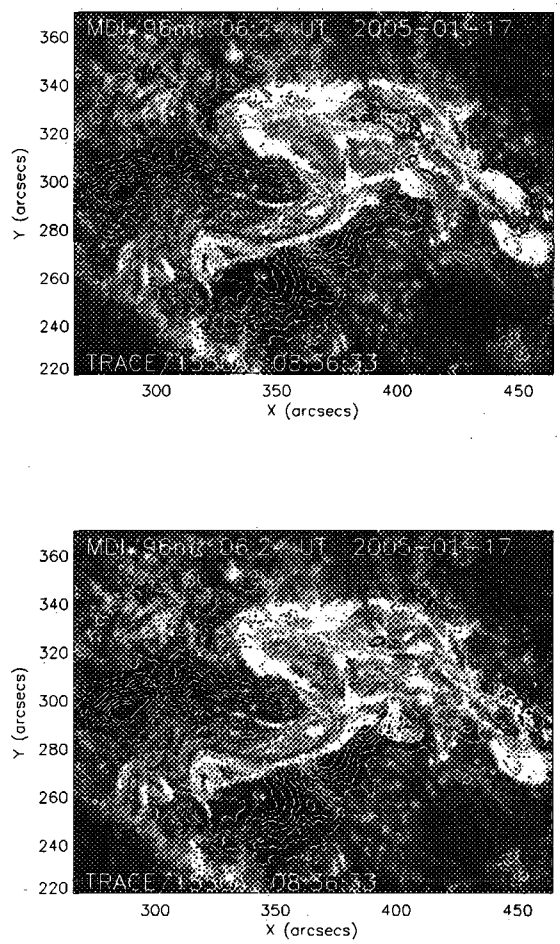

Figure 5.8 HXR sources for the X3.8 event overlaid on a TRACE 1550Å context image from 08:36 UT. MDI 96 minute cadence contours are shown from a magnetogram at 06:24 UT. (top) Image showing the HXR progression from 09:42:00 to 09:46:20. (bottom) Image showing the X-ray progression from 09:47:00 to 09:51:20. Each image results from a 20 second resolution image reconstruction. The color table for the HXR sources shows early times in blue, intermediate times in red and orange, and later times in yellow.

arcseconds-squared region covering from 390 to 460 arcseconds from disk center in the x-direction and 280 to 350 arcseconds from disk center in the y-direction. For the time ranges illustrated in Figure 5.8, we see, initially, the evolution of three isolated X-ray sources in the top figure each occurring in a localized magnetic field regions of mixed polarity. The X-ray source to the south and west exists in a region of negative polarity (shown in green). The two remaining sources are each found to be in regions of positive polarity (seen in orange). The temporal development, shown earlier in Figure 5.4, demonstrates a strong correlation and provides a direct link between two southern sources. This may indicate a direct magnetic connection or may be the result of two distinct sources responding simultaneously to the same energization. Either scenario provides critical insight into the magnetic structure and energetic development of the flaring region. Evidence of a connection to the active northern source at early images is not as convincing.

In the lower image of Figure 5.8, we see hard X-ray emission from 09:47 to 09:51:20 UT exist in four well defined kernels. The three kernels from the prior sequence persist through the latter times with the same 70x70 field as discussed for the earlier flare burst. The fourth source appears only during this second burst of activity and is located along a small patch of negative polarity field in the northwest portion of the flaring region. The four sources appear to form significant magnetic connections between the respective northern and southern pairs. These connections

would lend themselves to less complex loop structures which would be consistent with magnetic complexity and free energy being removed from the system during the initial intense burst beginning at 09:42 discussed above. As expected from the temporal analysis, the strongest and most well-defined sources throughout the X-ray activity are the southern kernels. Each of these sources remains extended and well-defined throughout the flare. In contrast the northern sources both fade earlier in the X-ray evolution.

In Figure 5.9, the southern pair of HXR sources shows a significant progression in the spatial location of their respective centroids over the lifetime of the flare. Both these sources show an initial shift with the western footpoint drifting an appreciable 20 arcsecond northwards over the first 6-7 minutes of the flare activity. In contrast, its counterpart shows a less dramatic but notable southward drift of just under 10 arcseconds during this initial period. Later in the flare event, these sources show a tendency to separate, expanding the spatial extent of the HXR flare emission horizontally. This expansion is consistent with footpoint motions resulting from an expanding and rising loop as the flare evolves. We see similar evidence of drifting and separation in the northern sources. The timing and spatial development of sources support the standard picture of each localized region of HXRs being a direct result of particle acceleration and energy deposition along loops resulting from an initial reconnection within the corona. In order to better clarify where reconnection is most

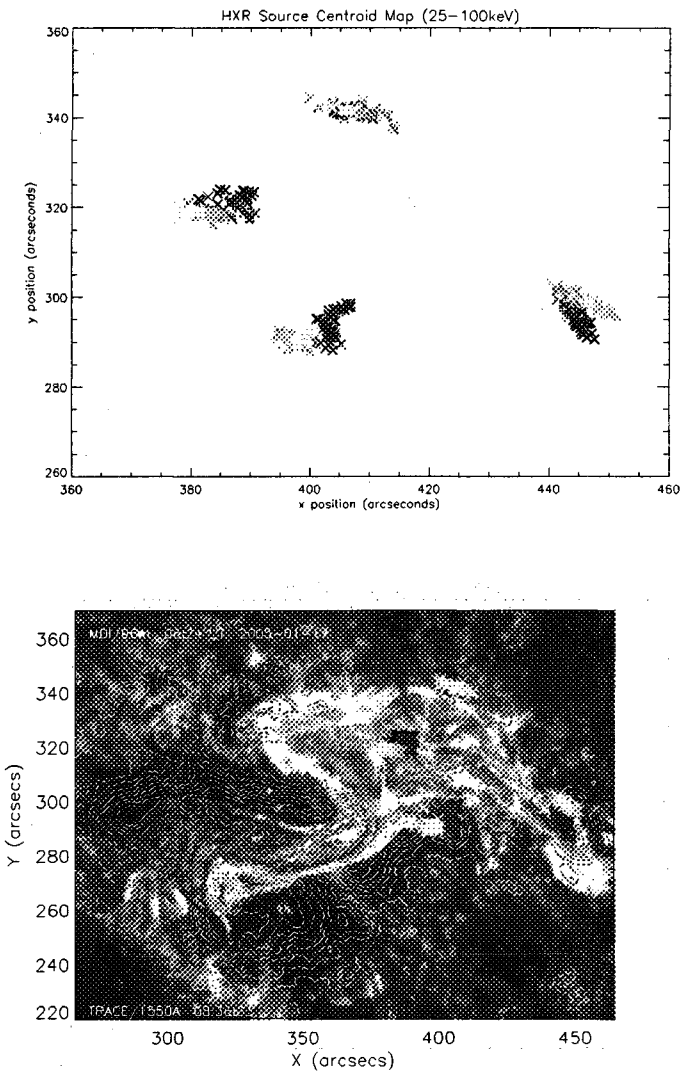

Figure 5.9 the position of the HXR centroid for the four sources at 10 second interval from 09:42:00-10:00:00. Earlier times are shown in black/blue, intermediate times are shown in red/orange, and the later times are in yellow. Differential rotation and TRACE co-alignment have been taken into account.

likely in this event we again rely on comparison of the HXR spatial distributions with the determined locations of QSLs over this western flare region.

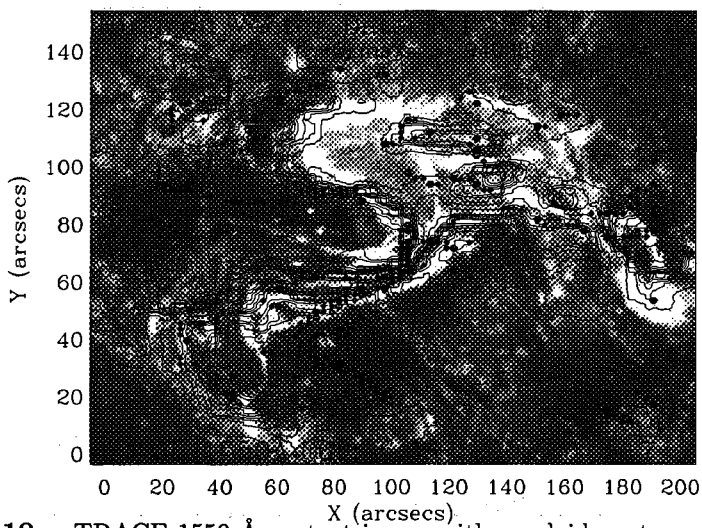

Figure 5.10 TRACE 1550 Å context image with overlaid contours of Huairou vector magnetogram data with positive polarity shown in yellow and negative in blue from 06:11 UT with the orange circles representing regions of high Q within the magnetic field in the corona of the flaring region.

For further exploration of the relationship in this event between the HXR sources and the flaring region topology, we again must compare our observations of X-ray to the extrapolated coronal field to more accurately describe the flare evolution in the context of the governing field. Specifically in this event we find that each of the four well-defined sources exist in clear regions of consistent magnetic polarity. Unlike the previous event, these magnetic polarity regions are much smaller and less extensively connected than the prior event. Within this western flaring region, we find evidence of magnetic neutral lines corresponding spatially to visible UV emission shown in the

TRACE context image. Around each of these neutral lines, we find regions of high squashing factor showing clear signs of a developing QSLs for both sets of emission sources, particularly evident between the two southern sources of emission. Direct comparison of QSL mappings from Figures 5.7 and 5.10 shows the development of strong but spatially limited QSL appearing in the later magnetic data covering an area of approximately 30"x 10" centered near [425,300] arcseconds from disk center. This QSL corresponds to the likely location of a coronal magnetic loop with footpoints corresponding to the enhanced emission kernels seen in this region in hard X-rays. The presence of a QSL provides evidence of a structural magnetic connection linking the two strong X-ray sources. Démoulin et al. ((1997) describe QSLs as locations for energy release and particle acceleration within flares which show chromospheric footpoints on either side; therefore, the QSL indicates the energy release and particle acceleration site. Energy release and particle acceleration at QSLs arise naturally from the QSLs being likely locations of magnetic reconnection in the corona.

In the case of the northern pair of sources we find evidence in the photospheric magnetic data of a smaller neutral line lying between the sources, supporting the probable connection between these two sources with the two emission kernels being footpoints of a weak X-ray loop in this northern region. From the perspective of QSLs, however, there are only a limited number of points in the region near the northern source pair with $Q > 100$, suggesting that, while there are still points of

strong discontinuity in this region, they appear sporadic and isolated. This indicates that a developing QSL in this region is weaker and less defined than those previously detected. It is also plausible that the weaker QSL would correspond to the weaker X-ray emission as the buildup and subsequent dissipation of magnetic free energy is more prevalent at stronger discontinuities.

5.4 Conclusions

In the preceding section, we addressed the evolution of the coronal magnetic field field for the complex NOAA active region 10720 through both the evolution of chromospheric hard X-ray emission signatures as an observational diagnostic of magnetic field evolution as well as the analysis of force-free coronal field explorations. Specifically in the flares we observed, we find several common traits. In both events, we find the hard X-ray emission develops in multiple sources largely in smaller spatially-confined regions. These groups of sources evolve with new sources emerging in regions where magnetic connections are readily available. When the field is extrapolated to the corona, we find these areas of hard X-ray emission to generally lie near a defined QSL with squashing factor parameter, Q, of greater than 100.

The individual events evolve differently; however, they both require that a magnetic connection exist between the corona and regions of hard X-ray emission. The first event contains a series of largely stationary sources developing nearly co-spatially with a strong QSL and remain largely stationary with time. The larger event, shows

four HXR sources spread over a greater spatial extent and with each of the sources showing significant mobility over the course of the event. The four sources of the X3.8 event develop as 2 sets of conjugate footpoints, with the southern pair developing and the stronger pair showing consistent emission throughout the duration of the flare. The northern developing pair is weaker in X-ray emission and does not persist throughout the event but only appears late in the flare. This indicates that the magnetic structure of the flaring region is evolving and and a new magnetic connection develops in the later stages. In relation to the QSLs, we find, through comparison of Figures 5.7 and 5.10, a developing QSL appearing within the region connecting the two southern sources. This QSL seemingly outlines a connection between the two sources consistent with the expanding rising loop picture. The northern pair of weaker sources, only demonstrating the conjugate emission later in the event, shows a weak developing QSL with seemingly sparse regions of $Q > 100$.

The observations strongly suggest a link between the hard X-ray sources and the presence of a QSL. This provides observational confirmation of these QSLs being significant locations for magnetic reconnection in the corona. This connection was theoretically expected in part due to the build up of currents and thus magnetic energy in the corona near QSLs. HXR emission has also been shown to result from the interaction of accelerated particles with the chromosphere following reconnection in the corona. Therefore, the results seen here indicate that the hard X-ray emission

sources can likely be used as chromospheric emission diagnostics for the magnetic structure of the corona.

Chapter 6
Relating Solar Magnetic Configurations and Flare Activity to Observed SEP Compositional Data

While the work discussed in earlier chapters focuses on flares and their interaction with the solar environment, these solar transient events also have a clear impact on the interplanetary environment and the Earth itself. Therefore, a critical component of attaining a complete understanding of solar transients requires knowledge of the mechanisms and means the govern how these energetic phenomena interact and influence the inner heliospheric environment, within 1 AU. This involves an understanding of the structure and state of large-scale magnetic environment in which the solar transient originates. In this chapter, we concentrate on large flare/CME events that result in the production of fast moving ions with energies as high as 100 MeV/nucleon, as observed by spacecraft near 1 AU, either at the L1 Lagrange point or in orbit around the Earth. These Solar Energetic Particle events (or SEPs) are some of the most dangerous Space Weather hazards to astronauts, satellite and other space-based equipment. The focus of our research has been on the investigation of the relationships between the pre-event solar conditions and the observed properties of the solar energetic particles. The discussion of the role of solar environmental conditions in influencing the observed SEP characteristics arises from an initial discussion of two 2002 SEP events, from 21 April and 24 August respectively, investigated as campaign

events at the SHINE 2004 workshop*. Both of the events are associated with intense X-class flares occurring on the west limb of the Sun. The flares themselves appear very similar when viewed in the EUV with TRACE (depicted in Figure 6.1). Despite similar flare strengths and locations, the two events produced widely varying results from a particle point of view at 1 AU. As briefly discussed in Section 2.3.2, the particle population analysis for these two events, using the instruments aboard ACE, have shown significant divergence in the observed abundance ratios of key elements in the event particle populations. Given that SEPs, in these large events, are accelerated by a shock forming some distance from the Sun, due to the interaction of a fast-moving CME and the solar wind (see Chapter 2), and then transported along interplanetary magnetic field to 1 AU, directly relating the observed particle properties to specific conditions within the solar environment has proven to be a daunting challenge, though attempts have been made using RHESSI X-ray observations (Lin, 2005; Krucker et al., 2005). The research in this chapter attempts to determine if there are any discriminating features in the solar environment that point to an explanation of the marked differences in particle composition between the 2002 April 21 and 2002 August 24 events. To this end, we investigate the variations in the solar activity leading up to these flares, and others associated with large gradual SEP events, to ascertain the importance of these solar conditions in shaping the pre-event

*$http://cdaw.gsfc.nasa.gov/SHINE_Campaign/20020421/$

environment and influencing the resulting particle distributions seen near Earth.

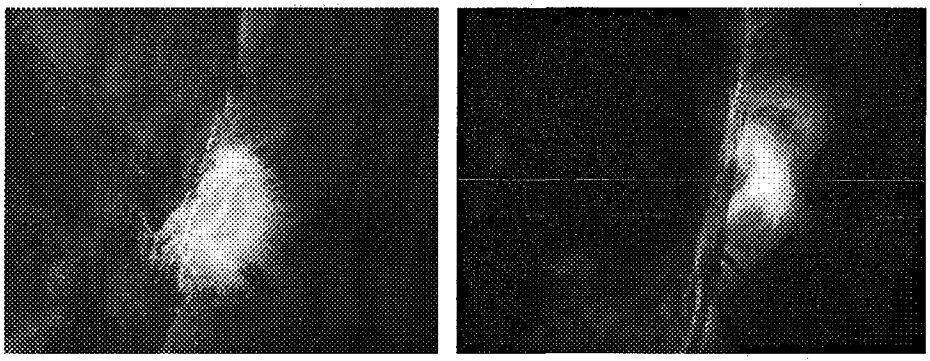

Figure 6.1 Flare arcades taken from the X-class flares on 21 April 2002 and 24 Aug 2002 respectively for visual comparison. Data shown is taken from TRACE 195Å observations.

In studies for the 2004 SHINE campaign on these events, our group investigated the solar pre-history for each of these events focusing on such as aspects as coronal variations, flare and CME productivity and and magnetic field development. The active regions associated with the two events showed drastic differences in both coronal magnetic structure, as determined from PFSS extrapolations (see Section 3.3.2, and in activity history leading up to the major events, suggesting these variations as plausible solar activity contributions to the significantly varied particle populations observed (Liu et al. 2004; Alexander et al. , 2004).

Using this two-event comparison as a starting point, we present in this chapter the results of an extended analysis of the role of solar magnetic field connectivity and flare productivity on the observed abundance ratios for heavy elements observed

by ACE for a large sample of large gradual solar energetic particle events (LSEP). The LSEP events we analyze here are initially taken from three event lists, each having significant overlap (Desai et al., 2006; Cane et al., 2006; Tylka et al., 2005, 2006) with the events selected in each case initially on the basis of their high proton fluences observed by GOES. These events, which are believed to be the result of shock acceleration, are generally expected to accelerate all available particles in the path of the shock; therefore, variations in the observed compositions are indicative of a variation in the seed population of particles for any given event. The exact driver for these event-to-event variations remains unclear; however, here, we investigate two potential contributors from the pre-event solar environment.

6.1 Event Selection and Available Particle Data

In the three LSEP studies referenced in the previous section, many of the events overlap as they were all selected primarily due to their high GOES proton counts; however, we consider each event list separately to include the unique events for each data set independently. The data tables for the three LSEP studies are included for reference in Appendix A. Of the data collected, we pay particular attention to the iron and oxygen abundances, specifically their ratio, for each of the three energy ranges studied (0.32-045 MeV/nuc, 30-40 MeV/nuc, and 25-80 MeV/nuc). For our solar environment study, we limit the events considered to only include those where an Fe/O ratio can be determined, and the SEP event can be traced to a specific active

region. Fe/O ratios provide the common parameter reported in all three particle studies and is often used to discuss heavy element composition in SEP studies. In the low-energy study of Desai et al. (2006), a total of 64 LSEP events were studied from 1997 November to 2005 January, covering a range of associated flare importance from C2 to X28. We calculate the active region open field magnetic fluxes for 58 of the 64 because these 58 events have calculable Fe/O ratios in the 0.32-0.45 MeV/nuc energy range. For the Tylka et al. and Cane et al. events, we calculate the open fluxes for 55, and 87 of the listed events for each study respectively.

For each of the events where abundance data is available, we then perform localized PFSS extrapolations, and determine the field configuration for the event associated active region. From this field configuration, we determine the total open field magnetic flux for each event based on extrapolations near the time of the flare and CME. This provides a quantitative measure of potential access for the particles to interplanetary space. Only those flares which can inject particle onto open field can generate energetic particle populations high in the corona. The specific details of our magnetic analysis will be described in Section 6.2 In addition, using the GOES flare history, we determine the flare index for the given active region for the events where both particle abundances were available and a specific active region could be determined. A full explanation of the flare productivity calculations can be found in Section 6.3.

6.2 PFSS Extrapolation and the Determination of Available Open Magnetic Flux

For each of the events studied here, we are able to isolate the active region associated with the associated flare and CME responsible for the LSEP event. In order to determine the magnetic structure, we then use the pfss_viewer procedure (DeRosa, Freeland, and Schrijver, 2004), from the Solarsoft IDL package, based on the PFSS model detailed by Schrijver and DeRosa (2003). For each event, we select the magnetogram from the nearest available time to the time of the flare. For each day the procedure uses four MDI magnetograms at a cadence of every 6 hours (The times of the magnetograms used are 00:04, 06:04, 12:04 and 18:04 UT each day.). Due to the cadence of the magnetograms and the desire to obtain the pre-event magnetic configuration, the closest magnetogram in time preceding the event is selected to define the photospheric boundary condition for the magnetic field. We select the active region using a user-defined region of interest. For our extrapolations, we used 400 field lines to ensure full magnetic coverage of the active region. Additional tests were run using more field lines within the active region; however, no appreciable variation in the field configuration occurred with the addition of the extrs lines. Two examples of the resulting 3D coronal field are shown in Figures 6.2 and 6.3.

Figure 6.2 shows the result of the 400-line field extrapolation for AR 9906 associated with the SEP event of 21 April 2002. The field for AR 9906 show a large central

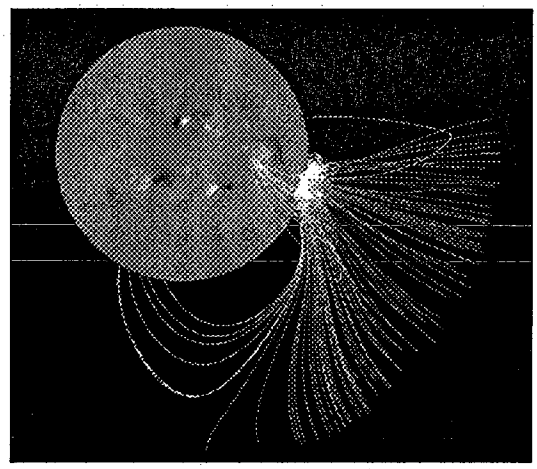

Figure 6.2 An example image of our PFSS extrapolations from 2002 April 21 showing large region of open field (pink lines) and closed field loop (white) prior to the 21 April 2002 event based on the MDI magnetogram at 00:04 UT.

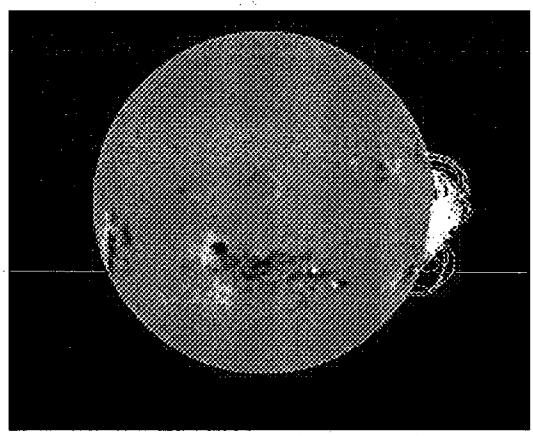

Figure 6.3 An image of our PFSS extrapolation results from 2002 August 24 showing the completely closed active region AR 10069 associated with the 24 August 2002 event based on the MDI magnetogram at 00:04 UT. The closed field loops generally stay confined to regions near the surface.

region of open field, shown in the figure as a collection of pink field lines extending to the source surface boundary at 2.5 solar radii. Around this central region, we find a number of smaller scale closed loops shown in white. Many of the closed loops near the active region remain tightly confined to the low corona. However, there are a few closed loops which connect active region 9906 to other active regions on the solar disk and appear to reach significant heights in the corona although they remain below 2.5 radii and thus remain closed.

For cases of open field, we calculate the available open field flux. The open field provides a pathway for particles to propagate away from the Sun. Any flare particles that are injected onto these open field lines will travel at much higher speed than the ambient solar wind particles; therefore, access to open field will likely limit the contribution of remnant flare particles to the shock-acceleration seed population as these particles will have left the corona prior to any shock formation. Within the PFSS procedure we use, four maps of data are collected: a map of the field line positions and maps of the three field components. To obtain the area for the open field region, the map of the field positions gives the location of the open field, designated as 1 or -1, depending on polarity. The open field line locations identified mark the boundaries of the open field region, allowing us to use a user-defined polygon region of interest to select the full area of the open field. The active region flux is then calculated using the area of the selected open field lines and the magnetic field through each

area. Because the maps of field line position and field values have been made in Carrington Map coordinates, each pixel within the map has an area weighting factor to take into account the conversion from rectangular to spherical coordinates in the area calculation. The flux calculation for each pixel is given by:

$$\Phi = \sqrt{\left(\frac{w * B_{rad}}{\overline{w}}\right)^2} \times 10^{18}, Maxwells(Mx) \tag{6.1}$$

where B_{rad} is the radial field through the area, w is the specific weight for the given pixel, and $\overline{w}$ is the mean of the weighting factors (DeRosa, 2006, private communication). The fluxes for the individual pixels within the area are then summed to produce the total open flux for each region. Within our events, for those showing open field, we find open field fluxes of order 10^{19}-10^{23} Mx. Typical active regions have total fluxes of order 10^{22} 10^{23} Mx (Zhang et al., 2007) with the largest active regions have fluxes of order 10^{25} Mx (Choudhary et al., 2002).

For a number of our events, however, we find active region with no evidence of any open flux. For these regions, magnetic structures largely consist of tightly confined loops in the low corona covering the active region (see Figure 6.3). Longer closed loops exist connecting the event-associated active region to other neighboring active regions, but all of these loops remain near the solar surface. Although these events cannot be directly included in the study of the influence of open field on composition results, these closed field events provide, a means of qualitative comparison with the open field events on the whole. These comparisons will be discussed fully in Section

6.4.1. It should be noted that PFSS models are designed to provide a reasonable approximation of the large-scale coronal magnetic field without implementing full MHD. It cannot reproduce the small-scale magnetic structure during the flare, as flares by definition are non-potential. This means we cannot say much about the specific mechanisms relating particle production at the Sun to those observed at 1 AU. We can, however, reasonably approximate the large-scale connectivity, giving a reasonable representation of the flux distribution.

6.3 Quantifying Flare Productivity

Many SEP events originate in complex active regions responsible for numerous flare and CME events over their lifetime on the solar disk. The recent importance of remnant flare suprathermals in shaping the population of particles accelerated by gradual SEP events (Mason et al., 2004) suggest that active regions which are more productive could significantly influence the existence and strength of a flare suprathermal component. Initially used to quantify activity for the entire lifetime of the active region, the flare index calculation takes into account the peak soft X-ray flux from GOES measurements (1-8 Å) using the flare classification on a logarithmic scale to produce a numeric measurement of activity (Antalova, 1996). This index gives significant influence to those active regions which produce large X-class flares. We repeat the formula from Chapter 3 here for convenience:

$$A = (100S^X + 10S^M + 1.0S^C + 0.1S^B)/\tau \quad (6.2)$$

Our study of flare productivity makes two important departures from the original flare index calculations. Instead of focusing on the full lifetime of the active region, as was done by Abramenko (2005), we focus only on the lifetime up to the time the SEP event, as flares occurring days after the event would not plausibly influence the particle seed population relevant to the SEP events. In addition, in cases of multiple events for a given active region, we include only the flares and CMEs between the times of the specific SEP events. This makes the plausible assumption that the SEP event clears the flare particle seed population by accelerating them to SEP energies. Testing the validity of this index, we find that the highest value in our study is attributed to AR 10486, the active region responsible for the intense Halloween 2003 events involving four very intense X-class flares within the span of seven days. Further analysis of our flare productivity results appears in Section 6.4.3.

6.4 Results and Discussion

In this section we present our findings and discussion of the influences of solar environment conditions on the resulting SEP compositions measured in-situ with ACE. Our analysis is discussed in three parts:

- Noting the existence of both open and closed field events based on the 21 April

2002 and 24 August 2002 events, we statistically compare the occurrence frequency with observed SEP composition ratios (Fe/O) to determine characteristic differences, if any, between the observed particle populations for the two categories of events.

- We then analyze the relationship, for open field events, between open field flux and the composition ratio.

- Finally, we present a study of the SEP composition and the implications of active region activity.

6.4.1 Comparing Open and Closed Field Events

In the original analysis of Liu et al. (2004) and Alexander et al. (2004), a striking difference between the 21 April 2002 and 24 August 2002 events was that the August event appeared completely closed magnetically, from results using PFSS extrapolations. As one of the clearest differences between the two events, we analyze the frequency of occurrence of these closed field events and their implications for particle populations at the various energies. We include a breakdown of open and closed events at each energy range in Table 6.1.

For the low energy data from ULEIS (Desai et al. 2006),we are able to identify active regions associated with 58 events where we also have composition data. Of those events we find 40 that show evidence of regions of open field while 18 events

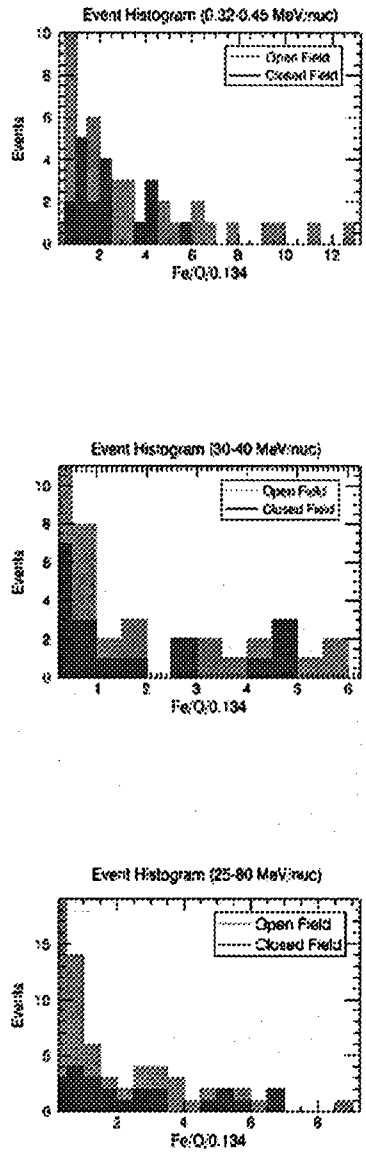

Figure 6.4 Open and closed field comparative histograms for each of the three energy ranges (0.32-0.45 MeV/nuc, 30-40 MeV/nuc, 25-80 MeV/nuc)

Energy (MeV/nuc)	# of Events	Open *	Closed	Closed %
0.32-0.45	58	40	18	31.0
30-40	55	37	18	32.7
25-80	87	64	23	26.4

Table 6.1 Table of closed configuration and open configuration occurrences for each energy range. Open field events refers to active regions with any discernible open field.

were completely closed. Figure 6.4 (top) shows the respective distributions of the Fe/O composition ratio. For the open field configuration events, hereafter OCEs in the low energy range we find a strongly peaked distribution between 0.5-1.0 relative to coronal values with 10 of the 40 open field events lying in this range. 28 of the 40 constitute the core of the histogram, all having normalized Fe/O from 0-3.5. The remaining 12 events form a well defined high enhancement tail extending to one event with an measured enhancement of 12.69 times coronal. For the closed field configuration events (CCEs), at low energies (shown in blue in the figure), 13 of the 18 events have composition ratios between 0.5-2.5 times coronal with 5 events of greater than 3.5 times coronal acting as a second smaller population. For all events within the low-energy ULEIS sample, both open and closed events show average enhancements significantly above the coronal average of 0.134 taken from Reames (1999). At low energies, the OCEs have a mean enhancement is 3.41 times coronal (median is 2.36 times coronal) while CCEs have mean enhancements of 2.31 times coronal (median is 2.00 times coronal) (see Table 6.2). The open field mean is increased largely due to the events in the extended high enhancement tail; however, in this case, it is most

important to note that both types of events show mean enhancements above the average coronal values for the low energies (0.32-0.45 MeV/nuc). Such enhancements were noted in the spectral comparison of the 2002 April 21 and 2002 August 24 events shown in Chapter 2 (Figure 2.8).

Energy (MeV/nuc)	Mean Fe/O (Open)	Median Fe/O (Open)	Max Fe/O (Open)	Mean Fe/O (Closed)	Median Fe/O (Closed)	Max Fe/O (Closed)
0.32-0.45	3.41	2.36	12.69	2.31	2.00	5.63
30-40	1.90	0.90	5.78	1.70	0.84	4.64
25-80	1.85	0.98	8.60	2.61	1.62	6.90

Table 6.2 Statistical comparison of closed configuration and open configuration related SEP composition.

For the high-energy data from SIS, 30-40 MeV/nuc from Tylka et al. (2005) and 25-80 MeV/nuc from Cane et al. (2006), we find the majority of events to possess open field to some extent. In both distributions, Figure 6.4 (middle and bottom panels respectively), we find the OCEs show a strong peak for Fe/O values at coronal values or less. For the 25-80 MeV/nuc energy range, we find 33 of the 64 OCEs show normalized Fe/O $\leq$ 1 and 42 of the 64 events $\leq$ 2 times the coronal average. The OCEs for both these high-energy datasets show mean enhancements of 1.90 and 1.85 respectively. The median values for these energies are 0.90 and 0.98 respectively, indicating the distribution is skewed with most events near coronal values, and the measured mean is greatly influenced by the high-enhancement tail. The distributions and mean values of the compositions for the open field events for both high energy data sets show similar results independent of energy. The CCEs, however, have

significant variations at the higher energies. For the 30-40 MeV/nuc event, the closed field distribution indicates a similar peak to that seen in the open field. However, for the highest energy data, a clear peak at low enhancements is not as well defined. The closed distribution is influenced by approximately half the closed events having Fe/O enhancement greater than twice coronal, resulting in a mean enhancement at the highest energy of 2.60 (median enhancement is 1.62 as compared to 0.98 for OCEs at 25-80 MeV/nuc) , the highest mean closed field enhancement of the three energy ranges discussed.

The marked increase in the mean elemental enhancements for closed field events at the highest energy range is worth noting because increasing enhancements were found with the 2002 August 24 event which was shown in the PFSS extrapolations to be completely closed. It is plausible that higher energy flare-associated remnant particles could be contained within the closed structures, which serve as magnetic traps, providing a larger component of high energy heavy elements in the seed population for shock acceleration. However, the structures often lie low in the corona, and as such there remains a significant question as to whether a shock can form and accelerate particles at these low coronal heights. A shock forming at these low heights would be able to accelerate particles which had been confined within closed loop magnetic traps. This would, in turn increase the high-energy, flare-accelerated seed population.

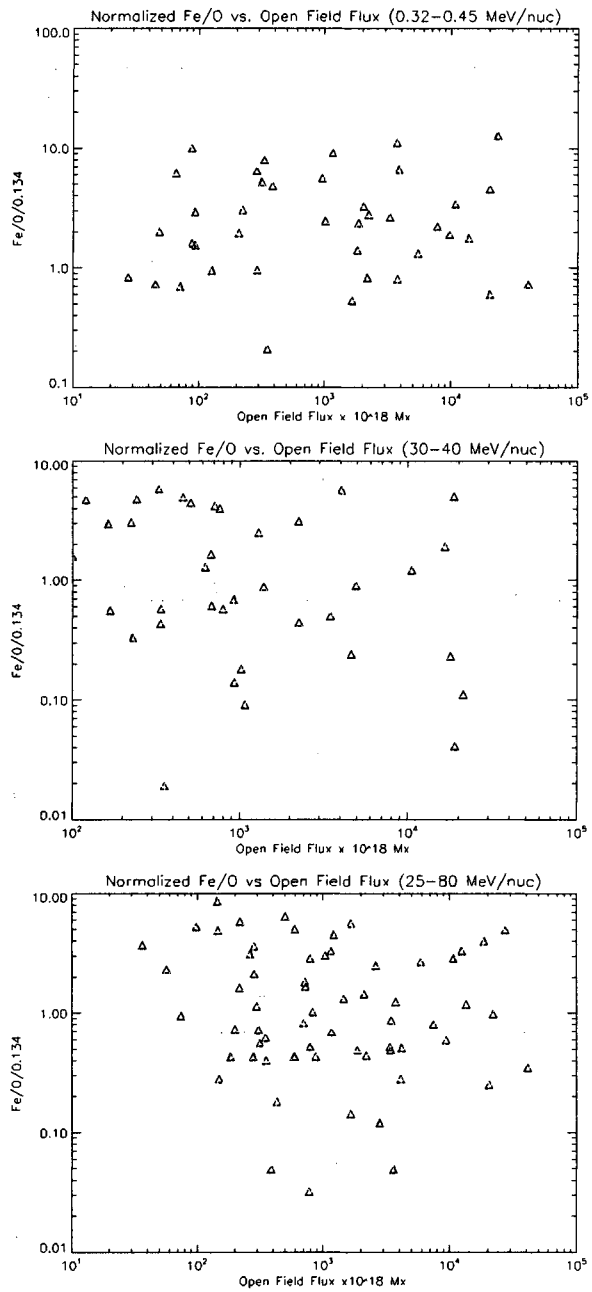

Figure 6.5 Scatter plots of normalized Fe/O vs open field magnetic flux for each of the three energy ranges (0.32-0.45 MeV/nuc, 30-40 MeV/nuc, 25-80 MeV/nuc). Fe/O ratios normalized to accepted coronal value 0.134 (Reames, 1999).

6.4.2 Open Field Influence on SEP Composition

To quantify the effects of open field availability across the energy spectrum for SEP events, we calculate the available open flux within the active regions as described in Section 6.2 and plot the Fe/O abundance ratio for the respective events to determine a relationship, if any, between the heavy element enhancements of large gradual SEP events and the existence of open field and more importantly a pathway for the high-energy particles to interplanetary space. Figure 6.5 shows the scatter plots of composition vs. open field for all three energy ranges. In all three cases, we find no statistically significant correlation with the amount of open magnetic flux. At the higher energies, the data show a slight trend of decreasing composition with increasing open field; however, this decrease is not statistically significant, R=-0.244 for 30-40 MeV/nuc data. These results suggest that the composition of large gradual SEP event is independent of the open magnetic field flux based upon our PFSS extrapolations. We will discuss caveats to the magnetic analysis in Section 6.5.

6.4.3 Flare Productivity Results

For the high energies, where elemental abundances enhancements are believed to be influenced by flare particle populations, the role of increased flare productivity must be further explored. To this end, we have determined flare index values for SEP events which are linked to a specific active region. The specifics of the flare index

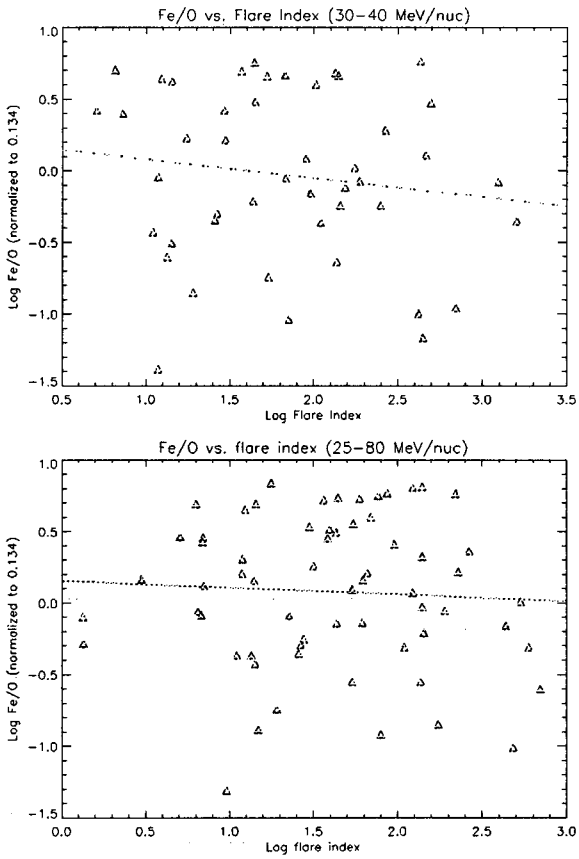

Figure 6.6 Scatter plots of log(normalized Fe/O) vs log(flare index) for the two highest energies (30-40 MeV/nuc, 25-80 MeV/nuc). The two energy ranges are shows because flare accelerated particles are believed to have their strongest contribution at higher energies. Fe/O ratios normalized to accepted coronal value 0.134 (Reames, 1999).

calculation are given in Section 6.3. We find flare indices covering three orders of magnitude with the strongest values (of order 1000) being attributed to AR 10486 of October-November 2003. The plots in Figure 6.6 show the variation of Fe/O ratio vs. the calculated flare index. Each energy range shows a wide scatter with no discernible trend in the data signifying any notable relationship. To confirm the lack of a relationship in both energies we have included in the plots the best linear fit to the data. Both of these fits result in nearly horizontal lines with wide scatter and show no clear relationship between the flare productivity and the abundance ratios. Thus, at these high energies, the Fe/O abundance ratio is independent of the flare activity in the event-associated active region.

6.5 Conclusions and Future Extensions

We have presented in this chapter an investigation into the role of the pre-event solar environment in shaping the resulting SEP particle distributions seen at 1AU. We have investigated both qualitative and quantitative aspects of the magnetic configuration as well as investigated a simplified measure of flare productivity to determine any relevance to the existence of heavy element enhancements in the SEPs. For this study, we have the following conclusions.

- At ULEIS energies (0.32-0.45 MeV/nuc), both OCEs and CCEs show significant heavy element enhancements with the OCEs have mean enhancements of 3.41 times coronal (median: 2.36) , although the mean is influenced by a significant

high enhancement tail extending to nearly 13 times coronal. Closed field events exhibit a mean enhancement of 2.31 times coronal (median: 2.00). The results are consistent with the examples of the 2002 April 21 and 2002 August 24 (open and closed event respectively) both of which show enhancements above coronal values at low energies (see Figure 2.8).

- At the highest energy range (25-80 MeV/nuc), we find a marked increase in the mean enhancement of closed field events to 2.60 times coronal. The increased enhancements at high energy for closed field events is consistent with the spectral observations of 2002 August 24 and suggest that other closed field events may exhibit similar increasing spectra, though further study of individual closed field events is recommended.

- We find that the heavy elements enhancements of large SEP events vary independently of the amount of open field in event where open field is present. We find no significant correlation between the available open field flux determined from PFSS extrapolations and the variation in Fe/O ratio.

- We also find that the composition variations are independent of flare activity within the associated active region, quantified via a modified flare index calculation which relies on the soft X-ray (1-8 Å) peak flux measured from GOES for flares associated with the respective active regions.

Our observations and analysis here shows evidence that both OCEs and CCEs show high enhancement tails at all energies suggesting that both open and closed events can contribute to high enhancement events. At high energies, where the influence of flare particles is most expected within the SEP events (Cane et al., 2006; Tylka et al. 2005), three of the four populations we measure show median Fe/O values lower than the coronal average. Only the closed field events at the highest energies (25-80 MeV/nuc) exhibit median Fe/O enhancements. This suggests that flare-accelerated particles may significantly affect the observed SEP populations for these events; however, as we have discussed briefly above, many of the closed loops seen in these events occur at low coronal heights. There is significant debate as to whether shocks can form at heights low enough to accelerate particles confined in these structures. It is important to note that all four high energy populations do show high enhancement tails. For the OCEs, it is possible that flare particles could stream out to interplanetary space via the open field. If these field lines are well-connected to the earth enhancements seen at 1AU would be possible due to a direct flare component. Further investigations of these events should concentrate on those events with observed enhancements, further analyzing the spectral characteristics and the relevance of the flare location. Flare location would clarify the magnetic connection between the events and earth. The spectral properties, particularly the influence of high-energy particles, could clarify the nature of the shock geometry. Enhancements

at high energies within the closed field structures suggest a flare seed population at those energies, but the lack of open field appears to keep the particles at the Sun. Higher energy particles have been shown to shown to be preferentially accelerated by quasi-perpendicular shocks. If so, and if shocks can form low enough these CCEs could provide a solar activity signature for SEPs with enhancements that increase with energy as discussed by Tylka et al. (2005), in particular the 2002 August 24 example.

Further studies relating pre-event solar conditions to SEP event measurements should be investigated, however, taking into account modifications to both the flare productivity analysis and the magnetic field extrapolations. While the potential field is a reasonable approximation for the large-scale corona, it cannot discern small-scale features near the flare and relate them specifically to the production of particles during the flare; therefore a further investigation of magnetic field configurations and their influence on SEP properties should make use of improved magnetic models such as linear force-free and non-linear force-free models to take into account current distributions in the corona and modify the resulting field. In addition, the flare index calculation should be modified to take into account the complete soft X-ray flux rather than just the peak measurement used in flare classification. Finally, a future extension of this work should further study the complete particle spectra for events with closed field configurations to further clarify the significance of the increased enhancements

we see at higher energies in these events. These future studies will further clarify the nature of the relationship between the solar environment and the results energetic particle distributions.

In addition, future investigations should take into account additional elements ratios and properties such as charge states or charge to mass ratio. We use Fe/O ratios in this study as it is the common link between the three composition study; however, it has been shown (Reames, 1999; Tylka et al., 2005) that this ratio is a key diagnostic of the existence of a flare particle component to the seed population. Flare-accelerated impulsive flares have Fe/O ratios of order unity as compared to the nominal value of 0.134 for coronal abundances (Reames, 1999). Thus, gradual SEPs showing enhancements above coronal values suggest significant influence of flare particles.

Chapter 7
Conclusions and Future Work

7.1 Summary and Conclusions

In this thesis, we have investigated the vital roles that the solar magnetic field and the acceleration of flare-associated particles play within explosive solar transients. We have used observations of emission signatures in the chromosphere to clarify the spatial and temporal relationships between hard X-ray and ultraviolet emission to place observational constraints on the nature and location of the energy release and particle acceleration within the flare, and to provide insight into the structure of the magnetic field and its influence on the flaring process. To obtain an understanding of the development of the 3D magnetic field, we have compared the development of structures known as QSLs with the evolution of the observed hard X-ray emission within flares. Work with QSLs, and the separatrix surfaces with which they are associated, has been largely theoretical (Démoulin et al., 1997; Titov et al., 2002) as attempts to understand the 3D coronal field and its importance to flares has progressed. The interaction of separatrix surfaces has been theoretically linked to magnetic reconnection and the release of free magnetic energy, particularly near a QSL. Our determination of QSLs within the flaring regions and the association of their locations with the observed chromospheric hard X-rays signatures provides an observable means by which to relate and examine the nature of these complex magnetic structures and the physical

processes that drive the flare and govern the flare emission. Finally, acknowledging the influence that solar transients wield on both the solar and interplanetary environments, we have clarified the relationship between the pre-event solar conditions and the subsequent accelerated particle signatures observed in large gradual SEP events at 1 AU. The energetic particles seen at Earth, particularly those at high energies, have direct and adverse complications for satellites, human spaceflight, and the Earth's magnetic environment. In our study, we find a qualitative connection between the solar magnetic field structure, at the time of the SEP event-associated flare, and the measured abundances of high-energy heavy elements at earth.

Our multi-faceted analysis of solar flares has shown that the traditional 1D single loop description of flares, described in Chapter 1, can only account for a portion of the observed emission seen in flares and that the entire flaring region, not just the localized loop structures, contributes significantly to the complex flare emission observed. Specifically:

- While a component of the temporally correlated UV and HXR emission develops co-spatially, in a number of events we find correlated emission with clear spatial separations which indicate not only the need for additional structural complexity in the flaring region, but also suggest the need for a more complex, energy-dependent acceleration mechanism to create the observed production of UV emission in some locations without discernible HXRs and vice versa.

- In addition to indicating the need for a more complex magnetic topology, the emission distribution and its evolution over the course of the flare, indicates that a complex energy release and time-dependent particle acceleration mechanism is required to produce the distributed but localized sources of UV and HXR emission (Linton and Longcope, 2006; Aschwanden and Alexander, 2001).

- We find sources of UV emission which evolve spatially separated from the main flare ribbons. These sources show significant time delays with respect to the HXRs, contrary to the relationships found in earlier works. For these sources we find their emission to be more closely linked with lower energy X-ray emission believed to originate from a more thermal origin. Thus, we suggest that the overall UV emission in flares must result from a combination of responses to both directly injected non-thermal electrons, associated with HXRs, and a thermal response either from the bulk energization of thermal particles or other thermal processes (e.g. conduction fronts, bulk chromospheric heating).

- In relation to 3D magnetic topology, we find strong observational evidence of a connection between the hard X-ray emission sources in the chromosphere and the location of QSLs determined within the magnetic field. Due to the theoretical link between QSLs and magnetic reconnection, QSLs are likely sources of energy release and particle acceleration resulting in the hard X-ray emission.

The findings here confirm that relationship and relates it to the spatial and temporal development of the active region as a whole.

In our studies relating the pre-event solar conditions to SEP composition measurements we examined both the magnetic structure and the flare productivity for the event-associated active regions and found:

- At high energies, those events occurring in active regions with entirely closed field configurations show, on average, significantly enhanced Fe/O ratios relative to the nominal coronal values. Such enhancements are believed the result of an increased contribution of a flare-accelerated population. However, these closed field structures lie low in the corona so there remains a significant question as to whether shocks can form low enough to accelerate the confined flare-accelerated particles.

- In contrast to the marked differences in composition ratios at high energies between completely closed field events and open field events, The heavy element composition seems to vary independently with respect to the amount of open field flux. The enhancements in closed field cases suggest that the particles confined to the solar corona play a significant role in shaping the enhancements observed; however, the observations raise the question of how these energetic particles end up in the vicinity of the CME-driven shock to be further acceler-

ated to SEP energies.

- Finally, the composition also varies independently of flare productivity as determined by the calculation of the flare index for each active region. The apparent independence of SEP composition with flare productivity calls into question the influence of a flare-accelerated seed particle population and how these flare-like particles reach and interact with the shock.

The findings presented here provide a number of additional future work opportunities. Many of these future studies will be able to take advantage of several recently launched missions including STEREO and Hinode. We briefly address some of these future directions in the next section.

7.2 Future Work

7.2.1 Future Observational Constraints on Magnetic Topology and Energy Release

In the work presented here, we have shown the importance of the 3D topology of the magnetic field in the flaring process. Future studies of this kind be able to use 3D image reconstructions from STEREO EUVI to observe coronal magnetic structures in EUV wavelengths due to emission from the entrained plasma. These observations will provide a 3D representation of coronal structure and will serve as a key observational constraint on magnetic field modelling of the corona. Future studies could build upon our work by comparing the temporal evolution and spatial development of

chromospheric emission, like HXRs, with the observed coronal structures seen during the flare. Such a study would provide clarification of the role of the magnetic topology in the flare. In addition, further insight would be gained with respect to the energy release and dissipation in the flaring region by determining the topology and energy transport mechanisms in areas of the flare region beyond the observable X-ray loops and post-flare arcades.

An additional study is currently underway to focus solely on the UV continuum emission. In our findings, we note the UV emission occurs in multiple physical processes or perhaps via the acceleration of multiple particle populations. A further study focused on the UV will determine the nature of the UV production mechanism, which is presently unclear, and further constrain the relationships between UV emission, flare energy release, and particle acceleration. Building on our findings of UV sources which are temporally related to lower energy X-ray emission, further events studied with UV and X-ray emission will provide further insight into the nature of the late developing UV emission sources which we have associated with thermal emission due to temporal association with lower energy X-rays. Such studies will be enhanced by the availability of new X-ray data from the XRT telescope aboard the Hinode spacecraft (Kosugi et al., 2007; Golub et al., 2007).

Further observational connections between QSLs and flare emission can be determined through the comparison of determined QSL positions with STEREO observa-

tions of coronal structures seen within flares. The STEREO observations will provide corroboration of visible magnetic structures within the corona. Determinations of QSLs from magnetic extrapolations should correspond in theory to these observed structures. Also further X-ray and EUV observations, in combination with QSL determinations with provide further insight into the relationship of QSLs in the corona to the energy release to flare emission seen in all observed wavelengths.

7.2.2 Future Advancements Relating SEP observations to Pre-Event Solar Conditions

Further investigations of the solar magnetic field configuration and its influence on SEP properties should make use of improved magnetic models such as linear force-free and non-linear force-free models to take into account current distributions in the corona which will modify the resulting field. These adaptations will improve on our results by including non-potentiality in the field extrapolations permitting a closer representation of the field near the flaring region. In addition, subsequent studies should also consider making use of available full MHD models within the solar community which when used in combination can establish the connection between smaller scale magnetic fields of the flaring region and the larger scale magnetic fields in the corona and provide a stronger physical background for use in relating the solar and interplanetary observation. Such models can be implemented via the Community Coordinated Modelling Center (CCMC) and through direct collaboration with the

MHD modelers.

In addition, the flare index calculation should be modified to take into account the complete soft X-ray flux rather than just the peak measurement used in flare classification. Finally, future extensions of this work should address the complete particle spectra at high energies for events with closed field configurations. These spectral studies will provide the opportunity for additional observational evidence of higher energy particles remaining confined within the low-lying closed loops, strengthening the significance of these closed field configurations with respect to the increased enhancements seen in these events. These studies and further investigations of the potential for shock-acceleration low in the corona will determine if and how the high-energy flare-accelerated particles can be shock-accelerated from low-lying closed loops. Additional studies should also take into account additional properties of the observed SEP composition (e.g. charge states, different elemental ratios such as Fe/C or ^{3}He/^{4}He, or mass to charge ratios). Higher charge states and enhanced ^{3}He/^{4}He ratios are signatures of flare-associated impulsive events (Tylka, 2004); therefore, including these observations will provide additional observational corroboration of flare particle influence in SEP events with enhancements. Desai et al. (2006) have shown that heavy element enhancements increase with mass/charge (M/Q) ratio; M/Q ratio would serve as a additional observational characteristic of the SEP properties at 1 AU which could be compared to the observed solar conditions.

Appendix A

A.1 Particle Composition Data for Discussion SEP Studies

This appendix provides the data tables from the SEP composition studies discussed in Chapter 6. The table of low-energy composition data from ULEIS, taken from Desai et al., (2006), are shown in Figure A.1. Data for the SIS data from 30-40 MeV/nuc, including Fe/O ratio and event timing data from studies by Tylka et al. (2005, 2006) are included in Figure A.2. Finally, the data from SIS observations at 25-80 MeV/nuc from Cane et al. (2006) are included in Figures A.3 and A.4.

TABLE 2

SAMPLING INTERVALS AND EFFICIENCIES, ABUNDANCES FOR 0.32-0.45 MeV/NUC SOLAR PARTICLE EVENTS

SEP	Year	ULEIS Sampling Intervals (month day, UT)[a]	0.5-2 MeV nucleon^{-1} ^{3}He/^{4}He (×10^3)	0.32-0.45 MeV nucleon^{-1} ^{4}He/O	C/O	N/O	Ne/O	Mg/O	Si/O	S/O	Ca/O	Fe/O
1	1997	Nov 4 12:05-Nov 6, 11:55	1.05 ± 0.43	56.6 ± 39.1	0.408 ± 0.026	0.122 ± 0.012	0.177 ± 0.018	0.237 ± 0.019	0.283 ± 0.022	0.090 ± 0.011	0.045 ± 0.008	0.092 ± 0.013
2[b]	1998	Apr 20, 15:40-Apr 21, 04:00 Apr 23, 19:10-Apr 26, 04:35	<0.21	142.5 ± 98.5	0.363 ± 0.063	0.124 ± 0.012	0.169 ± 0.016	0.291 ± 0.021	0.317 ± 0.018	0.092 ± 0.008	0.012 ± 0.004	0.093 ± 0.009
3	1998	May 4 11:55-May 7, 00:10	5.32 ± 0.78	141.2 ± 90.6	0.232 ± 0.014	0.090 ± 0.008	0.215 ± 0.014	0.283 ± 0.014	0.272 ± 0.016	0.085 ± 0.008	0.031 ± 0.007	0.080 ± 0.014
4[b]	1998	Aug 25, 02:10-Aug 25, 23:00 Aug 27, 04:05-Aug 28, 20:40	<0.39	31.9 ± 20.7	0.369 ± 0.013	0.114 ± 0.005	0.172 ± 0.008	0.250 ± 0.011	0.222 ± 0.009	0.053 ± 0.004	0.015 ± 0.002	0.239 ± 0.009
5[b]	1998	Sep 23, 07:55-Sep 24, 15:00 Sep 25, 08:20-Sep 25, 22:45	5.84 ± 0.90	38.6 ± 24.2	0.424 ± 0.023	0.150 ± 0.009	0.145 ± 0.010	0.212 ± 0.013	0.149 ± 0.010	0.032 ± 0.005	0.005 ± 0.002	0.091 ± 0.007
6[b]	1998	Sep 30, 19:35-Oct 2, 04:50 Oct 2, 13:00-Oct 4, 24:00	<0.41	56.8 ± 39.2	0.528 ± 0.021	0.126 ± 0.008	0.156 ± 0.009	0.203 ± 0.010	0.150 ± 0.010	0.040 ± 0.004	0.010 ± 0.002	0.102 ± 0.008
7	1998	Nov 8, 02:00-Nov 9, 15:30	<0.52	33.8 ± 25.1	0.320 ± 0.010	0.122 ± 0.006	0.151 ± 0.006	0.224 ± 0.006	0.143 ± 0.005	0.032 ± 0.002	0.006 ± 0.001	0.083 ± 0.003
8	1999	Jan 21, 04:05-Jan 22, 13:40	<0.61	63.6 ± 43.9	0.325 ± 0.014	0.115 ± 0.007	0.156 ± 0.009	0.194 ± 0.010	0.156 ± 0.008	0.036 ± 0.005	0.009 ± 0.002	0.097 ± 0.005
9	1999	Apr 5-6, 20:05-Apr 7-8 13:50	<0.68	33.6 ± 21.3	0.439 ± 0.015	0.120 ± 0.008	0.175 ± 0.010	0.211 ± 0.011	0.157 ± 0.010	0.032 ± 0.005	0.010 ± 0.003	0.166 ± 0.010
10	1999	May 3, 19:45-May 5, 12:45 May 6, 23:45-May 9, 12:05	<0.41	104.0 ± 32.3	0.461 ± 0.015	0.131 ± 0.006	0.130 ± 0.006	0.214 ± 0.006	0.158 ± 0.007	0.054 ± 0.004	0.009 ± 0.002	0.110 ± 0.004
11	1999	Jun 1, 15:05-Jun 4, 08:40	23.50 ± 1.71	64.4 ± 30.1	0.295 ± 0.018	0.126 ± 0.011	0.139 ± 0.014	0.246 ± 0.016	0.168 ± 0.018	0.039 ± 0.008	0.014 ± 0.006	0.148 ± 0.022
12	1999	Jun 4, 11:35-Jun 6, 19:20	1.61 ± 0.51	35.4 ± 21.1	0.172 ± 0.009	0.106 ± 0.006	0.133 ± 0.005	0.251 ± 0.009	0.142 ± 0.011	0.139 ± 0.005	0.052 ± 0.004	1.063 ± 0.037
13[b]	2000	Apr 4, 19:00-Apr 6, 07:30 Apr 6, 21:40-Apr 7, 04:01 Apr 7, 12:35-Apr 8, 11:05	0.94 ± 0.46	85.4 ± 26.5	0.538 ± 0.013	0.122 ± 0.006	0.163 ± 0.006	0.240 ± 0.010	0.250 ± 0.011	0.060 ± 0.005	0.025 ± 0.003	0.375 ± 0.011
14[b]	2000	Jun 6, 20:25-Jun 8, 00:10 Jun 8, 10:20-Jun 10, 01:52	<0.55	78.5 ± 24.4	0.446 ± 0.014	0.125 ± 0.006	0.140 ± 0.006	0.191 ± 0.006	0.157 ± 0.007	0.030 ± 0.001	0.006 ± 0.001	0.115 ± 0.003
15	2000	Jun 10, 19:05-Jun 11, 21:10	<0.92	66.4 ± 30.1	0.375 ± 0.025	0.134 ± 0.011	0.168 ± 0.012	0.197 ± 0.014	0.134 ± 0.013	0.027 ± 0.009	0.011 ± 0.007	0.152 ± 0.026
16[b]	2000	Jul 15, 22:05-Jul 19, 05:40	<0.38	175.5 ± 52.8	0.380 ± 0.011	0.120 ± 0.006	0.190 ± 0.009	0.259 ± 0.011	0.219 ± 0.010	0.050 ± 0.004	0.020 ± 0.003	0.267 ± 0.008
17	2000	Jul 22, 10:35-Jul 23, 20:15	3.33 ± 0.96	39.7 ± 29.2	0.292 ± 0.017	0.106 ± 0.010	0.193 ± 0.013	0.222 ± 0.017	0.217 ± 0.014	0.033 ± 0.005	0.015 ± 0.004	0.155 ± 0.009
18	2000	Sep 12, 17:20-Sep 16, 14:00	<0.15	67.6 ± 21.0	0.305 ± 0.009	0.115 ± 0.004	0.127 ± 0.005	0.151 ± 0.005	0.106 ± 0.006	0.029 ± 0.003	0.007 ± 0.002	0.209 ± 0.007
19	2000	Oct 16, 13:30-Oct 20, 17:40	2.96 ± 1.11	111.4 ± 34.7	0.262 ± 0.020	0.092 ± 0.011	0.139 ± 0.014	0.194 ± 0.016	0.248 ± 0.020	0.101 ± 0.012	0.046 ± 0.008	0.609 ± 0.026
20	2000	Oct 23, 16:45-Oct 28, 02:20	4.14 ± 0.77	37.7 ± 14.7	0.435 ± 0.013	0.136 ± 0.006	0.168 ± 0.006	0.206 ± 0.006	0.212 ± 0.020	0.046 ± 0.004	0.014 ± 0.002	0.215 ± 0.007
21[b,c]	2000	Nov 9, 15:35-Nov 10, 02:40 Nov 10, 09:40-Nov 10, 16:20 Nov 10, 19:40-Nov 14, 22:00	<1.58	68.1 ± 21.3	0.572 ± 0.024	0.152 ± 0.015	0.150 ± 0.014	0.173 ± 0.016	0.144 ± 0.014	0.029 ± 0.006	0.013 ± 0.004	0.236 ± 0.012
22[b,c,d]	2000	Nov 24, 19:15-Nov 26, 02:30 Nov 26, 17:20-Nov 26, 19:10 Nov 27, 07:00-Nov 28, 00:05 Nov 29, 09:40-Nov 29, 22:20 Nov 30, 14:30-Nov 30, 21:30	2.96 ± 0.50	44.7 ± 13.3	0.308 ± 0.013	0.124 ± 0.008	0.172 ± 0.010	0.204 ± 0.011	0.133 ± 0.013	0.028 ± 0.006	0.010 ± 0.004	0.492 ± 0.013
23	2001	Jan 29, 01:00-Feb 1, 06:45	<0.42	102.3 ± 31.4	0.352 ± 0.011	0.121 ± 0.005	0.111 ± 0.005	0.147 ± 0.006	0.151 ± 0.007	0.060 ± 0.003	0.017 ± 0.002	0.274 ± 0.007
24[b]	2001	Apr 2, 01:55-Apr 4, 01:20 Apr 4, 21:45-Apr 5, 11:20	4.20 ± 0.76	167.0 ± 51.9	0.367 ± 0.009	0.107 ± 0.004	0.142 ± 0.013	0.185 ± 0.016	0.247 ± 0.015	0.092 ± 0.006	0.022 ± 0.004	0.456 ± 0.022
25[b,c]	2001	Apr 10, 11:10-Apr 11, 09:10	<0.63	89.8 ± 25.0	0.445 ± 0.024	0.148 ± 0.012	0.115 ± 0.010	0.227 ± 0.015	0.208 ± 0.019	0.098 ± 0.009	0.025 ± 0.005	0.372 ± 0.022
26	2001	Apr 15, 19:40-Apr 17, 17:50	<0.63	122.4 ± 30.8	0.290 ± 0.014	0.107 ± 0.008	0.156 ± 0.010	0.206 ± 0.014	0.176 ± 0.008	0.113 ± 0.008	0.047 ± 0.006	1.323 ± 0.047
27	2001	Apr 18, 06:05-Apr 21 10:05 Apr 21, 19:30-Apr 21, 21:30	3.06	66.9 ± 20.8	0.364 ± 0.015	0.118 ± 0.008	0.176 ± 0.010	0.271 ± 0.013	0.238 ± 0.013	0.044 ± 0.005	0.014 ± 0.003	0.206 ± 0.011
28[b,c]	2001	Apr 26, 17:45-Apr 27, 15:15 Apr 28, 03:40-Apr 30 01:45	2.50 ± 0.85	85.5 ± 28.5	0.522 ± 0.018	0.127 ± 0.009	0.146 ± 0.010	0.238 ± 0.013	0.135 ± 0.009	0.021 ± 0.004	0.008 ± 0.002	0.071 ± 0.004

TABLE 2 - *Continued*

SEP	Year	ULEIS Sampling Intervals (month day, UT)[a]	0.5-2 MeV nucleon^{-1} ^{3}He/^{4}He (×10^3)	0.32-0.45 MeV nucleon^{-1} ^{4}He/O	C/O	N/O	Ne/O	Mg/O	Si/O	S/O	Ca/O	Fe/O
29	2001	May 7, 15:35-May 9, 09:50	4.29 ± 0.77	80.1 ± 24.9	0.285 ± 0.016	0.116 ± 0.009	0.162 ± 0.011	0.231 ± 0.013	0.270 ± 0.016	0.062 ± 0.007	0.032 ± 0.005	0.698 ± 0.030
30	2001	Jun 15, 14:35-Jun 17, 10:50	3.06 ± 0.85	111.8 ± 45.0	0.574 ± 0.015	0.102 ± 0.007	0.134 ± 0.009	0.214 ± 0.011	0.234 ± 0.011	0.042 ± 0.005	0.019 ± 0.003	0.216 ± 0.009
31[b]	2001	Aug 9, 17:35-Aug 12, 04:50 Aug 12, 22:40-Aug 14, 13:40	1.35 ± 0.55	94.1 ± 20.2	0.500 ± 0.016	0.115 ± 0.005	0.139 ± 0.006	0.175 ± 0.007	0.165 ± 0.005	0.036 ± 0.003	0.009 ± 0.001	0.108 ± 0.003
32[b]	2001	Aug 16, 04:20-Aug 17, 06:00 Aug 17, 16:25-Aug 18, 04:25	2.31 ± 0.91	69.4 ± 20.6	0.540 ± 0.015	0.116 ± 0.008	0.152 ± 0.009	0.231 ± 0.012	0.222 ± 0.011	0.041 ± 0.004	0.015 ± 0.003	0.157 ± 0.007
33[b,c]	2001	Sep 24, 15:50-Sep 25, 15:00 Sep 27, 12:00-Sep 30, 22:30	<0.52	69.4 ± 21.1	0.477 ± 0.011	0.117 ± 0.005	0.143 ± 0.005	0.257 ± 0.008	0.243 ± 0.008	0.055 ± 0.003	0.022 ± 0.002	0.295 ± 0.008
34[b]	2001	Oct 1, 14:35-Oct 2, 05:35 Oct 3, 23:10-Oct 4, 08:00	1.04 ± 0.50	64.4 ± 14.6	0.234 ± 0.014	0.124 ± 0.008	0.162 ± 0.009	0.237 ± 0.012	0.182 ± 0.010	0.026 ± 0.003	0.010 ± 0.003	0.097 ± 0.004
35	2001	Oct 20, 09:10-Oct 21, 21:35	1.73 ± 1.09	50.4 ± 15.8	0.270 ± 0.016	0.098 ± 0.009	0.159 ± 0.011	0.246 ± 0.015	0.240 ± 0.013	0.047 ± 0.008	0.022 ± 0.005	0.439 ± 0.021
36[b]	2001	Nov 4, 19:35-Nov 5, 21:35 Nov 6, 20:10-Nov 8, 24:00	<5.05	37.6 ± 11.7	0.462 ± 0.022	0.130 ± 0.013	0.126 ± 0.012	0.221 ± 0.017	0.173 ± 0.016	0.045 ± 0.008	0.016 ± 0.004	0.228 ± 0.016
37	2001	Nov 22, 03:10-Nov 23, 22:50 Nov 24, 24:15-Nov 30, 10:00	<0.97	49.1 ± 15.5	0.360 ± 0.015	0.105 ± 0.006	0.152 ± 0.008	0.273 ± 0.012	0.201 ± 0.014	0.054 ± 0.005	0.020 ± 0.004	0.240 ± 0.009
38	2001	Dec 24, 04:35-Dec 26, 18:00	<0.42	39.7 ± 12.2	0.319 ± 0.010	0.112 ± 0.005	0.150 ± 0.006	0.207 ± 0.008	0.260 ± 0.009	0.079 ± 0.004	0.022 ± 0.003	0.666 ± 0.014
39	2001	Dec 30, 12:05-Jan 7, 12:30	1.05 ± 0.30	55.9 ± 17.2	0.362 ± 0.024	0.109 ± 0.013	0.145 ± 0.016	0.205 ± 0.016	0.198 ± 0.016	0.053 ± 0.008	0.020 ± 0.005	0.342 ± 0.029
40	2002	Jan 10, 19:30-Jan 14, 06:20	<0.44	94.9 ± 29.3	0.437 ± 0.016	0.147 ± 0.009	0.151 ± 0.009	0.164 ± 0.007	0.146 ± 0.006	0.036 ± 0.002	0.007 ± 0.001	0.080 ± 0.003
41	2002	Feb 20, 09:35-Feb 22, 09:50	23.01 ± 1.42	104.4 ± 31.2	0.540 ± 0.017	0.102 ± 0.006	0.195 ± 0.012	0.226 ± 0.017	0.404 ± 0.021	0.118 ± 0.010	0.056 ± 0.008	1.489 ± 0.057
42	2002	Mar 22, 16:20-Mar 25, 09:45 Mar 25, 23:25-Mar 26, 11:10	1.66 ± 0.46	99.4 ± 12.5	0.370 ± 0.015	0.130 ± 0.006	0.179 ± 0.006	0.232 ± 0.010	0.229 ± 0.011	0.045 ± 0.004	0.022 ± 0.003	0.268 ± 0.008
43	2002	Apr 21, 05:35-Apr 23, 21:50 Apr 24, 14:25-Apr 24, 19:00	<1.91	24.0 ± 8.7	0.519 ± 0.022	0.116 ± 0.012	0.098 ± 0.011	0.298 ± 0.022	0.329 ± 0.024	0.080 ± 0.011	0.037 ± 0.007	0.752 ± 0.045
44	2002	May 22, 08:35-May 25, 05:20 May 27, 18:10-May 24, 23:35	<1.76	56.4 ± 17.4	0.392 ± 0.015	0.122 ± 0.007	0.160 ± 0.007	0.188 ± 0.009	0.159 ± 0.009	0.041 ± 0.004	0.009 ± 0.001	0.125 ± 0.006
45	2003	Jul 7, 15:50-Jul 10, 12:15	1.65 ± 0.84	41.5 ± 12.9	0.262 ± 0.010	0.112 ± 0.006	0.161 ± 0.007	0.157 ± 0.007	0.145 ± 0.007	0.026 ± 0.003	0.005 ± 0.001	0.058 ± 0.002
46[b]	2002	Jul 16, 07:00-Jul 17, 15:05 Jul 17, 21:35-Jul 18, 16:55	<0.57	88.2 ± 23.5	0.381 ± 0.016	0.115 ± 0.007	0.125 ± 0.008	0.196 ± 0.010	0.205 ± 0.011	0.045 ± 0.005	0.016 ± 0.005	0.388 ± 0.009
47[b]	2002	Jul 22, 05:05-Jul 25, 00:55 Jul 26, 09:20-Jul 29, 03:20	0.79 ± 0.33	81.9 ± 25.6	0.368 ± 0.010	0.120 ± 0.004	0.128 ± 0.005	0.213 ± 0.007	0.178 ± 0.006	0.033 ± 0.002	0.008 ± 0.001	0.127 ± 0.004

TABLE 2 - *Continued*

SEP	Year	ULEIS Sampling Intervals (month day, UT)[a]	0.5-2 MeV nucleon^{-1} ^{3}He/^{4}He (×10^3)	0.32-0.45 MeV nucleon^{-1} ^{4}He/O	C/O	N/O	Ne/O	Mg/O	Si/O	S/O	Ca/O	Fe/O
48	2002	Aug 14, 05:05-Aug 15, 19:50	13.86 ± 0.99	51.2 ± 15.0	0.302 ± 0.014	0.124 ± 0.008	0.141 ± 0.009	0.201 ± 0.011	0.178 ± 0.013	0.036 ± 0.006	0.010 ± 0.003	0.253 ± 0.009
49	2002	Aug 24, 05:25-Aug 26, 12:00	1.82 ± 0.66	52.9 ± 16.4	0.336 ± 0.011	0.114 ± 0.005	0.136 ± 0.006	0.251 ± 0.009	0.285 ± 0.010	0.077 ± 0.004	0.027 ± 0.003	0.536 ± 0.014
50	2002	Sep 6, 11:05-Sep 7, 13:20 Sep 9, 10:40-Sep 12, 21:25	1.89 ± 0.68	131.9 ± 24.8	0.428 ± 0.020	0.149 ± 0.009	0.166 ± 0.011	0.248 ± 0.013	0.219 ± 0.015	0.030 ± 0.004	0.009 ± 0.002	0.143 ± 0.010
51	2002	Nov 9, 19:40-Nov 11, 07:40	<1.22	42.8 ± 28.9	0.389 ± 0.025	0.126 ± 0.012	0.172 ± 0.014	0.259 ± 0.021	0.334 ± 0.023	0.103 ± 0.011	0.026 ± 0.005	0.751 ± 0.035
52[b]	2010	May 29, 08:35-May 29, 10:25 May 30, 04:00-May 30, 11:20 May 31, 02:20-May 31, 07:20	<0.40	101.4 ± 31.5	0.463 ± 0.015	0.129 ± 0.007	0.177 ± 0.008	0.127 ± 0.009	0.221 ± 0.010	0.052 ± 0.004	0.019 ± 0.003	0.328 ± 0.011
53	2005	May 24, 08:10-Jun 2, 16:05	<0.78	52.2 ± 16.2	0.356 ± 0.015	0.122 ± 0.007	0.139 ± 0.008	0.228 ± 0.011	0.208 ± 0.011	0.059 ± 0.005	0.017 ± 0.003	0.304 ± 0.012
54	2006	Jun 10, 05:55-Jun 25, 08:30	<0.28	106.4 ± 33.0	0.531 ± 0.013	0.149 ± 0.005	0.195 ± 0.005	0.295 ± 0.006	0.461 ± 0.005	0.030 ± 0.001	0.010 ± 0.001	0.126 ± 0.004
55	2003	Oct 26, 21:20-Oct 27, 20:30	1.67 ± 0.66	84.0 ± 24.2	0.503 ± 0.022	0.159 ± 0.012	0.200 ± 0.017	0.278 ± 0.021	0.292 ± 0.025	0.121 ± 0.014	0.058 ± 0.010	1.701 ± 0.075
56[b,c]	2003	Oct 29 14:30-Oct 30, 00:00	<2.39	7.56 ± 22.9	0.342 ± 0.035	0.181 ± 0.019	0.160 ± 0.020	0.171 ± 0.025	0.198 ± 0.028	0.042 ± 0.013	0.019 ± 0.009	0.290 ± 0.029
57	2005	Nov 3, 00:10-Nov 5, 15:05	<0.40	40.6 ± 12.0	0.389 ± 0.009	0.146 ± 0.004	0.199 ± 0.004	0.250 ± 0.005	0.422 ± 0.012	0.114 ± 0.004	0.043 ± 0.003	2.17 ± 0.08
58	2003	Dec 2, 14:55-Dec 6, 01:00	<0.85	53.0 ± 16.7	0.758 ± 0.020	0.244 ± 0.013	0.191 ± 0.009	0.216 ± 0.008	0.213 ± 0.010	0.064 ± 0.005	0.034 ± 0.003	0.887 ± 0.022
59	2006	Apr 11, 10:50-Apr 12, 12:00 Apr 12, 20:30-Apr 13, 10:10	<0.63	74.1 ± 19.6	0.562 ± 0.014	0.122 ± 0.007	0.123 ± 0.007	0.196 ± 0.010	0.236 ± 0.012	0.052 ± 0.005	0.015 ± 0.002	0.316 ± 0.010
60[b]	2010	Jul 25, 19:35-Jul 26, 14:50 Jul 27, 07:20-Jul 28, 20:10	<0.45	110.8 ± 36.4	0.430 ± 0.013	0.079 ± 0.006	0.157 ± 0.007	0.281 ± 0.010	0.255 ± 0.010	0.051 ± 0.004	0.025 ± 0.003	0.356 ± 0.011
61	2006	Sep 13, 12:00-Sep 17, 12:00	<0.36	76.2 ± 23.0	0.421 ± 0.014	0.133 ± 0.006	0.122 ± 0.006	0.190 ± 0.009	0.161 ± 0.007	0.032 ± 0.003	0.008 ± 0.001	0.140 ± 0.005
62	2006	Sep 30, 09:15-Sep 30, 13:15	<0.61	70.- ± 22.7	0.335 ± 0.015	0.105 ± 0.008	0.109 ± 0.008	0.157 ± 0.011	0.179 ± 0.012	0.037 ± 0.005	0.009 ± 0.002	0.232 ± 0.009
63	2006	Nov 3, 16:40-Nov 5, 12:00	60.64 ± 4.94	86.0 ± 29.5	0.347 ± 0.009	0.112 ± 0.005	0.220 ± 0.007	0.353 ± 0.012	0.424 ± 0.014	0.058 ± 0.004	0.014 ± 0.002	0.051 ± 0.002
64	2005	Jan 20, 11:05-Jan 21, 09:40 Jan 21, 22:00-Jan 21, 20:05	<0.77	66.6 ± 29.1	0.581 ± 0.020	0.104 ± 0.009	0.147 ± 0.011	0.152 ± 0.011	0.150 ± 0.013	0.044 ± 0.007	0.018 ± 0.005	0.284 ± 0.012

[a] Sampling times based on onset of ~1 MeV nucleon^{-1} ion intensity

[b] Excluded portions when ULEIS suffered loss in efficiency or from saturation effects.

[c] Excluded time intervals around the passage of B stacks at ACE.

[d] Sampling interval may contain ions from multiple injections (see Reames 2005).

Figure A.1 Low energy composition data (0.32-0.45 MeV/nuc) taken from Table 2 of Desai et al. (2006)

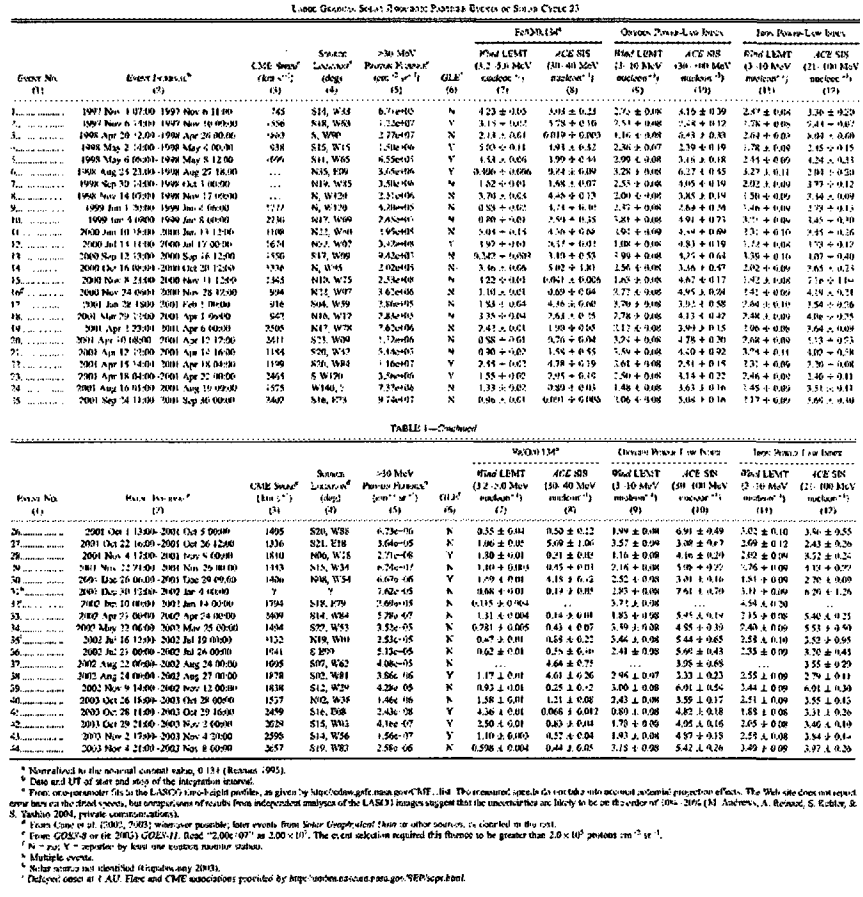

Figure A.2 Table of composition ratios and spectral indicies for SIS observations from Table 1 of Tylka et al. (2005). With supplemental data for events from 2004 and 2005 taken from Tylka et al. (2006)

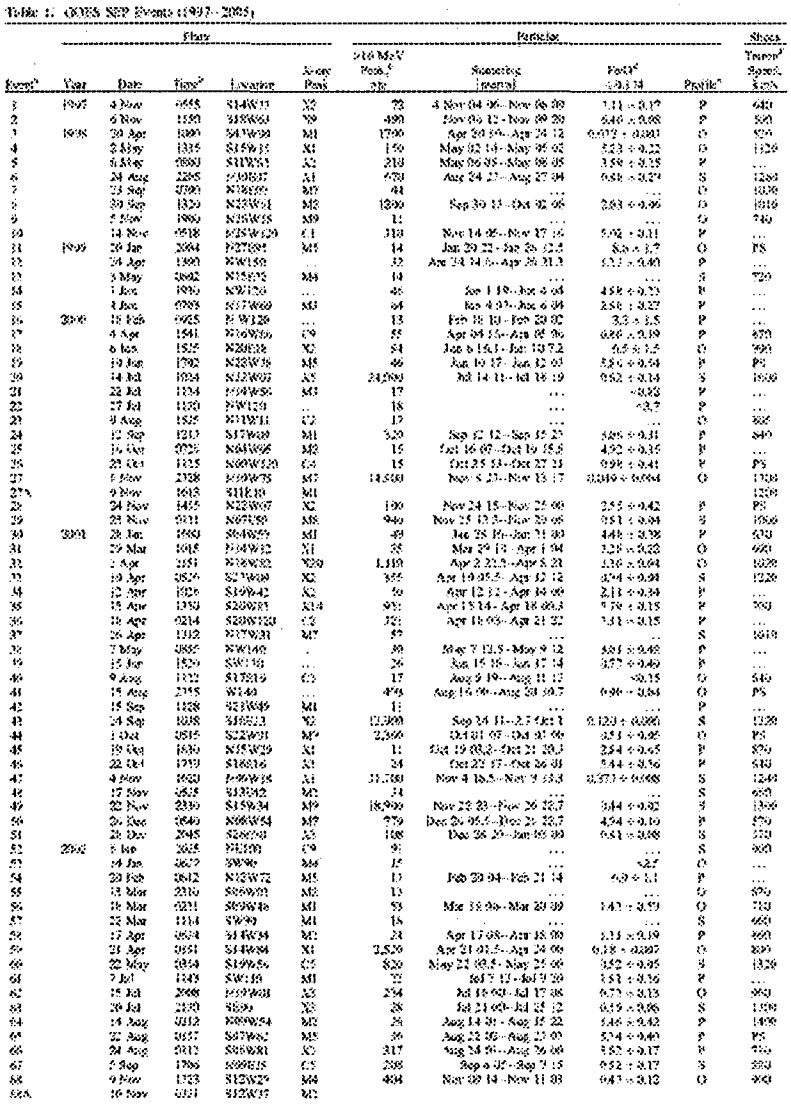

Figure A.3 Table of composition ratios and event information for SIS observations (25-80 MeV/nuc) from Table 1 of Cane et al. (2006).

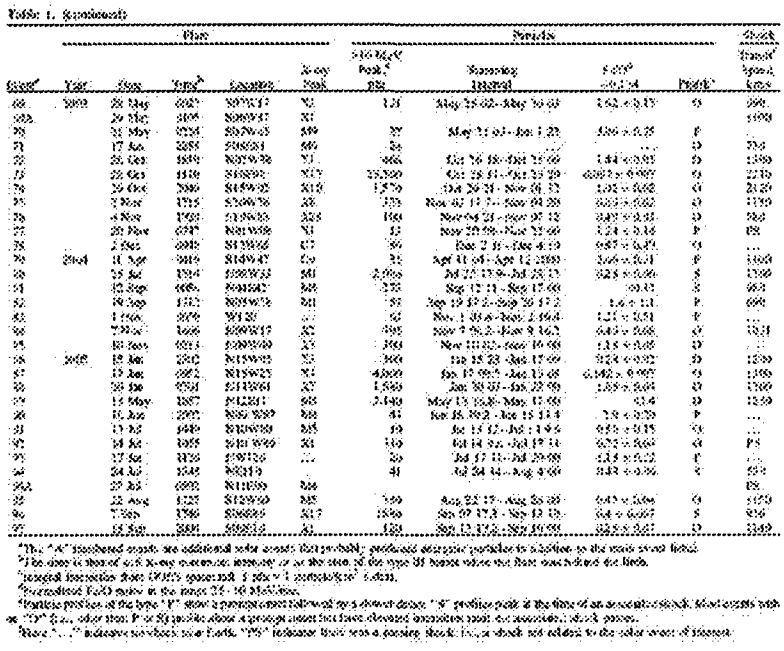

Figure A.4 Table of composition ratios and event information for SIS observations (25-80 MeV/nuc) continued from Table 1 of Cane et al. (2006).

References

1. Abramenko, V.I. "Relationship between magnetic power spectrum and flare productivity in solar active regions" Ap.J **629**, 1141 (2005).

2. Alexander, D. "The coronal trap model in solar flares." Astronomy and Astrophysics **235**, 431 (1990).

3. Alexander, D. and Coyner, A.J. "Temporal and spatial relationships between ultraviolet and hard X-ray emission in solar flares", Ap.J, **640**, 505 (2006).

4. Alexander, D. and Metcalf, T.R. "A spectral analysis of the Masuda flare using Yohkoh Hard X-Ray Telescope Pixon reconstruction" Ap.J **489**, 442 (1997).

5. Alexander D. and Metcalf T.R. "Energy dependence of electron trapping in a solar flare" Solar Physics **210** 323 (2002).

6. Alexander, D. *et al.* "SHINE SEP Campaign Events: Detailed comparison of active regions AR9906 and AR0069 in the build-up to the SEP events of 21 Apr 2002 and 24 Aug 2002" SHINE 2004 Workshop, Big Sky, Montana, (2004).

7. Antalova, A "Daily soft X-ray flare index (1969-1972)" Contributions of the Astronomical Observatory Skalnate Pleso **26**, 98 (1996).

8. Antiochos, S.K. "The magnetic topology in solar eruptions" Ap.J **502**, 181 (1998).

9. Aschwanden, M. J. "Deconvolution of direct-precipitating and trap-precipitating electrons in solar flare hard X-rays I : methods and tests" Ap.J **502**, 455 (1998).

10. Aschwanden, M.J. "Particle acceleration and kinematics in solar flares: a synthesis of recent observations and theoretical concepts" Space Science Reviews **101**, 1 (2002).

11. Aschwanden, M.J. Physics of the Solar Corona, An Introduction (Chichester, UK: Praxis Publishing)(2004).

12. Aschwanden, M.J. and Alexander, D "Flare plasma cooling from 30 MK down to 1 MK modeled from Yohkoh, GOES, and TRACE observations during the Bastille Day event (14 July 2000)" Solar Physics **204**, 91 (2001).

13. Aschwanden, M.J. *et al.* "Electron time-of-flight distances and flare loop geometries compared from CGRO and Yohkoh observations" Ap.J **468**, 398 (1996).

14. Aschwanden, M.J. *et al.* "On the photometric accuracy of RHESSI imaging and spectrosocopy" Solar Physics **219**, 149 (2004).

15. Benz, A.O. "Flare Observations" Living Reviews in Solar Physics **5**, 1 (2008).

16. Bespalov, P.A. *et al.* "Consequences of strong pitch-angle diffusion of particles in solar flares" Ap.J **374**, 369 (1991).

17. Brown, J.C. "The deduction of energy spectra of non-thermal electrons in flares from the observed dynamic spectra of hard X-ray bursts" Solar Physics **18**, 489 (1971).

18. Brown J.C. "Thick target X-Ray bremsstrahlung from partially ionised targets in solar flares" Solar Physics **28**, 151 (1973)

19. Brown, J.C. and McClymont, A.N. "The height distribution of flare hard X-rays in thick and thin target models" Solar Physics **41**, 135 (1975).

20. Brown, J.C., Melrose, D.B. and Spicer, D.S "Production of a collisionless conduction front by rapid coronal heating and its role in solar hard X-ray bursts" Ap.J **228**, 592 (1979).

21. Cane, H.V. *et al.* "Two components in major solar particle events" Geophysical Research Letters **30**, SEP5-1

22. Cane, H.V. *et al.* "Role of flares and shocks in determining solar energetic particle abundances" JGR **111**, A06S90 (2006)

23. Carmichael, H. "A process for flares" AAS-NASA Symposium on the Physics of Solar Flares, NASA SP-30, 451 (1964)

24. Cheng, C.-C. *et al.* "Spatial and temporal structures from solar flares observed in UV and hard X-rays" Ap.J Lett. **248**, L39 (1981).

25. Cheng, C.-C. *et al.* "Temporal correlations between impulsive ultraviolet and hard X-ray bursts at high time resolution" Ap.J **330**, 480 (1988).

26. Choudhary, D.P., Venkatakrishnan, P. and Gosain, S. "On magnetic flux imbalance in solar active regions" Ap.J **583**, 851 (2002).

27. Cohen, C.M.S. "Introduction to SEPs" 2006 SPD Summer School, Durham, NH (2006).

28. Coyner, A. J. and Alexander, D. "Investigating the temporal behavior of localized UV and hard X-ray emission in large solar flares" 37th Meeting of the AAS Solar Physics Division, Durham, NH (2006).

29. Czaykowska, A., Alexander, D., & De Pontieu, B., Ap.J **552**, 849 (2001).

30. Démoulin, P. *et al.* "Evidence of magnetic reconnection in solar flares" Astronomy and Astrophysics **271**, 292 (1993).

31. Démoulin, P. *et al.* "Three-dimensional magnetic reconnection without null points 2: Application to twisted flux tubes" JGR **101**, 7631 (1996).

32. Démoulin, P. *et al.* "Quasi-separatrix layers in solar flares. II: Observed magnetic configurations" Astronomy and Astrophysics **325**, 305 (1997).

33. DeRosa, M.L. private communication (2006).

34. DeRosa, M.L., Freeland, S.L., and Schrijver, C.J. "Magnetic field line rendering package for SolarSoft" LWS SDO Workshop, Boulder, CO (2004).

35. Desai, M.I. *et al.* "Heavy-ion elemental abundances in large solar energetic particle events and their implications for the seed population" Ap.J **649**, 470 (2006).

36. Donnelly, R.F. and Kane, S.R. "Impulsive extreme ultraviolet and hard X-ray emission in solar flares" Ap.J **222**, 1043 (1978).

37. Emslie, A.G. *et al.* "Energy partition in two solar flare//CME events" JGR **109**, A10104 (2004).

38. Emslie, A.G. and Sturrock, P.A. "Temperature minimum heating in solar flares by resistive dissipation of Alfvén waves" Solar Physics **80**, 99 (1982).

39. Forbes, T.G. "Magnetic Reconnection" 2006 SPD Summer School, Durham, NH (2006).

40. Forman, M.A. and Webb, G.M. "Acceleration of energetic particles" in Collisonless shocks in the heliosphere, Vol. 35 of American Geophysical Union, Geophysical Monograph Series, B.T. Tsurutani and R.G. Stone (Washington, D.C.: American Geophysical Union), 91 (1985).

41. Giacalone, J. "The efficient acceleration of thermal protons by perpendicular shocks" Ap.J **628**, 37 (2005).

42. Gilbert, H.R. *et al.* "The filament-Moreton wave interaction of 2006 December 6" Ap.J **684**, in press.

43. Golub, L. *et al.* "The X-ray Telescope (XRT) for the Hinode mission" Solar Physics **243**, 63 (2007).

44. Gosling, J.T. "The solar flare myth" JGR **98**, 18949 (1993).

45. Handy, B.N. *et al.*, "UV observations with the Transistion Region and Coronal Explorer" Solar Physics **183**, 29 (1998).

46. Handy, B.N. *et al.*, "The Transition Region and Coronal Explorer" Solar Physics **187**, 229 (1999)

47. Hirayama, T. "Theoretical model of flares and prominences. I: evaporating flare model" Solar Physics **34**, 323 (1974).

48. Hoeksema, J.T. "The large-scale structure of the heliospheric current sheet during the ULYSSES epoch" Space Science Reviews **72**, 137 (1995).

49. Jokipii, J.R. "Particle drift, diffusion, and acceleration at shocks" Ap.J **255**, 716 (1982).

50. Jokipii, J.R. "Rate of energy gain and maximum energy in diffusive shock acceleration" Ap.J **313**, 842 (1987).

51. Joshi, B. *et al.* "Multi-wavelength signatures of magnetic reconnection of a flare-associated coronal mass ejection" Solar Physics **242**, 143.

52. Kahler, S.W., Sheeley, N.R. Jr., and Liggett, M. "Coronal mass ejections and associated X-ray flare durations" Ap.J **344**, 1026 (1989).

53. Kane, S.R. and Donnelly, R.F. "Impulsive hard X-ray and ultraviolet emission during solar flares" Ap.J **164**, 151 (1971).

54. Kane, S.R., Frost, K.J. and Donnelly, R.F. "Relationship between hard X-ray and EUV sources in solar flares" Ap.J **234**, 669 (1979).

55. Kashapova, L.K., Zharkova, V.V. and Grechnev, V.V. "Signatures of high-energy particles in Hα emission before the solar flare of August 16, 2004" Physics of Chromospheric Plasmas ASP Conference Series, Proceedings of the conference held 9-13 October, 2006 at the University of Coimbra in Coimbra, Portugal. Edited by P. Heinzel, I. Dorotovic(, and R. J. Rutten. **368**, 437

Kitahara, T. and Kurokawa, H. "High-resolution observation and detailed photometry of a great H-alpha two-ribbon flare" Solar Physics **125**, 321 (1990).

56. Kopp, R.A. and Pneumann, G.W. "Magnetic reconnection in the corona and the loop prominence phenomenon" Solar Physics **50**, 85 (1976).

57. Kosugi, T. *et al.*, "The hard X-ray telescope (HXT) for the Solar-A mission" Solar Physics **136**, 17 (1991).

58. Kosugi, T. *et al.* "The Hinode (Solar-B) Mission: An overview" Solar Physics **243**, 3 (2007).

59. Krucker, S. *et al.* "RHESSI X-ray and Gamma-ray observations of the January 20, 2005 event" AGU Fall Meeting Abstract SH21A-01 (2005).

60. Lau, Y.-T. "Magnetic nulls and topology in a class of solar flare models" Solar Physics **148**, 301 (1993).

61. Lin, R.P. "Relationship of solar flare accelerated particles to solar energetic particles (SEPs) observed in the interplanetary medium" Physics of Collisionless Shocks, **781**, 246 (2005).

62. Lin, R.P. *et al.* "The Reuven Ramaty High Energy Solar Spectroscopic Imager" Solar Physics **210**, 3 (2002).

63. Linton, M.G. and Longcope, D.W. "A model for patchy reconnection in three dimensions" Ap.J **642**, 1177 (2006).

64. Liu R. *et al.* "SHINE SEP Campaign Events: Global and Local Magnetic Field Evolution in Build-up to the SEP events of 21 Apr 2002 and 24 Aug 2002" SHINE 2004 Workshop, Big Sky, Montana, (2004).

65. Lui,Y. *et al.* "Observational evidence of a magnetic flux rope eruption associated with the X3 flare on 2002 July 15" Ap.J **593**, 137 (2003).

66. Longcope, D.W. "Topology and current ribbons: a model for current, reconnection, and flaring in a complex, evolving corona" Solar Physics **169**, 91 (1996).

67. Longcope, D.W. and Cowley, S.C. "Current sheet formation along three-dimensional magnetic separators" Physics of Plasma **3**, 2885 (1996).

68. Longcope, D.W. *et al.* "Evidence of separator reconnection in a survey of X-ray bright points" Ap.J **553**, 429 (2001).

69. Longcope, D.W. and Magara, T. "A comparison of the minimum current corona to a magnetohydrodynamic simulation of quasi-static coronal evolution" Ap.J **608**, 1106 (2004).

70. Low, B.C. "Spontaneous current sheets in an ideal hydromagnetic fluid", Ap.J **649**, 1064 (2006).

71. Luhmann, J.G. *et al.* "The relationship between large-scale solar magnetic field evolution and coronal mass ejections" JGR **103** 6585 (1998).

72. MacKinnon, A.L. "Coulomb collisional precipitation in fast electrons in solar flares." Astronomy and Astrophysics **194**, 279 (1988).

73. MacKinnon, A.L. *et al.* "The effect of precipitation on diagnostics for electron trap models of solar hard X-ray bursts" Astronomy and Astrophysics **119**, 297 (1983).

74. Mandrini, C.H. *et al.* "Evidence of magnetic reconnection from Hα, soft X-ray and photospheric magnetic field observations" Solar Physics, **174**, 229 (1997).

75. Mandzhavidze, N. and Ramaty R. "Gamma rays from pion decay - Evidence for long-term trapping of particles in solar flares" Ap.J **396**, 111 (1992).

76. Mason, G.M. *et al.* "The Ultra Low Energy Isotope Spectrometer for the ACE spacecraft" Space Science Reviews **86**, 409 (1998).

77. Masuda, S. *et al.* "A loop-top hard X-ray source in a compact solar flare as evidence for magnetic reconnection" Nature **371**, 495 (1994).

78. Mason, G.M. Mazur, J.E. and Dwyer, J.R. "^{3}He enhancements in large solar energetic particle events" Ap.J **525**, 133 (1999).

79. Mason, G.M. *et al.* "Abundances of heavy and ultraheavy ions in ^{3}He-rich solar flares" Ap.J **606**, 555 (2004).

80. McClements, K.G. "The trap-plus-precipitation model of hard X-ray emission in solar flares" Astronomy and Astrophysics **230**, 213 (1990).

81. McClements, K.G. and Alexander, D. "Fokker-Planck modeling of asymmetric footpoint hard X-ray emission in solar flares" Ap.J **619**, 1153 (2005).

82. Metcalf, T.R. "Correcting TRACE pointing with MDI WL images or EIT EUV images"
(URL: `http://www.lmsal.com/ metcalf/TRACE/pointing.html`) (2003).

83. Metcalf, T.R. "Is the solar chromospheric magnetic field force-free?" **439**, 474 (1995).

84. Metcalf, T.R. *et al.*"Pixon-based multiresolution image reconstruction for Yohkoh's Hard X-ray Telescope" Ap.J **466**, 585 (1996).

85. Metcalf, T.R. *et al.* "TRACE and Yohkoh observations of a white-light flare" Ap.J **585**, 483 (2003).

86. Nishio, M. *et al.* "Magnetic field configuration in impulsive solar flares inferred from coaligned microwave/X-ray images" Ap.J **489**, 976 (1997).

87. Parker, E.N. "The solar-flare phenomenon and the theory of reconnection and annihiliation of magnetic fields" Ap.JS **8**, 177 (1963).

88. Petschek, H.E. "Magnetic field annihilation" in Proceedings of AAS-NASA Symposium 50, The Physics of Solar Flares, 425 (1964).

89. Priest, E.R. and Démoulin, P. "Three-dimensional magnetic reconnection without null points. 1: Basic theory of magnetic flipping" JGR **100**, 23443 (1995).

90. Priest, E.R., Longcope, D.W., and Heyvaerts, J. "Coronal heating at separators and separatrices" Ap.J **624**, 1057 (2005).

91. Reames, D.V. "Particle acceleration at the sun and in the heliosphere" Space Science Reviews **90**, 413 (1999).

92. Rohlf, F.J. and Sokal, R.R., Statistical Tables, (3^{rd} ed.; New York: W.H. Freeman) (1995).

93. Scherrer, P.H. *et al.* "The Solar Oscillations Investigation - Michelson Doppler Imager" Solar Physics **162**, 129 (1995).

94. Schrijver, C.J. and DeRosa, M.L. "Photospheric and heliospheric magnetic fields" Solar Physics **212**, 165 (2003).

95. Smith, D.F. and Lilliequist, C.G. "Confinement of hot hard X-ray producing electrons in solar flares" Ap.J **232**, 582 (1979).

96. Spicer, D.S. and Emslie, A.G. "A new quasi-thermal trap model for solar flare hard X-ray bursts - an electrostatic trap model" Ap.J **330**, 997 (1988).

97. Stone, E.C. *et al.* "The Advanced Composition Explorer" Space Science Reviews **86**, 1 (1988).

98. Stone, E.C. *et al.* "The Solar Isotope Spectrometer for the Advanced Composition Explorer" Space Science Reviews **86**, 357 (1988).

99. Sturrock, P.A. "Model for the high energy phase of solar flares" Nature **211**, 695 (1966).

100. Švestka, Z. and Cliver, E.W. "History and basic characteristics of eruptive flares" Lecture Notes in Physics **399**, 1 (1992).

101. Sweet, P.A. "The neutral point theory of solar flares" in Electromagnetic Phenomena in Cosmical Physics, ed. B. Lehnert (New York: Cambridge Univ. Press), 123 (1958).

102. Tian, L. *et al.* "Magnetic twist and writhe of δ active regions" Solar Physics **229**, 63 (2005).

103. Tian, L. and Alexander, D. "Role of sunspot and sunspot-group rotation in driving sigmoidal active region eruptions" Solar Physics **233**, 29 (2006).

104. Tian, L., Alexander, D. and Coyner, A. "Magnetic topological structures and hard X-ray sources of AR10720: source region of the most energetic event of 20 January 2005" In preparation (2008).

105. Titov, V.S., Hornig, G. and Démoulin, P. "Theory of magnetic connectivity in the solar corona" JGR **107**, 1164 (2002).

106. Tsuneta *et al.* "The soft X-ray telescope for the SOLAR-A mission" Solar Physics **136**, 37 (1991).

107. Tsuneta, S. "Moving plasmoid and formation of the neutral sheet in a solar flare" Ap.J **483**, 507 (1997).

108. Tylka, A.J. "Solar energetic particles (SEPs): a tutorial review" SHINE 2004 Workshop, Big Sky Montana, (2004).

109. Tylka, A.J. and Lee, M.A. "A model for spectral and compositional variability at high energies in large, gradual solar particle events" Ap.J **646**, 1319 (2006)

110. Tylka, A.J. *et al.* "Shock geometry, seed populations, and the origin of variable elemental composition at high energies in large gradual solar particle events" Ap.J **625**, 474 (2005).

111. Tylka, A.J. *et al.* "Spectral and compositional characteristics of very large SEP events in the declining phase of solar cycle 23" SHINE 2006 Workshop, Midway, Utah, (2006).

112. Vlahos, L. "The 3D picture of a flare" First Meeting of ISSI International Team on coronal hard X-ray sources in solar flares, (2006).

113. Wang, H. *et al.* "Topology of magnetic field and coronal heating in solar active regions - II. The role of quasi-separatrix layers" Solar Physics **197**, 263 (2000).

114. Wang, Y. and Zheng J. "A comparative study between eruptive X-class flares associated with coronal mass ejections and confined X-class flares" Ap. J **665**, 1428 (2007).

115. Warren, H.P. and Warshall, A.D. "Ultraviolet flare ribbon brightenings and the onset of hard X-ray emisson" Ap.J Lett. **560**, L87 (2001).

116. Weiss, L.A. *et al.* "A comparison of interplanetary coronal mass ejections at Ulysses with Yohkoh soft X-ray coronal events" Astronomy and Astrophysics **316**, 384 (1996).

117. Wheatland, M.S. and Melrose, D.B. "Interpreting YOHKOH hard and soft X-ray flare observations" Solar Physics **158**, 283 (1995).

118. Woodgate, B.E. *et al.* "Simultaneous ultraviolet line and hard X-ray bursts in the impulsive phase of solar flares" Ap.J **265**, 530 (1983).

119. Wülser, J.P. *et al.* "Multispectral observations of chromospheric evaporation in the 1991 November 15 X-class solar flare" *et al.* Ap.J **424**, 459 (1994).

120. Yashiro, S. *et al.* "Visibility of coronal mass ejections as a function of flare location and intensity" JGR **110**, A12S05 (2005).

121. Zhang, Y. Zhang, M. and Zhang, H.Q. "A statistical study on the relationship between surface field variation and CME initiation" Advances in Space Research, **39**, 1762 (2007).

122. Zhao, X. and Hoeksema, J.T. "Effect of coronal mass ejections on the structure of the heliospheric current sheet" JGR **101**, 4825. (1996).

123. Zharkova, V.V. and Gordovskyy, M. "Particle acceleration asymmetry in a reconnecting nonneutral current sheet" Ap.J **604**, 884 (2004).

124. Zharkova, V.V., Kashapova, L.K., Chornogor, S.N., and Andriyenko, O.V. "The multi-wavelength study of the effect of energetic particle beams on the chromospheric emission in the 25th July 2004 solar flare" Advances in Space Research **39**, 1483 (2007).